

Control of Integrated Three-level and Multi-level Converter Topologies with Driving and Charging Capabilities for Switched Reluctance Motor Drive-Train Based EV Application

A Thesis Submitted
In Partial Fulfillment of the Requirements
for the Degree of

Doctor of Philosophy

by

Vaibhav Shah
(2018EEZ0010)



Department of Electrical Engineering

Indian Institute of Technology, Ropar

Rupnagar-14001, Punjab, India

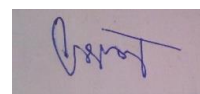
July 2023

Copyright © “2023” by Indian Institute of Technology Ropar

DEDICATED
TO
FAMILY

DECLARATION

I declare that this work entitled “**Control of Integrated Three-level and Multi-level Converter Topologies with Driving and Charging Capabilities for Switched Reluctance Motor Drive-Train Based EV Application**” has not previously been accepted in substance for any degree and is not being simultaneously submitted in candidature for any other degree. This thesis is being submitted in partial fulfillment of the requirements for the degree of Ph.D. in Electrical Engineering. This thesis results from my independent investigation, except where otherwise stated. I have acknowledged all the other sources by stating the references explicitly. I declare that any idea/data/fact/source stated in my thesis has not been fabricated/falsified/misrepresented. All the principles of academic honesty and integrity have been followed. I understand that any above violation will cause disciplinary action by the Institute and can also evoke penal action from the sources that have thus not been properly cited or from whom proper permission has not been taken when needed. I, as a result of this give consent for my thesis, if accepted, to be available online in the Institute’s Open Access repository and for inter-library loan, and for the title and abstract to be made available to outside organizations.



Signature

Name: **Vaibhav Shah**
Entry Number: **2018EEZ0010**

Date: 24/07/2023

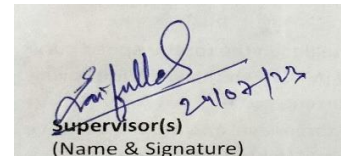
ACKNOWLEDGMENTS

I would like to take this opportunity to express my deep sense of gratitude and profound feeling of admiration for my thesis supervisor Dr. Saifullah Payami (Assistant Professor, Department of Electrical Engineering). I would also like to thank Dr. Subrahmanyam Murala, Head of Department, Electrical Engineering for providing the facilities required for my Ph.D. work. I would also thank my DC committee members for their help and support: Dr. C. C. Reddy (Professor, Department of Electrical Engineering), Dr. R. Sekhar (Assistant Professor, Department of Electrical Engineering), and Dr. Himanshu Paliwal (Assistant Professor, Department of Chemical Engineering).

I also appreciate the help given by my lab research scholars, Mahetab Alam, Gautam Kumawat, Zeeshan Rayeen, and Abdul Azeem for being ever prepared to assist me and supporting me during my Ph.D. work.

CERTIFICATE

It is certified that the work contained in the thesis titled “Control of Integrated Three-level and Multi-level Converter Topologies with Driving and Charging Capabilities for Switched Reluctance Motor Drive-Train Based EV Application,” by “Mr. Vaibhav Shah” has been carried out under my/our supervision and that this work has not been submitted elsewhere for the award of any degree.



Supervisor(s)
(Name & Signature)

Name(s): Dr. Saifullah Payami
Department(s): Electrical Engineering
IIT Ropar.

ABSTRACT

The application of switched reluctance motors (SRMs) for industrial electrical drives is slow despite its simple construction, ruggedness, and extensive research in the past decade. The higher ripples in the torque profile and acoustic noise are the primary disadvantages of SRM. For continuous torque production in SRM, active torque-producing phases ideally need to be serially excited via a rectangular current waveform. However, with limited phase voltage applied, this cannot be achieved, resulting in sharing of total torque among the incoming and outgoing phases during the commutation region. The sharing of the total torque among commutating phases majorly accounts for ripples in the torque profile for SRM. Thus, during commutation, the contribution of the incoming and outgoing phase torque towards the total torque needs to be controlled judiciously via the employed control algorithm for targeting torque ripple minimization in SRM.

In the existing literature, the control techniques developed/proposed for SRM achieve torque ripple minimization for a limited operating region in the torque-speed curve. In order to simultaneously enhance/improve the smooth torque operating region and the torque/ampere ratio, the thesis investigates a new direct torque control (DTC) for a 4-phase SRM. With the investigated DTC scheme, the contribution of the incoming and outgoing phases toward the total torque is monitored as per the respective phases' real-time inductance profile. However, with the limited phase voltage applied via the conventional converter for SRM, the ripple in the torque profile via the proposed DTC scheme can only be minimized to a certain extent. For further enhancing the operating region in the torque-speed curve, the thesis investigates a multi-level converter topology (MLCT) which aids in improving the energization and de-energization of the phase current. The commutation region width is reduced with improved energization and de-energization, resulting in a smooth torque profile for higher operating speeds.

With the advancement in control techniques and extensive research towards different MLCTs, SRM-based drive-trains are extensively developed for electric vehicle (EV) applications. Since EVs are powered via a battery storage system, charging them is another area of research concerning SRM-based drive-train. Conventional EV drive-train employing SRM as traction motors have separate on-board charging module/s for charging the battery via AC and/or DC sources. However, on-board charging modules incur an additional cost and are limited in their charging power output due to size and cost constraints associated with the EV drive-train.

However, for SRM, its isolated phase winding configuration allows easy integration of driving and charging modes, and such drive trains are termed integrated drive trains. With integrated drive-trains, the requirement of separate on-board charging modules and associated passive element/s is/are eliminated as the traction converter power electronic/s component/s, and the phase winding/s are reconfigured/reutilized to realize the battery charger functionality. In the existing literature, the SRM-based integrated drive-trains neglect their performance validation during the driving mode of operation, which results in higher ripples in torque profiles. Moreover, most proposed ICs do not achieve net zero charging torque production via the charging current within the reconfigured phase winding/s. Thus, a mechanical fixture is used for validating the efficacy of the integrated drive-trains during charging mode, which has practical limitations.

The thesis identifies this as an active research area and proposes three-level and multi-level integrated drive trains for SRM with zero charging torque production. In addition, with the implementation of the investigated DTC technique, the performance of the proposed integrated drive-trains is improved for the drive mode of operation.

LIST OF PUBLICATIONS

Journal papers (Accepted and in press)

- **V. Shah** and S. Payami, "An Integrated Driving/Charging 4-Phase Switched Reluctance Motor Drive with Reduced Current Sensors for Electric Vehicle Application," in *IEEE Journal of Emerging and Selected Topics in Power Electronics*, doi: 10.1109/JESTPE.2021.3120468.
- **V. Shah** and S. Payami, "Fully Integrated Multi-Level Power Converter for SRM Drive with Charging Capabilities (G2V) for Electric Vehicle Application," in *IEEE Journal of Emerging and Selected Topics in Industrial Electronics*, 2022, doi: 10.1109/JESTIE.2022.3190794.
- **V. Shah**, G. Kumawat and S. Payami, "Phase Current Reconstruction Technique for 4-Phase Switched Reluctance Generator with Two Current Sensors," in *IEEE Journal of Emerging and Selected Topics in Power Electronics*, 2022, doi: 10.1109/JESTPE.2022.3217693.
- **V. Shah** and S. Payami, "Integrated Converter with G2V, V2G, and DC/V2V Charging Capabilities for Switched Reluctance Motor Drive-Train Based EV Application," in *IEEE Transactions on Industry Applications*, doi: 10.1109/TIA.2023.3242636.

Journal papers (Under Revision)

- **V. Shah** and S. Payami, "Switched Reluctance Motor Drive-train with Fully Integrated Battery Charger and Instantaneous Zero Charging Torque for Electric Transportation" (*Minor Revision with provisional acceptance*).
- **V. Shah** and S. Payami "Direct Torque Control Technique for 4-Phase Switched Reluctance Motor to Extend Smooth Torque Operating Region" (Submitted for review in IEEE-JESTPE)

Conference papers (Accepted and Presented)

- **V. Shah**, M. Alam and S. Payami, "High Torque/Ampere Direct Torque Control of Switched Reluctance Motor Drives," 2019 National Power Electronics Conference (NPEC), 2019, pp. 1-6, doi: 10.1109/NPEC47332.2019.9034777.
- **V. Shah**, M. Alam and S. Payami, "A Novel Direct Torque Control Scheme for High-Speed Control of Switched Reluctance Motor Using 4-Level Torque Controller," The 10th International Conference on Power Electronics, Machines and Drives (PEMD 2020), 2020, pp. 966-971, doi: 10.1049/icp.2021.0974
- **V. Shah** and S. Payami, "A Novel Direct Torque Control for 4-Phase Switched Reluctance Motor Considering the Actual Rotor Pole Arc with High Torque/Ampere Ratio," IECON 2020 The 46th Annual Conference of the IEEE Industrial Electronics Society, 2020, pp. 826-831, doi: 10.1109/IECON43393.2020.9254741.

- **V. Shah** and S. Payami, "A Novel 4-level Converter with Inherent Voltage Boosting for 4-Phase SRM," 2020 IEEE International Conference on Power Electronics, Drives and Energy Systems (PEDES), 2020, pp. 1-6, doi: 10.1109/PEDES49360.2020.9379535.
- **V. Shah** and S. Payami, "Integrated Power Converter with G2V and V2G capabilities for 4-Phase SRM Drive Based EV Application," 2021 IEEE 2nd International Conference on Smart Technologies for Power, Energy and Control (STPEC), 2021, pp. 1-6, doi: 10.1109/STPEC52385.2021.9718718.
- **V. Shah** G. Kumawat and S. Payami, "Integrated Power Converter with G2V, V2G and Direct V2V Capabilities for SRM Drive Based Electric Vehicle Application," 2022 Second International Conference on Power, Control and Computing Technologies (ICPC2T), 2022, pp. 1-6, doi: 10.1109/ICPC2T53885.2022.9776689.
- **V. Shah**, G. Kumawat and S. Payami, "An Integrated Charger with High Efficiency Over Wide Range of Input Voltage with G2V, V2G, and Direct V2V capabilities for SRM Drive," 2022 IEEE IAS Global Conference on Emerging Technologies (GlobConET), 2022, pp. 12-17, doi: 10.1109/GlobConET53749.2022.9872370.
- **V. Shah** and S. Payami, "A Multi-Level Converter for SRM Drive Based EV Applications with Auxiliary Load Driving Capability," 2022 IEEE 2nd International Conference on Sustainable Energy and Future Electric Transportation (SeFeT), 2022, pp. 1-6, doi: 10.1109/SeFeT55524.2022.9909185.
- **V. Shah**, G. Kumawat and S. Payami "Solar Powered Electric Drive-Train With Integrated Bidirectional DC/V2V Fast Charger Incorporating Switched Reluctance Motor" 2022 IEEE GLOBAL CONFERENCE ON COMPUTING, POWER AND COMMUNICATION TECHNOLOGIES (GlobConPT).
- **V. Shah** and S. Payami "Solar Powered Electric Drive-Train With Integrated Multifunctional Dual Power On-Board Charger Incorporating N-phase SRM" 2022 IEEE International Conference on Power Electronics, Drives and Energy Systems.

TABLE OF CONTENTS

Declaration	iv
Acknowledgment	v
Certificate	vi
Abstract	vii
List of Publications	viii
List of Figures	xii
List of Tables	xv
Notations and Abbreviations	xvi
Chapter-1- Introduction and Literature Review	
1.1 Introduction	1
1.2. Literature Review	6
1.3. Objective and Motivation of the Thesis	10
Chapter-2- Direct torque control technique for 4-phase switched reluctance motor to extend smooth torque operating region	13
2.1. Generalized Modelling of Simultaneous-Phase Excited SRM	15
2.2. Proposed Direct Torque Control Technique	18
2.3. Sector Reorganization in The Proposed DTC Scheme	23
2.4. Implementation Of Proposed Direct Control Technique Scheme- Experimental Results	27
2.5. Conclusion	
Chapter-3- An Integrated Driving/Charging 4-Phase Switched Reluctance Motor Drive with Instantaneous Zero Charging Torque Production	
3.1. Proposed IC During Drive Mode	29
3.2. Proposed IC During Battery Charging Mode	32
3.3. Novel Charging Rotor Positions for ZCT And Simulation Results	34
3.4 Experimental Verification	39
3.5. Conclusion	46
Chapter-4- Fully Integrated Multi-Level Power Converter for SRM Drive with Charging Capabilities (G2V) For Electric Vehicle Application	
4.1. Operating Modes and Control Technologies of the proposed IML-PCT	47
4.2 Experimental Verification	55
4.3. Conclusion	59
Chapter-5- Integrated Converter with G2V, V2G, And DC/V2V Charging Capabilities for Switched Reluctance Motor Drive-Train Based EV Application	60
	62

5.1. Proposed IC During Drive Mode	66
5.2. Configuration And Control of The Proposed IC During G2V Charging Mode	68
5.3. Configuration Of the Proposed IC During DC/V2V Charging Mode	69
5.4. Configuration And Control of The Proposed IC During V2G Charging Mode	72
5.5. Charging Rotor Positions and Torque Analysis	78
5.6. Experimental Results	
6.7. Conclusion	
 Chapter-6- A Universal-Input Integrated Power Converter For 4-Phase Switched Reluctance Motor Drive-Based EV Application	
6.1. Literature Review for Universal Charger	80
6.2. Operational Modes of The Proposed IC	81
6.3. Torque production via charging current in phase windings	87
6.4 Experimental Validation and Discussion	88
6.5. Conclusion	90
 Conclusion and Future Scope	92
References/Bibliography	94
Appendix	100

LIST OF FIGURES

S. No.	Figure Caption	Page No.
1.	Active phase conduction intervals with inductance profile for low/medium-speed operation.	2
2.	Active phase conduction intervals with inductance profile for High-speed operation.	2
3.	Energization and de-energization during motoring and regenerative operation with three-level and multi-level topology.	3
4.	EV drive-train with different enclosures for driving and charging modes.	5
5.	EV drive-train with integrated converter.	6
6.	(a). Self-inductance profile of phase-A, for different operating currents. (b) Estimated torque of phase-A, for different operating currents	16
7.	Inductance profile of the prototype 4-phase SRM obtained from ANSYS/Maxwell, at phase current of 11 A.	16
8.	(a) Sector diagram in one electrical space. (b) Voltage vectors in simultaneous phase excited 4-phase SRM.	16
9.	(a). Flux vector position to obtain the maximum change in $\vec{\varphi}_{\alpha\beta(k)}$. (b) Flux vector position to obtain the minimum change in $\vec{\varphi}_{\alpha\beta(k)}$.	18
10.	Reorganized sector widths for DTC-I and the corresponding experimentally obtained phase currents.	19
11.	Experimental results at 1500 rpm and 3 N-m. Total torque output during commutation and torque contribution individual phase-A and phase-B. Torque: 2 N-m/div, current: 10 A/div, and time: 1ms/div.	20
12.	Flowchart representing real-time sector-reorganization for adjustable sector boundaries, i.e., starting of sector 2, 4, 6, and 8 in DTC-I.	21
13.	Reorganized sector widths for DTC-II and the corresponding experimentally obtained phase currents.	22
14.	(a) $T_{e,ad}(\theta, i_a = 11 \text{ A}, i_d \{0 \text{ A} \rightarrow 11 \text{ A}\})$, and (b) $T_{e,ab}(\theta, i_a = 11 \text{ A}, i_b \{0 \text{ A} \rightarrow 11 \text{ A}\})$.	23
15.	Flowchart representing real-time sector reorganization for adjustable sector boundaries, i.e., starting of sector 2, 4, 6, and 8 in DTC-II.	23
16.	Schematic diagram with the experimental setup.	24
17.	Experimental waveforms of conventional CCC for a load torque of 3 N-m. (a) 500 rpm, and (b) 1500 rpm.	25
18.	Experimental waveforms of DITC for a load torque load of 3 N-m. (a) 500 rpm, and (b) 1500 rpm.	25
19.	Experimental waveforms of the proposed DTC-I scheme for a load torque of 3 N-m. (a) 500 rpm. (b) 1500 rpm.	26
20.	(a) Experimental waveforms of DTC-I for speed change at constant load of 1 N-m. (b) Experimental waveforms of DTC-I for load change at 1500 rpm.	26
21.	Experimental waveforms of the proposed DTC-II scheme for a load torque of 2 N-m. (a) 2500 rpm. (b) 3000 rpm.	27
22.	. Comparison of (a) efficiency and (b) torque ripple at 3 N-m for proposed DTC-I, DTC-II and conventional CCC and DITC.	28
23.	Proposed IC configuration (a) Proposed IC, (b) front-end BDDC, and (c) front-end BDDC as boost converter.	29
24.	Front-end BDDC control for motoring and regenerative operation	30
25.	Adopted control strategy for the proposed IC during the driving mode.(a) control technique, and (b) switching states for reference and actual phase currents.	30
26.	Working states of the improved miller converter (a) energization, (b) free-wheeling, and (c) de-energization.	31
27.	Simplified and complete diagram of battery charging scheme with the employed control strategy.	33
28.	Operating modes of the BB-PFC during battery charging mode. (a) Positive half-cycle, switch (Q2, Q3) ON state. (b) Positive half-cycle, switch (Q2, Q3) OFF state. (c) Negative half-cycle, switch (Q6, Q7) ON state, and (d) Negative half-cycle, switch (Q6, Q7) OFF state.	34
29.	(a) Designed prototype 4-phase SRM. (b) Actual inductance profile of the 4-phase SRM.	35
30.	(a) Simulation results when charging at rotor position (a) A1, and (b) rotor position B1.	36
31.	(a) FEA of magnetic field when battery charging at rotor position (a) A1 and (b) rotor position B1.	37
32.	Experimental test bench.	40

33.	Experimental results for phase-A voltage and current with quadrature phase-C current and rotor position during drive mode of operation (a) 1500 rpm, (b) 3100 rpm, and (c) Dynamic performance with speed, current, and experimental torque waveforms.	41
34.	Experimental results when charging at rotor position A1. (a) Input AC voltage, current with adjacent phase-A and phase-B currents (b) Input AC voltage, current with quadrature phase-A and phase-C currents. (c) All four phase currents with input AC current using MATH operation.	44
35.	Rotor position (θ_{mech}) with total charging torque generated with battery voltage and current when charging battery at (a) rotor position A1, and (b) rotor position B1.	45
36.	Experimental input AC current FFT analysis.	46
37.	Proposed IML-PCT with driving and charging capabilities for 4-phase SRM drive-based EV application.	47
38.	Control strategy for the front-end BDDC during the driving mode.	47
39.	(a) IML-PCT configuration during driving mode. Operating modes of the IML-PCT (b) Mode-I, (b) Mode-II, (d) Mode-III, and (e) Mode-IV.	49
40.	Comparison of voltage levels of the IML-PCT with 3-level AHB/miller converter.	50
41.	IBB-PFCC operating modes during battery charging.	52
42.	Resulting IBB-PFCC with employed control strategy.	52
43.	Charging rotor positions during the battery charging mode.	54
44.	Experimental setup.	55
45.	Proposed IML-PCT experimental results during the motoring mode (a) 1500 rpm, $T_L = 1.9$ N-m (when operated as conventional AHB/miller converter (b) 1500 rpm, $T_L = 1.9$ N-m and (c) 3150 rpm [maximum operational speed].	56
46.	Torque-speed curve with AHB/miller converter and proposed IML-PCT.	57
47.	. Proposed IML-PCT experimental results during battery charging (a) input AC voltage and current with phase-B and phase-C windings current, (b) input AC voltage and current waveform with phase-A and phase-C windings current, and (c) BESS voltage and current with transient torque generated.	58
48.	Proposed IC topology for 4-phase SRM.	60
49.	Proposed IC during drive mode of operation.	60
50.	Operating modes during drive mode of operation (a) motoring, (b) free-wheeling, and (c) de-energization	61
51.	Adopted control strategy for the proposed IC during the driving mode. (a) control technique, and (b) switching states for the corresponding reference and actual phase currents.	61
52.	Proposed IC topology under G2V/V2G charging mode.	62
53.	Reconfigured boost inductor for BB-PFC when (a) J1- opened, and J2 closed, and (b) J1-closed, and J2-opened.	62
54.	PFC operation of the BB-PFC during the positive half cycle. (a) Switch ON state. (b) Switch OFF state.	64
55.	PFC operation of the BB-PFC during the negative half cycle. (a) Switch ON state. (b) Switch OFF state.	64
56.	FQDDC operational states under buck mode of operation. (a) Switch ON state. (b) Switch OFF state	64
57.	FQDDC operational states under boost mode of operation. (a) Switch ON state. (b) Switch OFF state	65
58.	Proposed IC configuration during DC/V2V charging mode.	66
59.	Current path during V2G operation for the positive half cycle. (a) Switch ON state. (b) Switch OFF state.	68
60.	Current path during V2G operation for the negative half cycle. (a) Switch ON state. (b) Switch OFF state.	68
61.	Inductance profile of prototype 4-phase SRM.	70
62.	Steady state response during drive mode of operation for (a) 500 rpm, and (b) 3000 rpm.	72
63.	Experimental waveforms for AC grid voltage, current and phase-A, phase-C currents for a battery charging current reference of 10A when charging is performed at rotor position (a) A1, (b) A2, and (c) A4.	73
64.	Experimental obtained rotor position, phase-B, and phase-D currents for a battery charging current reference of 10A when charging is performed at rotor position (a) A1, (b) A2, and (c) A4.	73

65.	FEA of magnetic flux density (B) for the marked instant when charging is performed (a) rotor-position A1, (b) rotor-position A2, and (c) rotor-position A4.	74
66.	Experimental waveform for V2V charging operation when integrated FQDDC operates in buck mode at (a) rotor position-A1, (b) rotor position-A3. (c) Experimental waveform for V2V discharging operation when integrated FQDDC operates in reverse boost mode at rotor position-A1.	76
67.	Experimental waveform of AC grid voltage, current and respective phase currents during V2G operation.	77
68.	Flowchart diagram.	78
69.	Proposed IC configuration for n-phase SRM drive.	82
70.	(a) Proposed IC configuration for 4-phase SRM drive. (For driving mode, relay J1 is closed). (b) Adopted control scheme while driving.	82
71.	Proposed IC configuration during battery charging mode (J1-open).	83
72.	Synchronous switching/cascade buck-boost operation of the two-phase IBuCBB or single-phase BuCBB configuration	83
73.	Input AC current, and phase-B and phase-D currents when two 180° phase shifted buck-boost pairs operate with (a) $D \geq 0.5$, and (b) $D < 0.5$. (Simulated result). (c) Control scheme for cascade buck-boost mode of operation. (d) Duty ratio during buck and boost operation.	85
74.	Proposed IC during battery charging mode, when operating in boost mode.	86
75.	Torque produced via charging currents when operating in boost mode (Simulated result- ($V_{ac} = 230$ V rms, $V_{BESS} = 400$ V, $i_{BESS} = 5$ A)).	88
76.	Torque produced via charging currents when operating in cascade buck-boost mode ($V_{ac} = 230$ V rms, $V_{BESS} = 400$ V, $i_{BESS} = 5$ A))	88

LIST OF TABLES

S. No.	Table Caption	Page No.
1.	Comparison of existing IC in the literature	11
2.	Voltage Vectors Table	16
3.	Voltage Vector Selection Table	17
4.	Phase Turn-On Signal Generation Logic	31
5.	Charging Positions A1, A2, A3, A4 Characteristics	35
6.	Phase Characteristics at Charging Positions B1, B2, B3, B4.	36
7.	Phase Characteristics at Different Charging Rotor Positions	53
8.	Nearest Charging Rotor Position From the EV Parking Position	53
9.	Phase Turn-On Signal Generation Logic	61
10.	Operation Modes Of FQDDC During G2V Charging	64
11.	Reconfigured Phase Winding/s For Different Rotor Positions	70

NOTATIONS AND ABBREVIATIONS

S. No.	Abbreviations	
1.	SRM	Switched reluctance motor
2.	BEMF	back-electromotive force
3.	STOR/STOA	smooth torque operating region smooth torque operating area
4.	MLCT	multi-level converter topology
5.	BES	battery energy storage system
6.	EV	Electric vehicle
7.	OBCM	on-board charging module
8.	IC	Integrated converter
9.	PFC	power factor correction
10.	G2V	grid-to-vehicle
11.	V2G	vehicle-to-grid
12.	DCFC	DC fast charging
13.	V2V	vehicle-to-vehicle
14.	PV	photovoltaic
15.	CCC	constant current control
16.	TSF	torque sharing function
17.	DITC	direct instantaneous torque control
18.	DFTC	direct flux and torque control
19.	DTC	direct torque control
20.	AHB	asymmetrical half-bridge
21.	ZCT	zero charging torque
22.	BDC	buck DC converter
23.	TQDDC	two-quadrant DC-DC converter
24.	BB-PFC	bridgeless boost power factor correction
25.	ZCT	zero charging torque
26.	FQDDC	four-quadrant DC-DC converter

CHAPTER 1

1.1 INTRODUCTION

Switched reluctance machines (SRM) have various advantages such as robustness, simplicity of design, fault tolerance, and its capability to work over a higher speed range when compared with conventional AC machines [1]. However, the application of SRMs for industrial electrical drives is slow despite its simple construction, ruggedness, and extensive research in the past decade. The higher ripples in the torque profile and acoustic noise are the primary disadvantages of SRM [1].

In the SRM drive for continuous and ripple-free torque output, the traction converter ideally needs to serially excite the torque-producing active phase by an ideal rectangular current waveform [1]. Moreover, to maximize the phase instantaneous torque production, the active phase is excited during its maximum slope of the inductance/flux-linkage profile. The approximated partial differential equation for the instantaneous phase torque ($T_e(\theta, i)$) for SRM is given by

$$T_e(\theta, i) \approx i \frac{\partial \varphi(\theta, i)}{\partial \theta}, \quad (1.1)$$

where, $\varphi(\theta, i)$ is the phase stator flux as a function of rotor position and phase current. Thus from (1.1), immediate energization and de-energization of the active phase are desirable for a smooth transfer of total torque from the outgoing phase to the incoming phase [1].

However, due to limitations on the applied phase voltage, a finite time is required to energize and de-energize the phase currents. The time required to energize and de-energize the phase current depends on the net applied phase voltage [2]. The net applied phase voltage is the difference between the applied phase voltage and the instantaneous back-electromotive force (BEMF) developed, which is speed-dependent [2]. From (1.2), it is observed that the net applied phase voltage reduces as the operating speed increases. It also reduces the available time for active phase current energization and de-energization with respect to the rotor position. The variation of phase current with respect to the rotor position is given by

$$\frac{V_q - \omega \frac{d\varphi(\theta, i)}{d\theta}}{\omega \frac{d\varphi(\theta, i)}{di}} = \frac{di}{d\theta}, \quad (1.2)$$

where V_q is the applied phase- q voltage, $\omega \frac{d\varphi(\theta, i)}{d\theta}$ is the BEMF, and ω denotes the operating speed [2].

The finite energization and de-energization time associated with the phase current waveform results in a commutation region wherein the total torque-producing responsibility is transferred from the outgoing to the next incoming phase in the serial excitation sequence. Thus, for SRM, maximum torque ripple arises during the commutation region wherein the total torque is shared among commutating phases, as shown in **Fig. 1.1**.

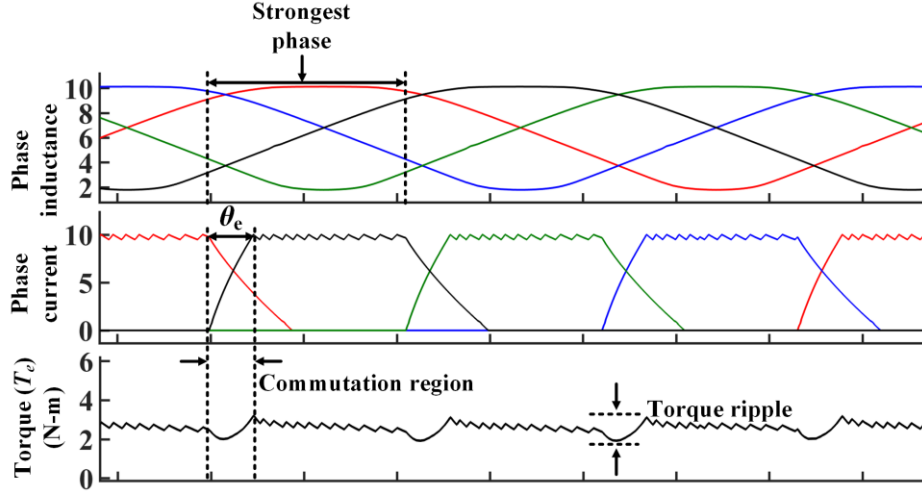


Fig. 1.1. Active phase conduction intervals with inductance profile for low/medium-speed operation.
(Y-Axis- Time (Not to scale) for illustration purposes only)

For calculating the angular width required for phase current energization, i.e., θ_e , the expression derived in [3] can be used, where θ_e is given by

$$\theta_e = \frac{\omega L_u}{R + x \omega} \ln \frac{V_{ph} - (R + x \omega)i_{ref}}{V_{dc}}, \quad (1.3)$$

where V_{ph} is the applied phase voltage, R is the phase resistance, i_{ref} is the reference current, and ω denotes the operating speed. x represents the $\frac{\partial L}{\partial \theta}$ ratio and L_u represents the inductance of the aligned phase. From (1.3), it can be further observed that the time taken by the rotor to cover one rotor pole pitch/ electrical cycle also decreases as the operating speed increases along with a reduction in the net applied phase voltage. In context to the rotor position, this increases the energization and de-energization time of the phase current, leading to an increased ripple in torque profile during the commutation region and lower average torque output, as shown in **Fig. 1.2**.

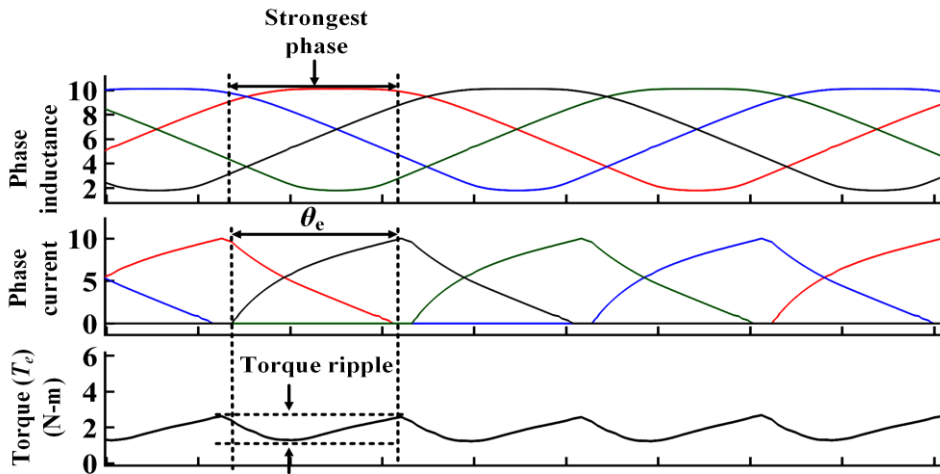


Fig. 1.2. Active phase conduction intervals with inductance profile for High-speed operation.
(Y-Axis- Time (Not to scale) for illustration purposes only)

Thus, the control over instantaneous phase torque and the corresponding torque ripples during commutation is not achieved/possible at higher operating speeds. Moreover, the smooth torque operating region (STOR) achieved via any control method proposed/developed for SRM is restricted [4]. The advantages and shortcomings of the state-of-the-art torque ripple minimization technique available in the existing literature for SRM drive are discussed in later subsection of the chapter.

For extending the STOR, faster energization and de-energization of the active phase current must be addressed at higher operating speeds. The fast energization of the incoming active phase current can be achieved in two ways. Firstly, by providing an extra angular position for the phase current build-up [5]. Secondly, by nullifying the effect of higher BEMF by increasing the applied phase voltage [6]. The incoming phase quickly reaches its current reference by applying higher phase voltage [6]. Also, the faster de-energization of the phase current is equally crucial so that the outgoing phase current quickly reduces to zero. Thus, restricting the tail current conduction within the positive slope of the inductance profile. To address the issues mentioned above, several multi-level converter topologies (MLCTs) are proposed in the existing literature [7]-[9].

Fig. 1.3. shows the energization and de-energization intervals associated with three-level and multi-level converters for motoring and regenerative braking mode of operation. Marked regions A1 and A2 show the reduction in required energization and de-energization time when MLCT is adopted instead of a three-level converter topology.

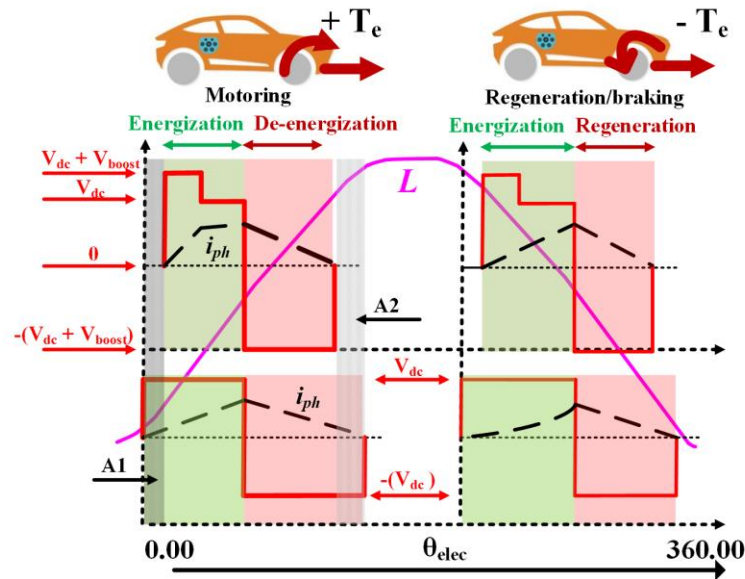


Fig. 1.3. Energization and de-energization during motoring and regenerative operation with three-level and multi-level topology. (for illustration purposes only)

With the advancement in control techniques and MLCTs, SRM-based drive-trains are extensively researched and developed for electric vehicle (EV) applications. According to the author's knowledge, Land Rover and Chloride LUCAS drive-trains for the present EV market employ SRM as traction motors [10]. EV drive-trains are powered via battery energy storage systems (BES), and their capacity decides the driving range for an EV. For higher driving ranges, BES capacity increases. However, BES adds to the curb weight of the EV, its size, weight and capacity are associated constraints with it.

The EV battery must be frequently charged to regain/increase the driving range. For this, the EV drive-train is

mandatorily equipped with a single-phase AC level-1 on-board charging module (OBCM). With single-phase OBCMs, EVs can charge their BES via commonly available single-phase commercial or residential/ public AC outlets [11].

Single-phase OBCMs with power output ranging from 2 kW to 11 kW are industrially available [11]. However, as the power output of the OBC module increases, its size, volume, and cost increase. Thus, to eliminate the OBC module, the EV drive-train can be integrated with an on-board battery charger functionality into/with the drive converter. The integrated on-board charger is realized by reconfiguring/ reutilizing the high-power drive converter that facilitates BES charging with maximum allowable power from a single-phase supply without any additional cost and space. Integrated converter (IC) technology is developed because the traction converter power electronics are not engaged when the EV is idle. Thus, for integrating driving and charging modes, the traction converter is provided with additional switches and relay/s. ICs also eliminate bulky inductor/s requirement for realizing integrated battery chargers as phase winding/s of the employed electric traction motor is/are reconfigured/reutilized as inductor/s. Thus, bringing different drive-train components into a single, compact mechanical enclosure simplifies assembly and design.

IC during drive mode is reconfigured as a drive power converter. And when the EV is standstill/idle, the IC is reconfigured as a power factor correction (PFC) based battery charger for charging BES via a single-phase AC grid, i.e., grid-to-vehicle (G2V) charging. The power electronic switches of the ICs are usually bidirectional; thus, they provide an opportunity to integrate additional functionality of vehicle-to-grid (V2G) charging. With integrated V2G, EV BES is considered asset storage that can support the grid during peak power demand and mitigate the intermittency of renewable energy.

However, due to limitations on maximum allowable power from a single-phase grid, conventional or integrated single-phase on-board battery chargers can take longer (6-10 hours) to charge the BES completely. Also, recent studies show that increased EV penetration into the distribution/residential grid results in disruptive problems, which are highlighted and reported in [12]. Thus, for higher charging power DC charging is used/adopted [13]. In this regard DC fast charging (DCFC) station infrastructure is developed for faster charging of BES via an off-board charger. The output power of the DCFC station ranges from 50 kW to 350 kW and can charge the BES in 0-0.5 hours. [13]. However, the DCFC station requires space and higher initial investment as multiple power conversion stages transform three-phase AC power into DC power, which impedes installation within residential and urban areas.

Thus, for faster charging of BES via DC sources, DC/vehicle-to-vehicle (V2V) charging technology has been practiced in research and industry [14]-[17]. DC sources include solar photovoltaic (PV) systems installed on or external to EVs, emerging DC grids, and BESs of other EVs. In practice, charging via solar PV installed on EVs has been recently tested by Toyota, Sharp, and NEDO [18]. For DC/V2V charging, the EV drive train is provided with a DC-OBCM [14]. Alternatively, external DC/V2V chargers that can be carried separately in the EV trunk are commercially available [15]-[17]. However, an additional bulky module with power electronics rated to support DC power equal to or greater than 50 kW is added/carried in the EV trunk, increasing its weight and cost.

Given the benefits of DC-OBCM, recent ICs for AC drives also integrate a DC/V2V charger [19]. Thus, with an integrated DC/V2V charger, the maximum charging power can be increased up to the rated power of the IC without any additional DC charging module requirement.

To conclude, integrating a DC charger and a single-phase charger facilitates faster charging of BES. Also, it provides the ability to charge BES independently of the power socket (via solar PV systems).

Earlier ICs focus majorly on conventional induction and permanent magnet motors-based EV drive. However, recent developments in SRM drives possess high competitiveness for conventional EV drives because of their advantages. The major advantage of considering the SRM drive-train for integrating driving and battery charging functionality is the isolated phase winding configuration resulting from its salient pole structure, making it the most suitable candidate for integrated drive-trains.

However, in the existing literature, the proposed ICs for SRM drive-train completely neglect their operating performance validation during the drive mode. Therefore, a discussion and possible shortcoming of the reconfigured traction converter and employed control technique during the drive mode of operation is equally crucial for validating the performance of the developed IC. The subsection following addresses the shortcomings during the driving and the charging mode of the IC proposed for the SRM drive-train separately.

Fig. 1.4 shows an EV drive-train with different enclosures available in the EV drive-train. For charging the BES via AC source, the OBCM is connected to a single-phase AC source via a SAEJ1772 5-pin connector, and for DC charging of the BES via an off-board DC charger, CHAdeMO or SAEJ1772 7-pin connector configuration is used. Nissan LEAF uses the shown connector configuration in Fig. 4 for AC and DC charging of the BES. **Fig. 1.5.** shows an EV drive-train with an IC. Here a SAEJ1772 7-pin connector is used for AC and DC charging of the BES.

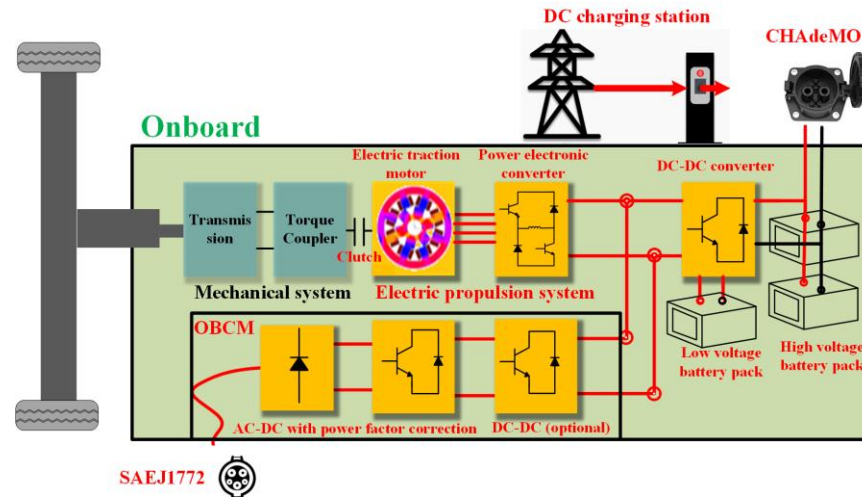


Fig. 1.4. EV drive-train with different enclosures for driving and charging modes.

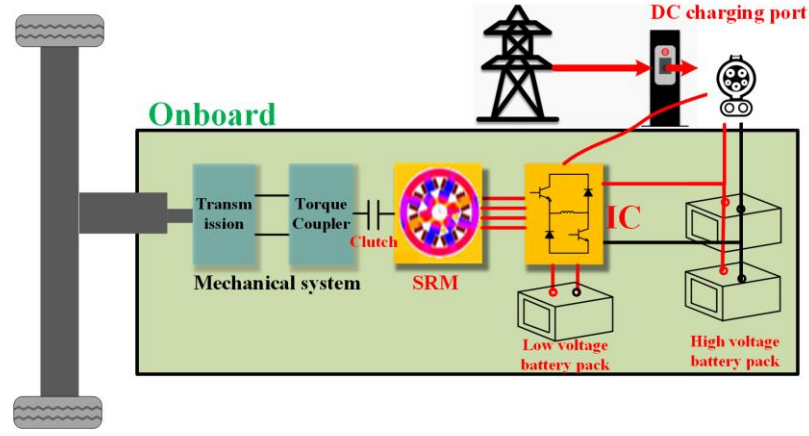


Fig. 1.5. EV drive-train with integrated converter.

1.2. LITERATURE REVIEW

1.2.1. CONTROL TECHNIQUE PROPOSED FOR SRM DRIVE

As mentioned in the previous subsection, the control techniques proposed for SRM drive have a restricted STOA due to the limited phase voltage applied by the conventional traction converter developed for SRM. Thus, various control techniques are proposed to improve the torque per ampere ratio and achieve torque ripple minimization, but they are restricted to a lower operating speed range only. In [20], constant current control (CCC) is implemented for SRM. However, the active phase excitation during its maximum slope of the inductance profile is not ensured with CCC. Hence [21] combines CCC with an optimization technique for exciting the active phase during its maximum slope of the inductance profile. In [22], different torque-sharing functions (TSF) are compared for maximum STOR range and efficiency. Moreover, it is shown that TSF results in an extended STOR range when adjacent phases are simultaneously conducted. With TSF, efficient commutation is achieved. However, the excitation of the active phase during the maximum slope of the inductance profile is not ensured, which results in a lower torque/ampere ratio.

In [23], direct instantaneous torque control (DITC) is proposed, wherein torque is instantaneously controlled. However, for higher operating speeds, the torque controller in DITC is saturated, limiting the STOR to 60%-70% of the base speed. In [24], DITC with a multi-phase torque-sharing algorithm is proposed. However, the operating speed range of the proposed algorithm is limited. Also, in [23] and [24], the active phase is not excited during the maximum slope of the inductance profile, which results in an increased RMS phase current and reduced efficiency.

In contrast to CCC, TSF, and DITC schemes, wherein the turn-on and turn-off angle/s for active phase/s are computed offline/online, the direct flux and torque control (DFTC) applies voltage vectors for total torque control [25] and [26]. Thus, with DFTC, the computational burden is reduced [26]. In the DFTC scheme, both the stator flux and torque are actively regulated [25] and [26]. However, the constant stator flux control loop in DFTC tends to excite the phases during the negative slope of the inductance profile [27]. It results in negative torque production, lower drive efficiency, and increased torque ripples. Hence, constant stator flux control is not recommended/ preferred for SRM [27]. In [28] and [29], the voltage vector selection rule of DFTC is modified, keeping the stator flux control loop. However, due to the constant stator flux control, the phases are excited in the negative region of the inductance profile, leading to a lower torque/ampere ratio. In [30] and [31], a

modification to DFTC is proposed wherein the stator flux is kept constant during commutating sectors only, and in other sectors, it is not controlled. However, the proposed control is sensitive to the flux reference and leads to higher torque ripples.

In [32] and [33], the stator flux control loop in DFTC is completely removed for 3-phase SRM. And instead of the stator flux angle, the inductance profile is used for sector identification. However, the proposed direct torque control (DTC) scheme in [32] and [33] have fixed sector widths that do not ensure active phase excitation during the maximum slope of the inductance profile, leading to restricted STOR.

One way to extend the STOR, discussed in [20], [21], and [33]-[37], is by extending the commutation region's width, i.e., wider phase overlap. The extended commutation width facilitates incoming phase energization in the lower $\frac{d\varphi(\theta,i)}{d\theta}$ region near to unaligned inductance position. And from (1.2), it is observed that excitation in the lower $\frac{d\varphi(\theta,i)}{d\theta}$ leads to a faster energization of the incoming phase current [20]. For 3-phase SRM, the inductance profile for adjacent phases does not overlap. Hence during extended commutation, the excitation of the incoming phase in the lower $\frac{d\varphi(\theta,i)}{d\theta}$ region does not contribute much to the total torque. Also, excitation in the lower $\frac{d\varphi(\theta,i)}{d\theta}$ region increases the RMS value and the corresponding copper losses [34]-[37].

The methods proposed in [34]-[37] extend the STOR for 3-phase SRM. However, it leads to restricted STOR when implemented for 4-phase SRM. Since with 4-phase SRM, the torque-producing inductance profile of adjacent phases overlaps. Thus, during extended commutation, both the incoming and outgoing phases contribute to the total torque of the 4-phase SRM if excited appropriately.

In the existing literature on DTC for 4-phase SRM, no work claims/extends the STOR to base speed. Thus, objective 1 of the thesis is to develop a control scheme for 4-phase SRM that allows simultaneous excitation of adjacent phases to extend the STOR, resulting in an improved torque/ampere ratio and minimized torque ripples. In this context, the motivation for chapter 2 of the thesis is to formulate/investigate a direct torque control technique that can later be applied to any integrated three-level or MLCT topologies available/ proposed for the SRM drive-train.

1.2.2 EXISTING ICS FOR SRM DRIVE-TRAIN DURING CHARGING MODE OF OPERATION

In [38] and [39], the proposed ICs integrate a modified miller converter and a buck-boost power factor correction (PFC) charger. However, with the proposed IC in [38], the current within the reconfigured inductors results in torque during charging, termed charging torque. Furthermore, the proposed IC in [39], instead of phase winding/s, employs an additional non-integrated circuit and an external inductor for realizing the PFC charger. Thus, zero charging torque (ZCT) with the phase winding reconfigured as inductors is not achieved via [38] and [39], implying the use of external braking, which is neither recommended nor practically feasible. In [40], the proposed IC integrates a modified asymmetrical half-bridge (AHB) and an inverting buck-boost PFC charger. Moreover, the current in the reconfigured inductors results in an instantaneous ZCT. However, ZCT is achieved at only one rotor position in an electrical cycle. Thus, for the 4-phase SRM, the maximum rotor displacement for reaching the nearest charging rotor position is 30° mechanical ($30^\circ * 6 = 180^\circ$ electrical).

The inverting buck-boost PFC charger configuration, integrated with the ICs proposed in [38]-[40] because of additional diodes in the rectifier bridge, increases the conduction losses [41]. Also, the inverting buck-boost PFC configuration, due to the indirect transfer of energy from the input to output via the inductor, results in lower charging efficiency. Thus, inverting buck-boost PFC configuration is unsuitable for high-power battery charging [42]. Among all the PFC charger configurations available, the bridgeless boost (BB) - PFC charger configuration achieves the highest efficiency and thus is widely adopted for PFC battery chargers [41], [42].

With the proposed IC in [43] and [44], a modified AHB converter and a bridgeless boost PFC (BB-PFC) charger are integrated. However, in [43], phase windings are split for realizing inductors during charging mode. The reconfigured split-phase windings result in ZCT at any rotor position. However, the requirement of a customized SRM and complex control limits the proposed IC application. And with the IC proposed in [44], the current flowing in reconfigured inductors results in charging torque production.

Thus, ZCT with the phase winding reconfigured as inductors is not achieved via [43] and [44]. Also, the IC proposed in [43] and [44] integrates a boost-type PFC charger. Thus, the battery voltage needs to be higher than the peak of the input AC voltage, which is not always the case. ICs proposed in [45] and [46] consider a more practical scenario wherein a two-stage PFC battery charger is integrated for charging the battery of voltage rating lower than the input AC voltage peak. The two-stage PFC charger is realized by BB-PFC stage cascade by buck DC converter (BDC).

The IC proposed in [45] requires additional non-integrated/external inductors for realizing the two-stage PFC charger. By having external inductors, the windings are not reutilized as active inductors during charging. Thus, full integration of driving and charging modes is not achieved. The ICs proposed in [46] integrate a two-stage battery charger wherein the phase windings of employed SRM are reutilized as inductors in the BB-PFC stage, and the single-phase AC grid is directly connected to winding nodes. However, to realize the two-stage PFC stage, an additional non-integrated two-quadrant DC-DC converter (TQDDC) along with an additional charging inductor is required between the BES and the traction converter. Thus, with the ICs proposed in [46], the charging operation is completed via BB-PFC reconfigured from the drive converter cascaded to the TQDDC, which is non-integrated. Also, during charging, the current flowing in the reconfigured phase windings result in charging torque, implying the use of external braking, which is neither recommended nor practically feasible in an actual EV application.

The above-discussed ICs for SRM drive-train, i.e., [38], [39], [43]-[46], do not achieve ZCT with phase winding/s reconfigured as inductor/s during charging operation. And thus, an external braking mechanism is used, which is neither recommended nor practically feasible in an actual EV application. Thus, the motivation for objective 2 and the corresponding chapter 3 of the thesis is to investigate a three-level integrated drive train that achieves average and/or instantaneous ZCT. Moreover, novel rotor positions are introduced that minimize the rotor displacement to the proposed charging rotor position from its initial parking position.

However, as discussed in the introduction, three-level converter topologies can only apply limited phase voltage which restricts the STOR during its drive mode of operation. Thus, the motivation for objective 3 and the corresponding chapter 4 of the thesis is to investigate an MLCT that can apply higher phase voltages during energization and de-energization. Moreover, the proposed MLCT integrates the driving and charging modes of

operation. In addition, the benefits achieved with the three-level IC drive train discussed/proposed in objective 2 are also achieved with the proposed MLCT in objective 3.

The aforementioned ICs cleverly eliminates the de-merit of OBC by integrating and comprehensively studying the numerous ways of integrating different PFC charger topologies for the SRM drive-train. However, the integrated charger topologies are powered via an AC grid, for which the energy is mainly derived from fossil fuels. Therefore, if the EVs are supplied primarily by AC grids, the main reason to come towards EV i.e., reducing the emission because of fossil fuels is unsatisfactory/ not achieved. To overcome the dependency on AC grids, the EV chargers must be powered via renewable energy sources, such as rooftop solar photovoltaic (PV) systems.

In this regard, another group of ICs for SRM drive-train integrating two-stage battery chargers are proposed in [47]-[52], wherein the single-phase AC grid does not directly connect to the phase windings. Instead, an additional non-integrated front-end rectifier/converter stage connects to the AC grid. Furthermore, the cascade interleaved BDC stage and its active inductors are derived from the drive converter and motor phase windings. Thus, with a non-integrated front end, the driving and charging modes of operation are partially integrated. Apart from partial integration, the ICs proposed in [47]-[52] increase the total switch count as an additional non-integrated front-end converter stage is required with these ICs.

Also, the reconfigured BDC stage functions as a unidirectional TQDDC that facilitates DC charging via a rooftop solar PV system. However, for the targeted application, the available footprint for the rooftop solar PV system is limited, resulting in restricted DC power leading to slow DC charging.

To make EVs more sustainable and practical to the current market, charging and discharging via a fast DC source/load, i.e., DC charging station, DC micro-grids, another vehicle BES, i.e., V2V charging/discharging, has been recently proposed by researchers [53]-[55]. For this, an additional bidirectional fast DC-OBC module is added to the EV drive-train [53]- [55]. However, a bidirectional fast DC-OBC module similar to an AC-OBC module increases costs and requires space within the EV drive train.

Thus bidirectional DC-OBC is integrated with the conventional AC motor drive-trains. However, [56] requires additional hardware to achieve integrated bidirectional fast DC-OBC. [57] eliminates additional hardware requirements, but the proposed IC configuration depends on the receiver EV IC configuration to achieve integrated bidirectional fast DC-OBC configuration. ICs in the existing literature on integrated SRM drive-trains do not integrate bidirectional fast DC-OBC.

Thus, the motivation for objective 4 and the corresponding chapter 5 of the thesis is to investigate an IC for an SRM drive-train that integrates driving, G2V charging, and fast V2V charging/discharging without the requirement of additional non-integrated components. **Table. I. I** provide the tabular comparison for all the ICs discussed above. **Table. I. I** has compared different ICs discussed above in terms of their total switch count and relay requirement for integrating different functionalities. From **Table. I. I** it is inferred that the ICs developed for SRM drive employ either a non-integrated TQDDC or a non-integrated rectifier unit to integrate driving, G2V charging, and/or slow unidirectional DC charging modes.

TABLE. I. I
COMPARISON OF EXISTING IC IN THE LITERATURE

Reference	Integrated G2V	Integrated V2G	Integrated DC charging (Unidirectional)	Switch + Diode count	Relay/Contactors requirement	Zero-torque during charging	No of charging positions and rotor displacement	Additional non-integrated components
[40]	√ Inverting Buck-Boost PFC Charger	×	×	18	√ [2]	√	1, and 30°	√ (TQDDC)
[38]	√ Inverting Buck-Boost PFC Charger	×	×	13	√ [1]	√	No	√ (TQDDC)
[46]	√ Two-Stage PFC Charger	√	×	18	×	√	No	√ (TQDDC)
[52]	√ Two-Stage PFC Charger	×	√ (Two-quadrant)	18	√ [5]	×	-	√ (Rectifier unit)
[49]	√ Two-Stage PFC Charger	×	√ (Two-quadrant)	20	√ [3]	×	-	√ (Rectifier unit)
[47]	√ Two-Stage PFC Charger	×	√ (Two-quadrant)	16	√ [3]	×	-	√ (Rectifier unit)

1. 3. MOTIVATION AND OBJECTIVES

The main motivation of the thesis is to address the shortcomings of the IC developed for SRM drive-train. But before addressing the shortcomings it is important to develop a control scheme for 4-phase SRM allowing simultaneous excitation of adjacent phases which results in extending the STOR and simultaneous results in an improved torque/ampere ratio and minimized torque ripples. In this context the motivation for objective-1 of the thesis is to develop a direct torque control technique that later be applied to any integrated three-level or MLCT topologies proposed for the SRM drive-train.

Also as discussed in the introduction the proposed ICs for SRM drive-train do not achieve ZCT during charging mode of operation and thus an external braking mechanism is used, which is neither recommended nor practically feasible in an actual EV application. Thus, motivation for objective-2 of the thesis is to propose a three-level integrated drive-train that achieves ZCT. Moreover, novel rotor positions are introduced that minimize the rotor displacement to the proposed charging rotor position from its initial parking position.

However as discussed in the introduction three-level converter topologies can only apply limited phase voltage which restricts the STOR during its drive mode of operation. Thus, the motivation for objective-3 is to propose an MLCT that can apply higher phase voltages during energization and de-energization. Moreover, the MLCT integrates driving and charging mode of operation. The contribution of the proposed three-level integrated drive-train in objective-2 are also achieved with the proposed MLCT in objective-3.

The ICs proposed above facilitates charging via single-phase AC grid only. However, due to limitations on maximum allowable power from a single-phase grid, single-phase battery chargers can take longer (6-10 hours) to charge the BESS completely. Thus, for faster charging of BES via DC sources, DC/vehicle-to-vehicle (V2V)

is adopted. Thus objective-4 of the thesis is to propose an IC that without any additional non-integrated circuit, integrates driving/G2V/V2G and DC/V2V charging with the least switch count. The proposed/discussed IC in objective-4, integrates a DC charger and a single-phase charger that facilitates faster charging of BES which is not achieved with the IC proposed in objective-2 and objective-3.

The IC discussed/ proposed in objective-2, objective-3 and objective-4 integrates a cascade/ two stage battery charging topology for the charging mode. However, cascade battery charging topology results in reduced charging efficiency. Thus, for the integrated battery charger to be operational over the universal input voltage range and to have the acceptable charging efficiency, a single-stage battery charger capable of operating simultaneously in buck, boost and buck-boost mode of operation must be integrated with the IC, which is the primary motivation for objective-5.

Moreover, the integrated three-level topology and MLCT proposed in objective-2 and objective-3 can be applied for even phase SRM. Thus, to achieve ZCT for n-phase SRM the secondary motivation for objective-5 of the thesis is to propose an integrated AHB-based SRM drive-train topology with driving and multiple charging capabilities. With integrated multiple charging the BES can be charged via AC and DC sources. Thus, charging via DC source allows faster charging of BES which is not achieved by IC topology proposed in objective-2 and objective-3. Also as stated the integrated battery charger with objective-5 integrates a single-stage battery charger which improves the charging efficiency when compare with the IC proposed in earlier objectives.

To summarize the objectives of the thesis are as follows.

Objective 1 – To develop a control technique for a 4-phase switched reluctance motor to achieve a high torque-ampere ratio with minimized torque ripples and extended smooth torque operating region.

Objective 2 – To develop an integrated driving/charging three-level SRM drive-train topology with zero charging torque for minimal rotor displacement.

Objective 3 – To develop an integrated driving/charging multi-level converter topology for SRM drive-train with zero charging torque production with improved smooth torque operating region.

Objective-4 – To develop an integrated converter for SRM drive-train with G2V, V2G and DC/V2V fast charging capabilities.

Objective-5 - To develop an integrated converter with charging capabilities over a wide input AC voltage with AHB-based SRM drive-train topology.

To address these objectives the chapters of the thesis are as follows:

Chapter-2 proposes a novel DTC scheme to extend the STOR for 4-phase SRM till the base speed. In the proposed DTC scheme, adjacent phases are simultaneously controlled for the maximum torque-producing inductance profile. Two novel sector reorganization schemes, i.e., DTC-I and DTC-II, are proposed where the sector widths are varied based on the real-time slope of the inductance profile.

Chapter-3 proposes an integrated converter (IC) with driving and battery charging features for electric vehicles (EVs) drive-train employing a 4-phase SRM. Moreover, charging operation is performed at appropriate rotor

positions, which results in a net-zero charging torque (ZCT) from the phases reconfigured as inductors. The proposed reconfiguration of inductors allows eight novel rotor positions for charging within an electrical cycle where ZCT is achieved. Thus, to reach the nearby rotor position for charging, the maximum displacement for the rotor is reduced to 3.75° mechanical, which any other IC does not achieve for the SRM drive.

Chapter-4 proposes a fully integrated multi-level power converter topology (IML-PCT) with integrated battery charging capability for SRM drive. The proposed IML-PCT applies higher energization and de-energization voltage during the driving mode, leading to an enhanced constant torque region for SRM drive. The contribution of the proposed three-level integrated drive-train in chapter-3 are also achieved with the proposed MLCT in chapter-4.

Chapter-5 proposes an IC with driving, grid-to-vehicle (G2V), vehicle-to-grid (V2G), and DC/ vehicle-to-vehicle (V2V) charging capabilities for EV drive-train employing SRM. When EV is standstill/ idle, the proposed IC can charge the battery via standard AC and DC charging sockets. For charging the battery via a single-phase residential/public AC outlet, i.e., G2V charging, the proposed IC exhibits a PFC charger. The reconfigured switches are bidirectional, facilitating the flow of power in both directions, i.e., G2V and V2G charging. For fast charging of the battery via DC source, which includes emerging DC grids, solar photovoltaic systems, and battery source of another EV, i.e., V2V charging, the proposed IC exhibits a four-quadrant DC-DC converter (FQDDC).

Chapter-6 proposes an IC that during battery charging mode, is utilized as an integrated OBC by reconfiguring it into a single-stage (n-2, n-3..., 1) phase interleaved buck cascaded buck-boost (IBuCBB) converter. The (n-2, n-3..., 1) charging inductors for the IBuCBB configuration are realized via the phase windings of the SRM. Thus, the proposed IC eliminates the requirement of an additional circuit for battery charging. The integrated OBC facilitates battery charging via a single-phase residential/public outlet, i.e., AC level-1 and AC level-2 charging, over a universally available input voltage range, i.e., 85-265 V rms (root mean square), with acceptable performance and efficiency. In addition, the proposed IC for n-phase SRM drives employees' same number of power electronic switches as in the conventional AHB converter for n-phase SRM.

CHAPTER 2

DIRECT TORQUE CONTROL TECHNIQUE FOR 4-PHASE SWITCHED RELUCTANCE MOTOR TO EXTEND SMOOTH TORQUE OPERATING REGION

The present chapter investigates a novel DTC scheme to extend the STOR for 4-phase SRM till the base speed. In the proposed DTC scheme, adjacent phases are simultaneously controlled for the maximum torque-producing inductance profile. Two novel sector reorganization schemes, i.e., DTC-I and DTC-II, are proposed where the sector widths are varied based on the real-time slope of the inductance profile. DTC-I operates in a lower speed range (up to 70% of the base speed), and DTC-II operates at a higher speed range (above 70% of the base speed). As per the author's best knowledge, the sector reorganization based on the real-time slope of the inductance profile is not available in the existing literature. Also, in the proposed DTC scheme, the constant flux control loop of DFTC is removed, and sector identification is based on the inductance profile as per [32] and [33].

In contrast to the available control techniques for 4-phase SRM, the proposed method offers the following advantages.

- The proposed DTC scheme, without any optimization technique, can excite the active phase in the maximum torque-producing region. However, with CCC and DITC, this is possible by applying optimization techniques that increase the computational burden.
- Unlike the DTC scheme discussed in [32] and [33], wherein the sector widths are fixed, the proposed DTC-I and DTC-II scheme allows the reorganization of the sector widths in real-time. Thus, with the proposed DTC schemes, the active phase is excited only during its maximum slope of the inductance profile, which is not achieved in [32] and [33].

2.1. GENERALIZED MODELING OF SIMULTANEOUS-PHASE EXCITED SRM (MATHEMATICAL BACKGROUND)

In this chapter section, the mathematical background of the instantaneous torque equation used in the proposed DTC for torque control is derived. The section also gives the non-linear static torque characteristics of the prototype 4-phase SRM, designed in ANSYS/ Maxwell. Also, the maximum possible torque output from the prototype 4-phase SRM, when the simultaneous phases are excited, is taken up for discussion.

2.1.1. THE INSTANTANEOUS TORQUE CONTROL EQUATION

This section presents a generalized approach to model a simultaneous phase excited SRM. The mutual effect due to simultaneous-phase excitation in 4-phase SRM is small, hence neglected for the analysis. In 4-phase SRM, any two phases are simultaneously excited at any operating instant to supply the maximum possible torque. Assuming two-phase windings in the motor are displaced in space with other at a particular angle, the voltage equation for simultaneously exciting two-phase winding can be written as (*assuming phase-A, and phase-B are excited about the discussion*)

$$\vec{v}_a + \vec{v}_b = r_a i_a + \frac{d\vec{\varphi}_a(\theta, i_a)}{dt} + r_b i_b + \frac{d\vec{\varphi}_b(\theta, i_b)}{dt} \quad (2.1)$$

where $\overrightarrow{\varphi}_k(\theta, i_k)$ is the non-linear flux-linkage of phase-K, with respect to its phase current (i_k) and rotor position (θ). And r_k is the stator winding resistance for phase-K. $\overrightarrow{v}_a + \overrightarrow{v}_b$, is the resulting voltage vector when phase-A and phase-B are excited. Neglecting the stator resistance, (2.1) can be rewritten as

$$\overrightarrow{v}_a + \overrightarrow{v}_b = \frac{d\overrightarrow{\varphi}_a(\theta, i_a)}{dt} + \frac{d\overrightarrow{\varphi}_b(\theta, i_b)}{dt}. \quad (2.2)$$

From (2.2), it is inferred that by applying the voltage vector ($\overrightarrow{v}_a + \overrightarrow{v}_b$), for a sufficiently small-time interval, Δt the change in combined stator flux vector ($\Delta\overrightarrow{\varphi}_{ab}$) can be expressed as

$$(\overrightarrow{v}_a + \overrightarrow{v}_b)\Delta t = \Delta\overrightarrow{\varphi}_{ab}(\theta, i_a, i_b) \quad (2.3)$$

where $\overrightarrow{\varphi}_{ab}(\theta, i_a, i_b)$ is the combined non-linear flux-linkage of phase-A and phase-B, with respect to its phase current and rotor position. Thus, the applied voltage vector ($\overrightarrow{v}_a + \overrightarrow{v}_b$) produces a change in the stator flux vector ($\Delta\overrightarrow{\varphi}_{ab}$) in the same direction as the resultant of ($\overrightarrow{v}_a + \overrightarrow{v}_b$) and is proportional to the time period it is applied for. The instantaneous torque can be defined as a derivative of mechanical energy with respect to rotor position and be given as

$$T_e = \frac{dW_{\text{mech}}}{d\theta} \quad (2.4)$$

where dW_{mech} is the differential change in mechanical energy with respect to its rotor position. From the above equation, the total torque in the simultaneous-phase excited SRM can be given as

$$T_{e,ab}(\theta, i_a, i_b) = \overbrace{T_{e,a}(\theta, i_a)}^{A \text{ phase excitation}} + \overbrace{T_{e,b}(\theta, i_b)}^{B \text{ phase excitation}}, \quad (2.5)$$

$$T_{e,ab}(\theta, i_a, i_b) = i_a \frac{\partial \overrightarrow{\varphi}_a(\theta, i_a)}{\partial \theta} + i_b \frac{\partial \overrightarrow{\varphi}_b(\theta, i_b)}{\partial \theta} - \frac{\partial W_{\text{field}}}{\partial \theta}. \quad (2.6)$$

The first term in (2.5) denotes the torque of phase-A, due to current in phase-A winding only. The second term denotes the torque of phase-B due to the current in phase-B winding only. Hence the simultaneous-phase excitation model can be simplified to two single-phase excitation models, both applied together with respect to the rotor position.

All the above equations (2.1) - (2.6) hold good for a system with non-linear saturating magnetizing characteristics such as SRM. Also, SRM is designed to operate in magnetic saturation, and it can be stated that the influence of $\frac{\partial W_{\text{field}}}{\partial \theta}$ in (2.6) is negligible. If the magnetizing characteristics are assumed to be linear, then the approximate instantaneous torque equation for simultaneous phase excitation can be written as

$$\overrightarrow{T}_{e,ab}(\theta, i_a, i_b) = i_a \frac{d\overrightarrow{\varphi}_a(\theta, i_a)}{d\theta} + i_b \frac{d\overrightarrow{\varphi}_b(\theta, i_b)}{d\theta}. \quad (2.7)$$

Assuming i_a and i_b are same for the time instant considered, the resulting current can be given by i_x .

$$\overrightarrow{T}_{e,ab}(\theta, i_a, i_b) = i_x \left(\frac{d\overrightarrow{\varphi}_{ab}(\theta, i_a, i_b)}{d\theta} \right). \quad (2.8)$$

From (2.3) and (2.8), the instantaneous torque equation for a sufficiently small-time interval Δt can be given as

$$\vec{T}_{e,ab}(\theta, i_a, i_b) = i_x \frac{d\vec{\varphi}_{ab}(\theta, i_a, i_b)}{d\theta} = i_x \frac{(\vec{v}_a + \vec{v}_b)\Delta t}{d\theta}. \quad (2.9)$$

From (2.9), it is seen that in unipolar current-controlled SRM, the instantaneous torque ($\vec{T}_{e,ab}$) output due to the simultaneous excitation of phase-A and phase-B depends on the change in the stator flux vector magnitude ($\Delta\vec{\varphi}_{ab}$), with respect to the change in the rotor position ($\Delta\theta$).

In other words, the change in the stator flux magnitude with respect to the rotor position controls the instantaneous torque in SRM. That is to achieve positive torque the magnitude of the stator flux vector ($\vec{\varphi}_{ab}$) should be increased in the positive direction of rotation. Also, from (2.9), it is observed that the change in stator flux magnitude ($\Delta\vec{\varphi}_{ab}$), responsible for instantaneous torque production, can be achieved by applying a voltage vector ($\vec{v}_a + \vec{v}_b$) for a small-time interval Δt .

Thus, by applying the appropriate voltage vectors for a particular rotor position, one can directly control the instantaneous torque of the 4-phase SRM. The proposed DTC technique uses the concepts developed above for instantaneous torque control of 4-phase SRM, where two simultaneous phases are excited, which is discussed in the following section.

2.2. PROPOSED DIRECT TORQUE CONTROL TECHNIQUE

In the proposed DTC scheme, the constant flux control of the DFTC scheme is removed, and only control over instantaneous torque is done. After the removal of the flux control loop, the sector identification in the proposed DTC scheme is based on the actual inductance profile, which is rotor-position dependent. Also, the voltage vector and its selection rule are modified for instantaneous torque control, which is discussed in subsequent subsections.

2.2.1 SECTOR FORMATION BASED ON ACTUAL INDUCTANCE PROFILE.

The SRM model in ANSYS/Maxwell and the obtained inductance profile ($L_a(\theta, i_a)$) and torque profile ($T_a(\theta, i_a)$) are shown in **Fig. 2.1. (a)** and **Fig. 2.2. (b)**, respectively. **Fig. 2.1. (a)** shows the inductance profile for phase-A, of the prototype 4-phase SRM, for the different operating phase currents with respect to the rotor position. The initial rotor position in ANSYS/Maxwell is kept at 22.5° mechanical so that phase-A is at its unaligned position at 22.5° mechanical, as shown in **Fig. 2.1. Fig. 2.2.** shows the actual inductance profile with unaligned and aligned positions for all marked phases. The inductance profile is shown for the rated phase current of 11A.

Also, the corresponding electrical angle and sector formation is shown. Phase-A unaligned inductance position is taken as a reference for the sector formation. The complete electrical cycle is partitioned into eight sectors, as shown in **Fig. 2. 2.**

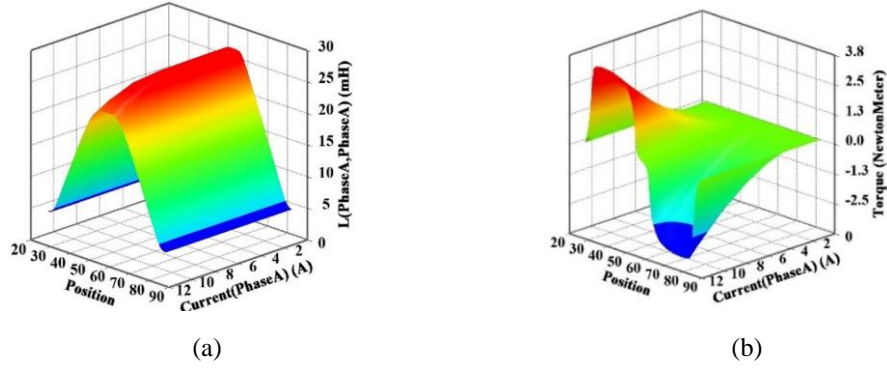


Fig. 2.1. (a). Self-inductance profile of phase-A, for different operating currents. (b) Estimated torque of phase-A, for different operating currents.

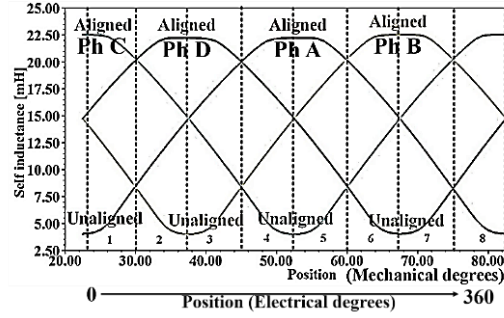


Fig. 2.2. Inductance profile of the prototype 4-phase SRM obtained from ANSYS/Maxwell, at phase current of 11 A.

2.2.2 VOLTAGE VECTORS AND THEIR SELECTION RULE FOR TORQUE CONTROL

In a 3-level asymmetrical half-bridge (AHB) converter configuration, each phase can have three possible phase voltage combinations. First, when positive phase voltage is applied to the phase windings, which is denoted by 1. Second, when zero voltage is applied to the phase winding, which is denoted by 0, and third when the negative voltage is applied to the phase windings denoted by -1.

For 4-phase SRM with a 3-level AHB converter, 81 voltage vector combinations are possible. For the proposed DTC scheme, only 16 voltage vector combinations are selected so that the phases are excited during positive torque, producing inductance profile only. The selected voltage vectors with their direction are shown in **Fig. 2.3**. For voltage vector direction, the phase-aligned axis, as shown in **Fig. 2.3. (a)** is taken as the reference. **Table.II. I** gives the magnitude of all the selected voltage vectors. Voltage vectors \vec{V}_{x-} , where $x = \epsilon (1 - 8)$ are in the same direction as that of \vec{V}_{x+} , but are smaller in magnitude. The reason for selecting \vec{V}_{x+} and \vec{V}_{x-} , for instantaneous torque control is discussed below.

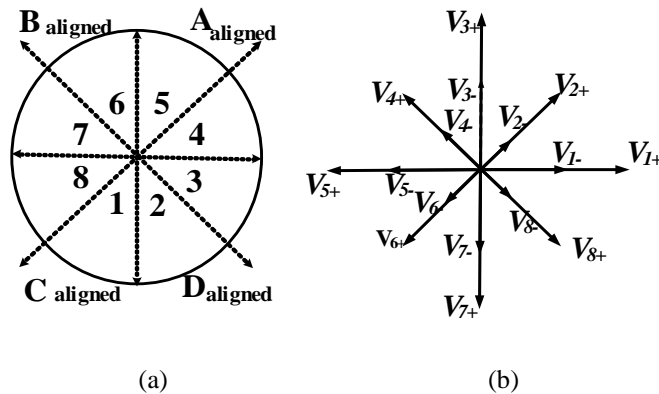


Fig. 2.3. (a) Sector diagram in one electrical space. (b) Voltage vectors in simultaneous phase excited 4-phase SRM.

TABLE. II. I
VOLTAGE VECTORS TABLE

Vector Notation	Magnitude	Vector Notation	Magnitude
V_{1+} (1, -1, -1, 1)	$2.82 V_{dc}$	V_{1-} (0, -1, -1, 0)	$1.41 V_{dc}$
V_{2+} (1, -1, -1, -1)	$2 V_{dc}$	V_{2-} (0, -1, -1, -1)	V_{dc}
V_{3+} (1, 1, -1, -1)	$2.82 V_{dc}$	V_{3-} (0, 0, -1, -1)	$1.41 V_{dc}$
V_{4+} (-1, 1, -1, -1)	$2 V_{dc}$	V_{4-} (-1, 0, -1, -1)	V_{dc}
V_{5+} (-1, 1, 1, -1)	$2.82 V_{dc}$	V_{5-} (-1, 0, 0, -1)	$1.41 V_{dc}$
V_{6+} (-1, -1, 1, -1)	$2 V_{dc}$	V_{6-} (-1, -1, 0, -1)	V_{dc}
V_{7+} (-1, -1, 1, 1)	$2.82 V_{dc}$	V_{7-} (-1, -1, 0, 0)	$1.41 V_{dc}$
V_{8+} (-1, -1, -1, 1)	$2 V_{dc}$	V_{8-} (-1, -1, -1, 0)	V_{dc}

Assuming $\overrightarrow{\varphi_{\alpha\beta}(k)}$ represents the current rotor position of the stator flux vector, which is in sector-4 at time instant (k) in the $\alpha\beta$ plane, as shown in **Fig. 2.4. (a)**. And at (k) time, instant voltage vector V_{4+} is applied to $\overrightarrow{\varphi_{\alpha\beta}(k)}$, for a sufficiently small-time interval, Δt , to have a resulting flux vector $\overrightarrow{\varphi_{\alpha\beta}(k+1)}$ at time instant (k+1). The change in stator flux magnitude is given by

$$\overrightarrow{\varphi_{\alpha\beta}(k+1)} - \overrightarrow{\varphi_{\alpha\beta}(k)} = (\overrightarrow{V_{x\pm}})\Delta t. \quad (2.10)$$

By applying V_{4+} , the change in stator flux magnitude with respect to the change in the rotor position (θ_i) is positive (i.e., flux acceleration), as shown in **Fig. 2.4. (a)**. Thus, the flux acceleration leads to an increase in the instantaneous torque given by (2.9).

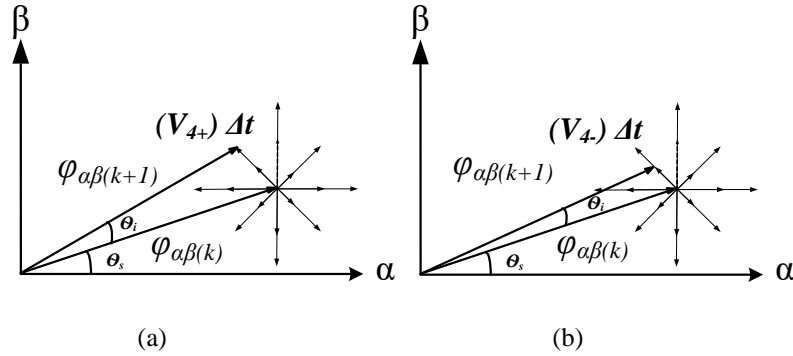


Fig. 2.4. (a). Flux vector position to obtain the maximum change in $\overrightarrow{\varphi_{\alpha\beta}(k)}$. **(b)** Flux vector position to obtain the minimum change in $\overrightarrow{\varphi_{\alpha\beta}(k)}$.

If instead of V_{4+} , V_{2+} or V_{3+} is applied, it also results in a positive torque change. But since the torque for SRM is rotor position sensitive, applying V_{2+} or V_{3+} leads to more magnitude of phase-A current due to saturation in the phase-A inductance profile. Thus, for sectors 2, 4, 6, and 8, vectors V_{2+} , V_{4+} , V_{6+} , and V_{8+} , respectively, are applied, wherein only a single phase is energized in such a way that none of the phases operates during saturation in inductance profile. Similarly, from **Fig. 3.2**, it is seen that in sectors 1, 3, 5, and 7, two simultaneous

phases can be energized as for them $\frac{dL(\theta,i)}{d\theta}$ is maximum and lies in the linear range. Thus, for sectors 1, 3, 5, and 7, vectors V_{1+} , V_{3+} , V_{5+} , and V_{7+} , respectively, are applied.

The above-discussed approach is applicable for increasing the instantaneous torque. To decrease the instantaneous torque, the phase that is/are in the active state is/are de-energized. This is achieved by applying a zero-phase voltage to the active phase winding/s. And because of the BEMF, the phase current and the corresponding phase torque reduce, which can be inferred from (2.9).

For decreasing instantaneous torque, V_{4-} is applied to $\overrightarrow{\varphi_{\alpha\beta(k)}}$, as shown in **Fig. 2.4. (b)**, to have a resulting flux vector $\overrightarrow{\varphi_{\alpha\beta(k+1)}}$ at time instant $(k+1)$, which results in a decrease in stator flux magnitude. It simultaneously maintains the change in the rotor position (θ_i) in the direction of rotation. The detailed voltage vectors with respect to the sector for positive change in instantaneous torque $T_{err}(+)$ and negative torque change $T_{err}(-)$ are mentioned in **Table. II. II**.

TABLE. II. II
VOLTAGE VECTOR SELECTION TABLE

Sector	1	2	3	4	5	6	7	8
$T_{err}(+)$	V_{1+}	V_{2+}	V_{3+}	V_{4+}	V_{5+}	V_{6+}	V_{7+}	V_{8+}
$T_{err}(-)$	V_{1-}	V_{2-}	V_{3-}	V_{4-}	V_{5-}	V_{6-}	V_{7-}	V_{8-}

2.3. SECTOR REORGANIZATION IN THE PROPOSED DTC SCHEME

The torque output for SRM is dependent on the inductance profile, which is dependent on the rotor position. Thus, the torque for SRM is rotor position sensitive. As adopted in [32] and [33], having sectors of fixed widths results in the excitation of phase in regions where the slope of inductance profile is not maximum, resulting in poor torque performance.

Hence in the proposed DTC scheme, sector boundaries are rearranged in real-time. The corresponding sector's boundaries define the energization and de-energization of the phase corresponding to the maximum slope of the inductance profile.

2.3. 1. DTC-I

For 4-phase SRM, the torque-producing inductance profile overlaps; hence, there is no need to completely energize the incoming phase in the lower inductance region. However, early turn-on of the incoming phase is advantageous, as it reduces the phase flux linkage peak, resulting in lower iron losses. Also, the duty cycle for the incoming phase, if set to 100%, limits the STOR range and reduces efficiency [32] and [33].

Hence, in the proposed sector partition, the starting of sector 1 is fixed at the position where $\frac{dL(\theta,i_a)}{d\theta}$ for phase-A is zero with respect to the actual inductance profile, shown by the solid line in **Fig. 2.5**. Actively regulating the incoming phase, i.e., phase-A in sector 1, allows its partial energization in the lower $\frac{dL(\theta,i_a)}{d\theta}$ region. Similarly, the starting of sectors 3, 5, and 7 are fixed at the position where $\frac{dL(\theta,i)}{d\theta}$ is zero for phase-B, phase-C and phase-D, respectively. Also, due to the symmetry of the inductance profile, the sectors 1, 3, 5, and 7 are equidistant from one another, i.e., 90° electrical, as shown in **Fig. 2.5**.

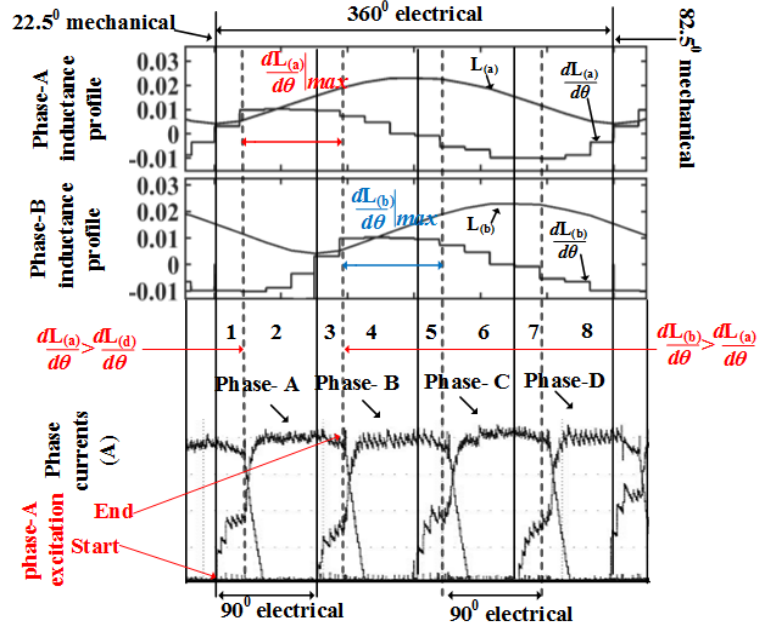


Fig. 2.5. Reorganized sector widths for DTC-I, and the corresponding experimentally obtained phase currents.

According to (2.9) and **Fig. 2.1**, excitation of the active phase in maximum $\frac{dL(\theta,i)}{d\theta}$, results in maximum torque production. The adjustable sector boundaries, i.e., starting of sectors 2, 4, 6, and 8, marked with dotted lines in **Fig. 2.5**, are fixed at the rotor position wherein $\left(\frac{dL(\theta,i)}{d\theta} \text{ incoming phase}\right) > \left(\frac{dL(\theta,i)}{d\theta} \text{ outgoing phase}\right)$. **Fig. 2.5** shows the inductance profile and the $\frac{dL(\theta,i)}{d\theta}$ ratio for phase-A and phase-B. Here the starting boundary of sector 4 is marked at the position wherein $\left(\frac{dL(\theta,i)}{d\theta} \text{ phase-B}\right) > \left(\frac{dL(\theta,i)}{d\theta} \text{ phase-A}\right)$. Again, due to symmetry in the inductance profile, the adjustable boundaries are also equidistant from one another, i.e., 90° electrical, as shown in **Fig. 2.5**. The DTC-I scheme is summarized below:

- By implementing DTC-I, a smooth transition of the total torque is achieved during commutation, as shown in **Fig. 2.6**. In **Fig. 2.6**, the torque output during commutation of total torque from phase-A to phase-B is shown. During DTC-I, the incoming phase excitation is controlled, along with the outgoing phase, to achieve efficient commutation with reduced torque ripples.

- With DTC-I, the active phase is excited during the period of the maximum positive slope of the inductance profile. This is achieved by reorganizing the sector widths in real-time by monitoring the slope of the inductance profile with respect to the operating current.

Fig. 2.7 shows the flowchart for real-time sector reorganization for adjustable sector boundaries, i.e., starting of sectors 2, 4, 6, and 8 in DTC-I. The operating current and the rotor position are the inputs to the sector reorganization scheme. The phase inductance is calculated using the look-up table, as shown in **Fig. 2.1 (a)**. Thus, the saturating effect at higher operating currents is considered with the proposed DTC schemes.

The $\frac{dL(\theta,i)}{d\theta}$ ratio of any two adjacent phases is calculated in the digital controller and is monitored for $\left(\frac{dL(\theta,i)}{d\theta} \text{ incoming phase}\right) > \left(\frac{dL(\theta,i)}{d\theta} \text{ outgoing phase}\right)$, as shown in **Fig. 2.7**.

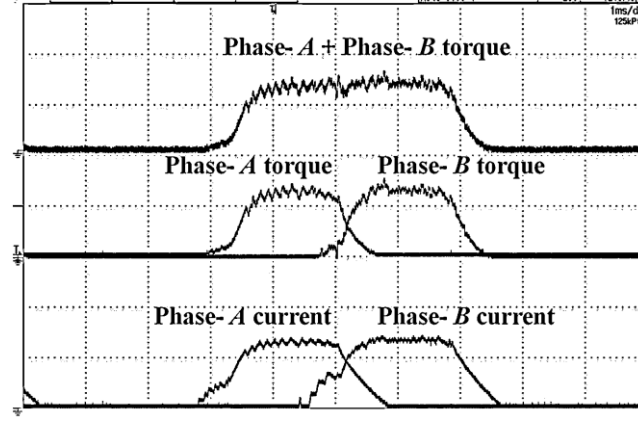


Fig. 2.6. Experimental results at 1500 rpm and 3 N-m. Total torque output during commutation and torque contribution individual phase-A and phase-B. Torque: 2 N-m/div, current: 10 A/div, and time: 1ms/div.

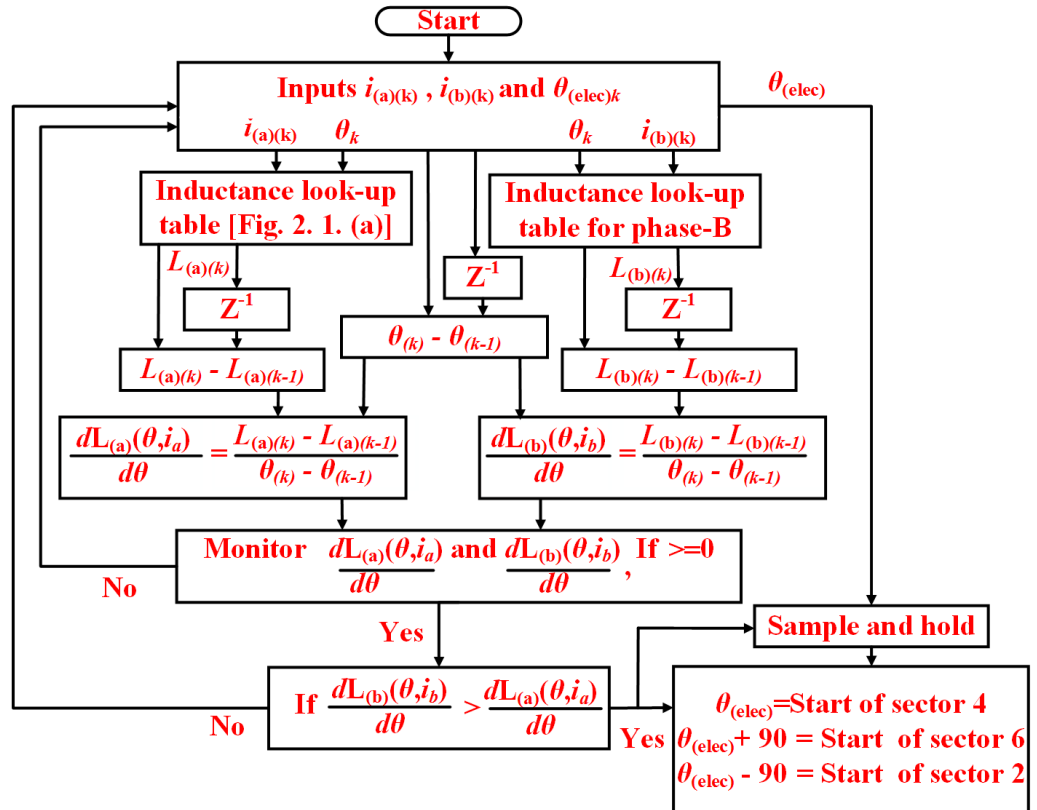


Fig. 2.7. Flowchart representing real-time sector-reorganization for adjustable sector boundaries, i.e., starting of sector 2, 4, 6, and 8 in DTC-I.

However, the proposed DTC-I has a limitation during higher operating speeds. As with an increase in the operating speed, the available energization time for the incoming phase decreases. And if the outgoing phase is de-energized before the energization of the incoming phase, then torque ripple is increased during commutation. The entire electrical cycle is further modified to avoid the above situation when torque ripple exceeds 30%, which is discussed below. The transition from DTC-I to DTC-II at 30% torque ripple is user-defined. It is observed experimentally that DTC-I is able to minimize torque ripples to 30% of the load torque till 70% of the base speed. Beyond 70% of the base speed, the controller switches to DTC-II.

2.3.2. DTC-II

To extend the STOR for the complete operating speed range, the outgoing phase has to support the incoming phase in total torque production. Moreover, during this extended commutation region, torque from the incoming and the outgoing phases has to be simultaneously regulated for smooth torque output. Torque ripples are monitored in the controller, and if torque ripple exceeds 30% of the load torque, then the controller in real-time varies the adjustable boundaries, as discussed below.

Similar to DTC-I, the starting of sectors 1, 3, 5 and 7 in DTC-II are fixed at positions where $\frac{dL(\theta, i_a)}{d\theta}$ for the corresponding phase is zero, as shown in **Fig. 2.8**. But with DTC-II, the adjustable boundaries are varied such that the incoming phase energization time increases; meanwhile, the outgoing phase regulates the total torque.

Thus, in DTC-II, adjacent phases are excited simultaneously for total torque production. According to (3.9), when adjacent phases are simultaneously excited, the total torque is given by the addition of individual phase torque. **Fig. 2.9** shows the total torque produced when phase-A is excited at 11A, and phase-D, phase-B current varies from 0A to 11A. It is observed that the corresponding rotor position where maximum torque is obtained during simultaneous excitation of adjacent phases is not similar to the corresponding rotor position where maximum torque is obtained during phase-A excitation only. **Fig. 2.1. (b)** shows the developed torque due to phase-A excitation only.

Thus, to have maximum torque from the simultaneous excitation of adjacent phases, the $\left(\frac{dL(\theta, i)}{d\theta} \right)_{incoming} + \left(\frac{dL(\theta, i)}{d\theta} \right)_{outgoing}$ should be monitored. In DTC-II, the $\left(\frac{dL(\theta, i)}{d\theta} \right)_{incoming} + \left(\frac{dL(\theta, i)}{d\theta} \right)_{outgoing}$ is tracked for its maximum value in the direction of rotation. And the adjustable boundaries are extended till $\left(\frac{dL(\theta, i)}{d\theta} \right)_{incoming} + \left(\frac{dL(\theta, i)}{d\theta} \right)_{outgoing}$ ceases out to be maximum, as shown in **Fig. 2.8**. **Fig. 2.8** shows the $\frac{dL(\theta, i)}{d\theta}$ ratio for phase-A, phase-B, and phase-A + phase-B. **Fig. 2.10** show the flowchart for real-time sector reorganization in DTC-II.

By implementing the above-discussed logic, the STOR can be extended to the base speed. But unlike the DTC-I scheme discussed above, in DTC-II, the active phases are not always excited during the maximum slope of the inductance profile. These results in lower efficiency compared to the DTC-I scheme, discussed in next section of the chapter.

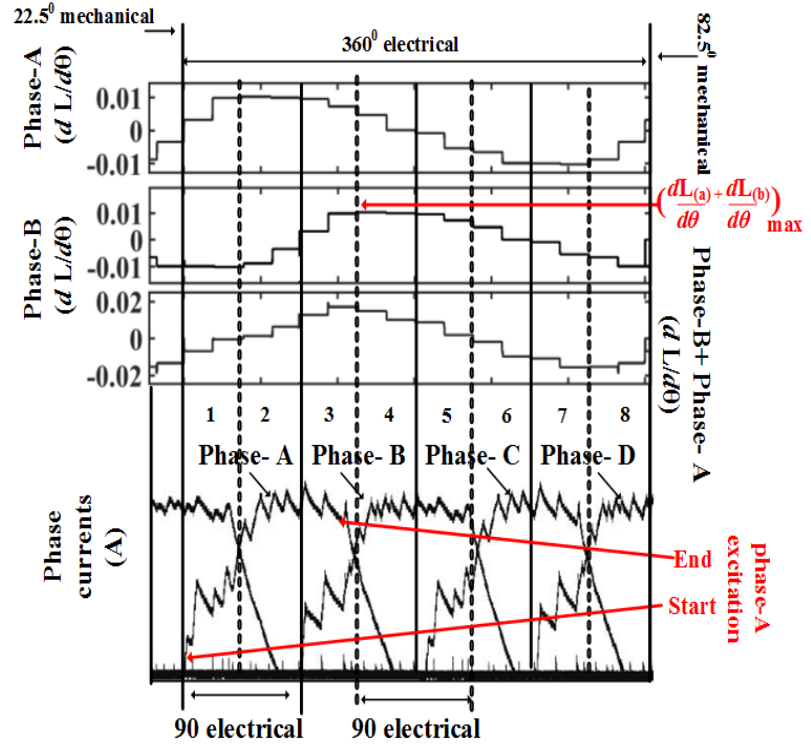


Fig. 2.8. Reorganized sector widths for DTC-II and the corresponding experimentally obtained phase currents.

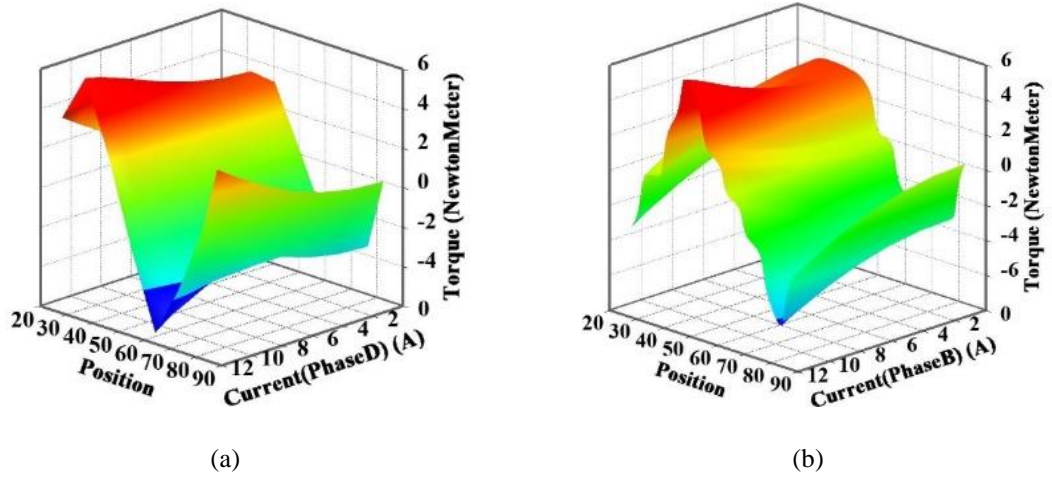


Fig. 2.9. (a) $T_{e,ad}(\theta, i_a = 11 \text{ A}, i_d \{0 \text{ A} \rightarrow 11 \text{ A}\})$, and (b) $T_{e,ab}(\theta, i_a = 11 \text{ A}, i_b \{0 \text{ A} \rightarrow 11 \text{ A}\})$.

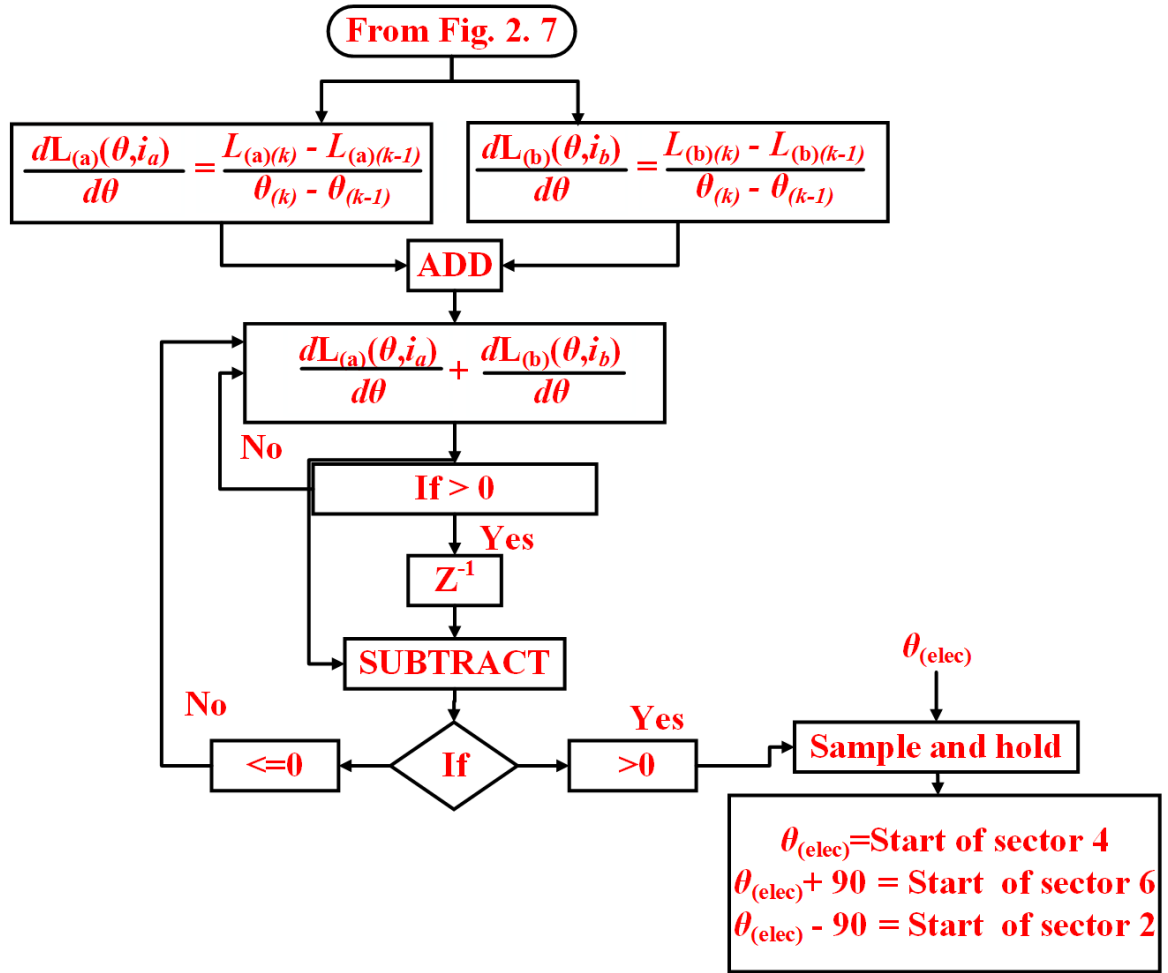


Fig. 2.10. Flowchart representing real-time sector reorganization for adjustable sector boundaries, i.e., starting of sector 2, 4, 6, and 8 in DTC-II.

2.4. IMPLEMENTATION OF PROPOSED DIRECT CONTROL TECHNIQUE SCHEME- EXPERIMENTAL RESULTS

In order to verify the proposed DTC algorithm, simulation and hardware tests are carried out on a 2.2 kW peak power, 3000 rpm, 4-phase 8/6 SRM. The motor parameters are provided in the appendix. A 4-phase AHB converter is designed with eight SKM75GB12T4 IGBT switches. And for the digital implementation, TMS320-F28379D DSP with a sampling frequency of 50 kHz (20 μ s) is used. For speed and position measurement, an incremental encoder with a 1024 pulse per revolution (BAUMER-EIL580-T) is used and is synchronized with the position sensor for accurate position detection. The position sensor is placed in such a way that it gives the information for phase-A unaligned inductance position, which is essential for sector formation.

The 4-phase SRM used for the experiment is designed in ANSYS/Maxwell. As shown in **Fig. 2.1. (b)**, the static torque-current-position characteristics data is used to estimate the actual torque by measuring the phase current and rotor position. For phase currents measurement, four current sensors (LA55-P) are used. The current sensor data is taken into the DSP controller using an analog-to-digital converter (12-bit).

The total estimated torque is compared with the reference torque (T_{ref}) and is given to a 2-level torque hysteresis comparator, and the torque error (T_{err}) is given by

$$T_{ref} - T_e = T_{err}$$

$$T_{ref} - T_e \geq (T_{band} / 2) = T_{err}(+)$$

$$T_{ref} - T_e \leq -(T_{band} / 2) = T_{err}(-)$$

where T_e is the estimated output motor torque, and T_{band} is the torque hysteresis band. In the proposed system PI controller is employed to derive the T_{ref} and implement the closed-loop speed control. The T_{band} is set to 0.44 N-m, which is 15% of the load torque (3N-m) to limit the maximum switching frequency to 15 kHz, which is obtained by simulation and experimental verification.

Depending on the T_{err} and corresponding sector/rotor position, a suitable voltage vector given in **Table. II** is applied to control the instantaneous torque. The instantaneous torque is converted to an analog signal through a 12-bit digital-to-analog converter for observation purposes. For sector reorganization, the static inductance-current-position characteristic is stored in the DSP and is monitored for $\frac{dL(\theta, i)}{d\theta}$ ratio for varying the sector widths in real-time.

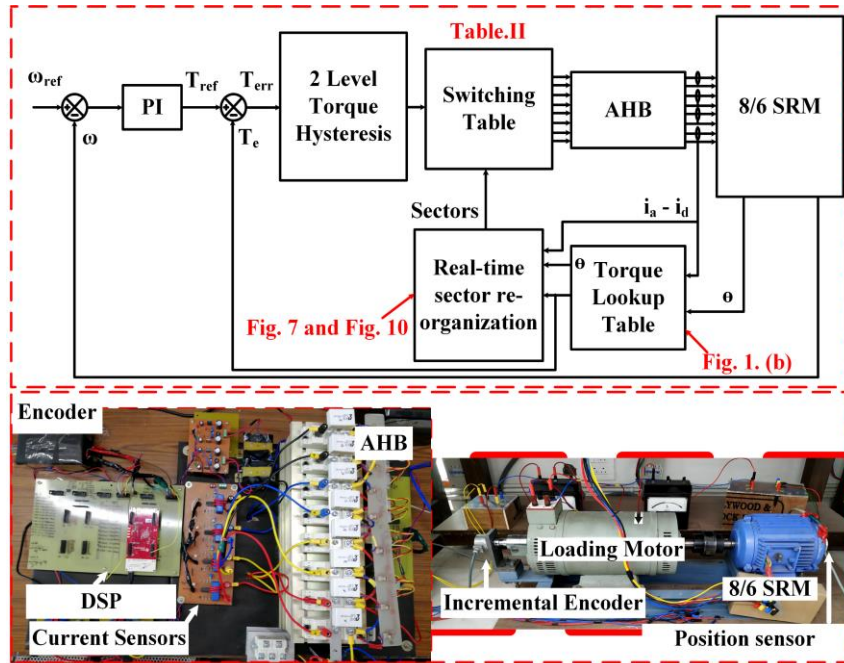


Fig. 2.11. Schematic diagram with the experimental setup.

A DC generator is used to load the 4-phase SRM. And the DC generator is connected to a bidirectional power supply (ITECH-6012B), which is used in constant current mode for varying the load. The bidirectional power also measures the loading power (in watts), and this output power is used while plotting the efficiency curve, considering the losses in the DC generator. The schematic diagram with the experimental setup is shown in **Fig. 2.11**.

For showing the efficacy of the proposed DTC schemes, it is compared with the conventional CCC and DITC schemes. For comparing maximum torque ripple, results of the conventional schemes and the proposed DTC schemes are compared at rated load condition.

Fig. 2.12 and **Fig. 2.13** show the experimental results for the conventional control scheme. For the shown results, the turn-on and turn-off angles for phase-A are set to 23.5° and 41.5° mechanical, respectively, and the load torque is maintained at 3 N-m. **Fig. 2.12** shows the experimental waveforms when the motor operates at

500 rpm and 1500 rpm, with the CCC scheme, where the current hysteresis width is set to 0.6 A for achieving a maximum switching frequency of 15 kHz. As the total torque from the incoming and the outgoing phase is not regulated during commutation, it results in 50 % higher torque ripples when compared with the proposed DTC-I scheme.

The experimental results of the conventional DITC scheme, as proposed in [23] are shown in **Fig. 2.13**. In conventional DITC, the phases are excited in lower $\frac{dL(\theta,i)}{d\theta}$ region, which results in peak phase current. Also, resulting in higher torque ripples when operating at rated load conditions, as shown in **Fig. 2.13**.

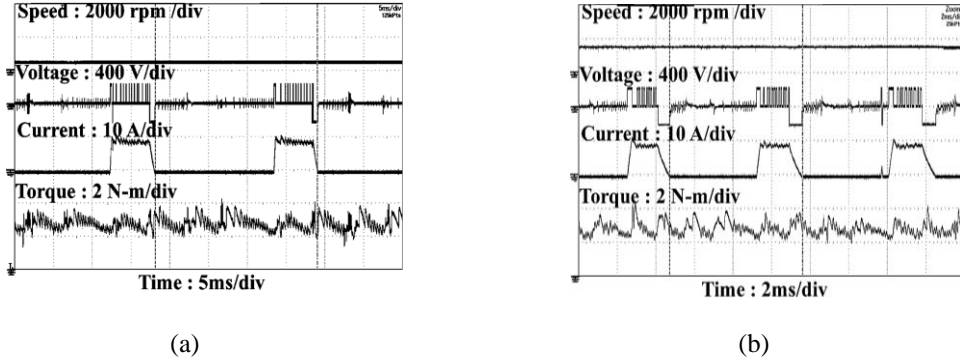


Fig. 2.12. Experimental waveforms of conventional CCC for a load torque of 3 N-m. (a) 500 rpm, and (b) 1500 rpm.

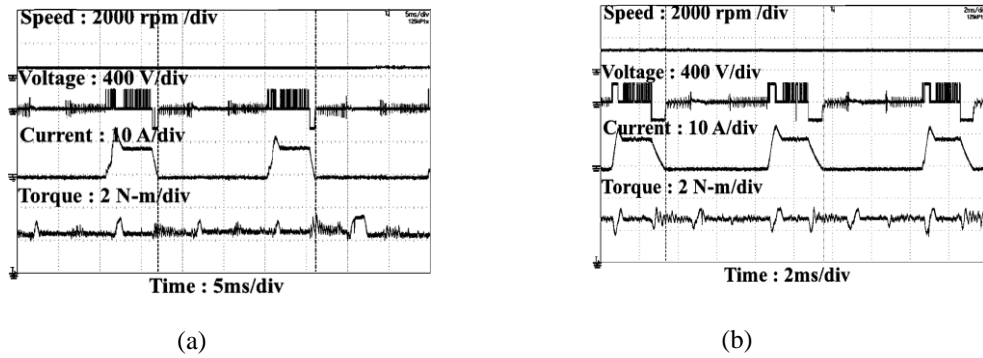


Fig. 2.13. Experimental waveforms of DITC for a load torque load of 3 N-m. (a) 500 rpm, and (b) 1500 rpm.

The phase voltage, phase current, and torque response of the proposed DTC-I scheme for 500 rpm and 1500 rpm at a load of 3 N-m are shown in **Fig. 2.14**. The sector width is kept according to the DTC-I, as discussed. With the DTC-I scheme, the corresponding ripples in torque profile for 500 rpm and 1500 rpm is 15% -20 % of the load torque.

From **Fig. 2.14. (b)** it is observed that even at 1500 rpm, the proposed DTC-I scheme is able to regulate the torque within 20% of the torque band. Also, the torque controller is not saturated, as by applying phase voltage, the DTC-I scheme is able to regulate the phase current.

Fig. 2.15 shows the speed and load dynamical response of the proposed DTC scheme. For speed dynamical response, as shown in **Fig. 2. 15. (a)**, the operating speed is changed from 1000 rpm to 1500 rpm and then from 1500 rpm to 1000 rpm, at a constant load of 1 N-m. When speed reference is varied, the required phase current and total torque are adjusted accordingly. Hence to track the increased reference speed, the current and the torque values are increased within the acceptable range. And to track the decrease in speed, the controller makes the

current and torque zero since the proposed voltage vector selection scheme does not allow negative torque in the system.

For the dynamical load response, as shown in **Fig. 2.15. (b)**, the load torque is changed from 1 N-m to 3 N-m and then from 3 N-m to 1 N-m at a constant speed of 1500 rpm. From the result, it is observed that the operating speeds vary to counter the effect of increase and decrease in the load torque.

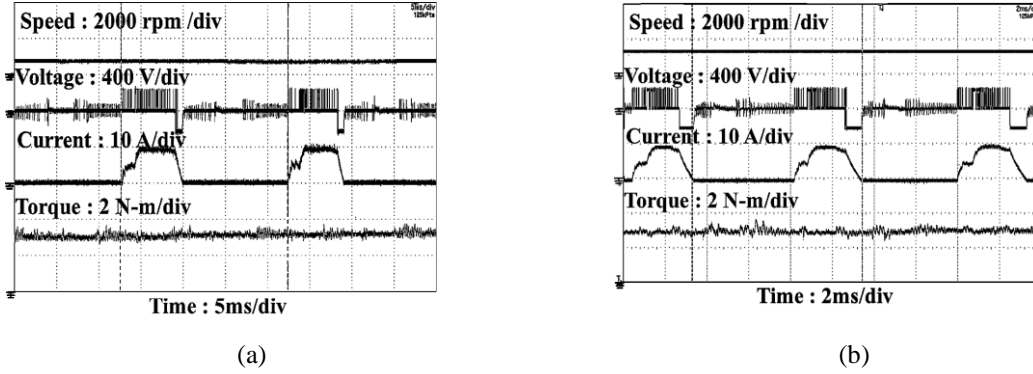


Fig. 2.14. Experimental waveforms of the proposed DTC-I scheme for a load torque of 3 N-m. (a) 500 rpm. (b) 1500 rpm.

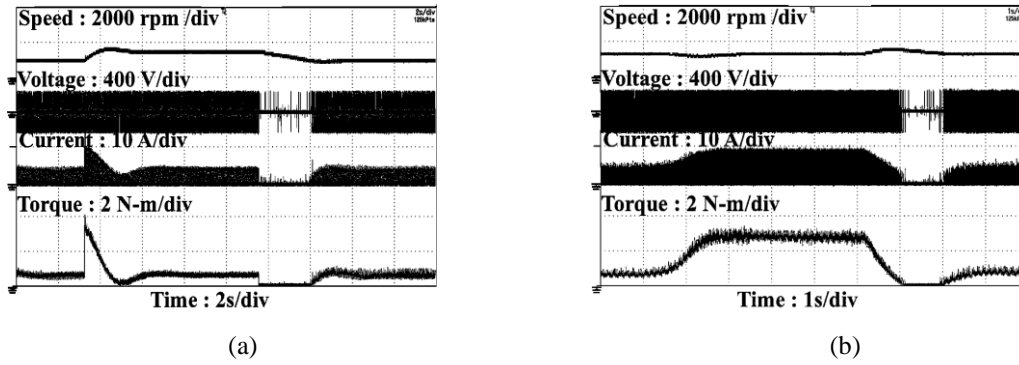


Fig. 2.15. (a) Experimental waveforms of DTC-I for speed change at constant load of 1 N-m. (b) Experimental waveforms of DTC-I for load change at 1500 rpm.

From the experimental results, it is observed that the proposed DTC-I scheme is able to minimize torque ripples to 30% of the load torque till 70% of the base speed. For speeds higher than 70% of the base speed, the controller varies the adjustable boundaries according to the DTC-II scheme mentioned.

Fig. 2.16 shows the response phase voltage, phase current, and total torque response of the DTC-II scheme for a constant load of 2 N-m. From the results, it is observed that even at the base speed, the DTC-II scheme is able to regulate the phase current, and the ripples in torque profile during commutation are kept below 50% of the load torque. Also, by switching to DTC-II, the efficiency of the system is decreased, as the active phase in the DTC-II scheme is not always excited in the maximum torque-producing region.

Fig. 2.17 shows the system efficiency and torque ripple comparison plots for a load of 3 N-m. The comparison plot illustrates that the proposed DTC-I and DTC-II schemes result in improved system efficiency and smoother torque output than the conventional CCC and DITC schemes.

The proposed DTC-I scheme, at the base speed, improves efficiency by 15% and 20% in comparison to CCC and DITC, respectively. And the proposed DTC-II scheme, at the base speed, improves efficiency by 10% and 15% in comparison to CCC and DITC, respectively.

The proposed DTC-I scheme, at base speed, improves the torque ripple by 45% and 25% in comparison to CCC and DITC, respectively. And the proposed DTC-II scheme, at the base speed improves the torque ripple by 55% and 35% in comparison to CCC and DITC, respectively.

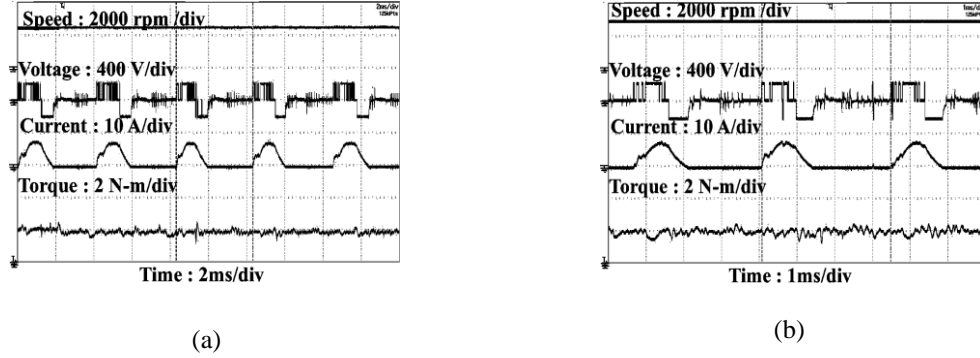


Fig. 2.16. Experimental waveforms of the proposed DTC-II scheme for a load torque of 2 N-m. (a) 2500 rpm. (b) 3000 rpm.

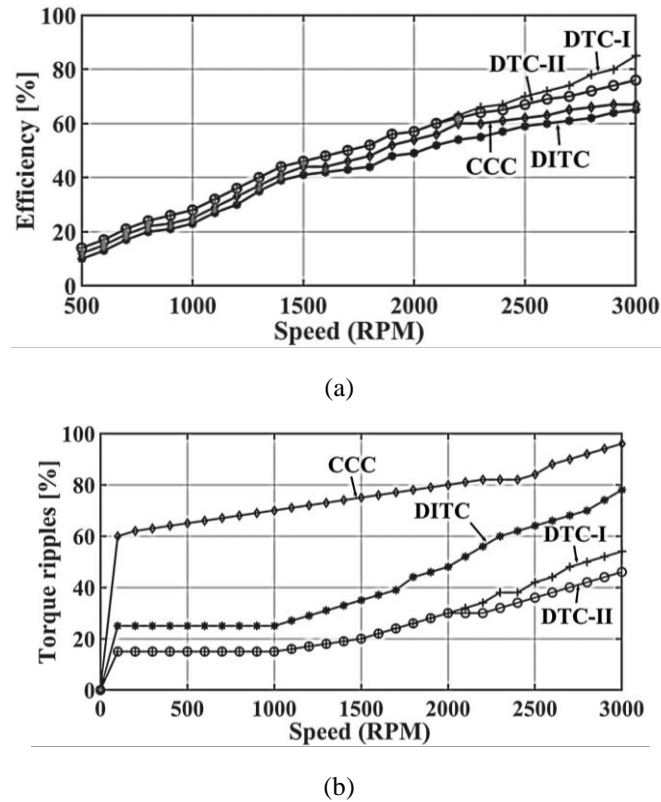


Fig. 2.17. Comparison of (a) efficiency and (b) torque ripple at 3 N-m for proposed DTC-I, DTC-II and conventional CCC and DITC.

2.5. CONCLUSION

Chapter-2 proposes a DTC scheme for 4-phase SRM, where simultaneously, two adjacent phases were excited to extend the smooth torque operating region to the base speed. In the proposed DTC scheme, the sector widths were varied in real-time, which is based on the maximum slope of the inductance profile. Two DTC schemes, i.e., DTC-I and DTC-II, were proposed. DTC-I operates till 70% of the base speed, and DTC-II operates above 70% of the base speed. The maximum torque ripple with DTC-I is 30% of the nominal torque till 70% of the base speed. Thereafter the controller switches to DTC-II, where the maximum torque ripple is 50% of the nominal torque at the base speed. The proposed DTC schemes resulted in improved system efficiency and smoother torque output than the conventional CCC and DITC scheme.

CHAPTER 3

AN INTEGRATED DRIVING/CHARGING 4-PHASE SWITCHED RELUCTANCE MOTOR DRIVE WITH INSTANTANEOUS ZERO CHARGING TORQUE PRODUCTION

The present chapter of the thesis investigates an integrated converter (IC) with driving and battery charging features for electric vehicles (EVs) drive-train employing a 4-phase SRM. The proposed IC allows flexible control over the DC link during drive mode, i.e., for motoring, it can boost the battery voltage, and during regenerative braking, it can maintain the battery charging profile. When the EV is standstill/idle, the proposed IC is reconfigured as an integrated single-phase battery charger incorporating two stages. The two-stage battery charger is comprehended by reconstructing the IC proposed into a bridgeless boost power factor correction (BB-PFC) circuit cascaded by a buck DC converter. The active inductors for the BB-PFC circuit are realized via the windings of the employed SRM.

Moreover, charging operation is performed at appropriate rotor positions, which results in a net-zero charging torque (ZCT) from the phases reconfigured as inductors. The proposed reconfiguration of inductors allows eight novel rotor positions for charging within an electrical cycle where ZCT is achieved. Thus, to reach the nearby rotor position for charging, the maximum displacement for the rotor is reduced to 3.75° mechanical, which any other IC does not achieve for the SRM drive. Also, the proposed IC does not require any additional relay or non-integrated circuit for its operation and can charge the battery with maximum supportive charging power up to the power rating of the traction SRM/converter. The efficacy of the proposed IC is shown by simulation and experimental verification.

3.1 PROPOSED IC DURING DRIVE MODE

Fig. 3.1. (a) shows the proposed IC configuration. The proposed IC employs a bidirectional DC-DC converter (BDDC) which forms the front end and is cascaded with the traction converter. The traction converter has an improved miller converter configuration that employs fewer switches than the conventional AHB converter.

Fig. 3.1. (b) shows the configuration of the front-end BDDC. The front-end BDDC during driving boosts the BES voltage to the required designed voltage of the SRM drive. Thus, the DC link voltage can vary from BES to the required voltage. And during battery charging mode, the front-end BDDC maintains the BES charging current and voltage profile. The following sub-sections discuss the control strategies for the proposed IC during the drive mode.

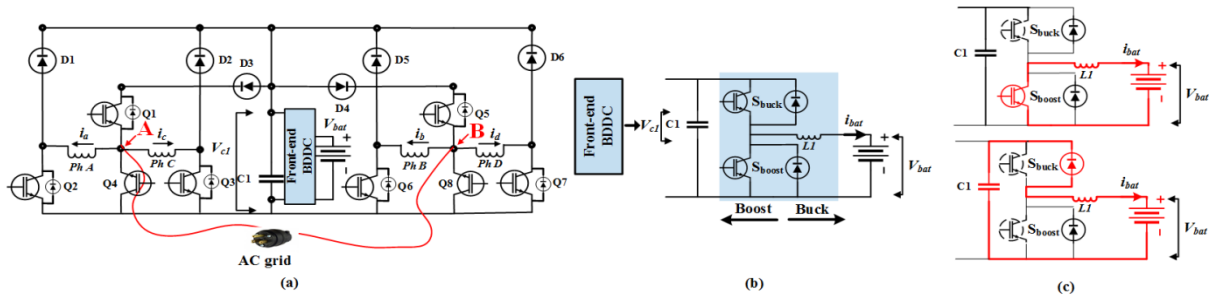


Fig. 3.1. Proposed IC configuration (a) Proposed IC, (b) front-end BDDC, and (c) front-end BDDC as boost converter.

3.1.1. BUCK/BOOST OPERATION FOR THE BDDC

The required DC-link voltage (V_{cl}) is derived by boosting the BES voltage (V_{bat}). The voltage across the DC-link is regulated to attain the rated voltage. For achieving boost operation, switching of S_{boost} switch in the front-end BDDC is regulated, and switch S_{buck} is kept in an OFF state. **Fig. 3.2** shows the closed voltage-controlled loop, and the corresponding switching states of the switch S_{boost} are shown in **Fig. 3.1. (c)**.

For charging the BES via the regeneration/braking power generated, switching pulses of S_{buck} switch in the front-end BDDC is regulated via a current controller. The reference battery current (i_{bat}^*) is decided based on the rate of braking and the BES charging capability. For detecting the braking operation, speed reference and the actual speed are compared, and whenever the comparison output is negative, the braking algorithm is performed, as shown in **Fig. 3. 2**.

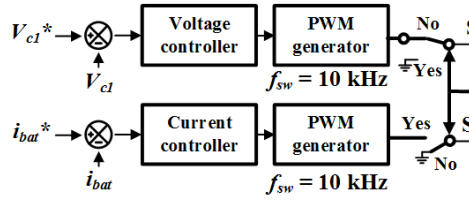


Fig. 3. 2. Front-end BDDC control for motoring and regenerative operation.

3.1.2. OPERATING MODES OF THE PROPOSED IC

As discussed above, the proposed IC boosts the BES voltage during drive mode and regulates the DC-link voltage to the set value by controlling the front-end BDDC. The improved miller converter connected in cascade controls the SRM drive. The improved miller converter employs switches, i.e., Q1 and Q5, for the quadrature-phase pairs. The two quadrature-phase pairs are phase-B, phase-D, and phase-A, phase-C. Employing common switches for quadrature-phases does not affect the driving performance of the SRM drive, as for 4-phase SRM, simultaneous conduction of quadrature-phases does not happen. Thus, the switch count is reduced with the improved miller converter compared to the conventional AHB converter.

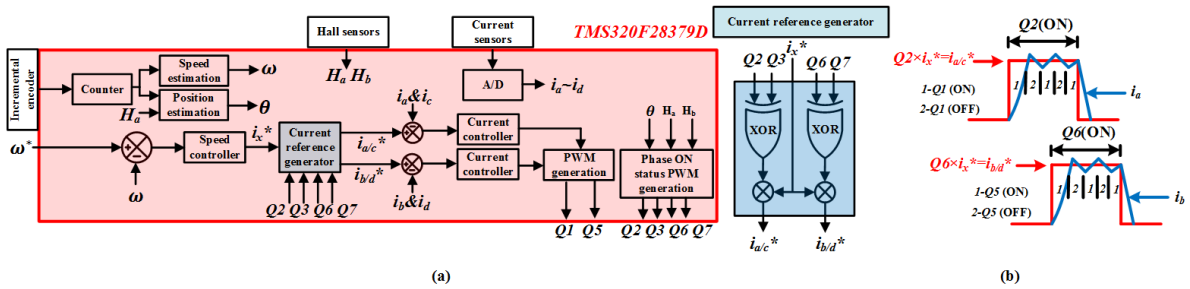


Fig. 3. 3. Adopted control strategy for the proposed IC during the driving mode.(a) control technique, and (b) switching states for reference and actual phase currents.

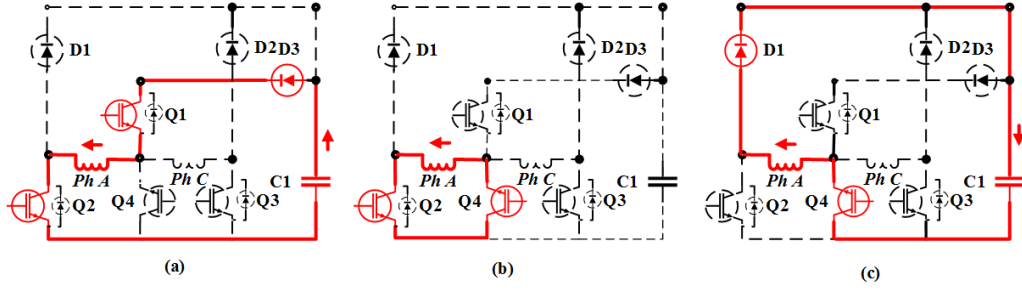


Fig 3. 4. Working states of the improved miller converter (a) energization, (b) free-wheeling, and (c) de-energization.

The adopted control strategy for the driving mode is shown in **Fig. 3.3. (a)**. The turn-on signal/s ($Q2/Q3/Q6/Q7$) for the active phase/s is/are generated by decoding the hall sensors (H_a , and H_b) outputs, as given in **Table. III. 1**. The generated phase turn-on signals are given to the current reference generator (CRG) block. The reference current (i_x^*) generated from the outer speed loop is also given as an input to the CRG block. The CRG block generates the current references $i_{a/c}^*$ and $i_{b/d}^*$ corresponding to the quadrature-phase pairs, i.e., $i_{a/c}^*$ for phase-C, phase-A, and $i_{b/d}^*$ for phase-D, phase-B. As shown in **Fig. 3.3. (a)**, the CRG block employs two XOR gates whose output is multiplied by i_x^* for generating the current references, $i_{a/c}^*$ and $i_{b/d}^*$. The input signals for the individual XOR gates are the generated turn-on signals of quadrature phases. The output of the XOR gates is multiplied by i_x^* , and the generated output of the CRG block for the different turn-on signals is given in **Table. III. 1**. Two current controllers are employed, whose output is given to the PWM generators, which generate the PWM signals for switches Q1 and Q5.

The generated reference and actual phase currents for phase-A (i_a) and phase-B (i_b) with the switching states are shown in **Fig. 3.3. (b)**. For phase-A, the active/turn-on period, switch Q2, is operated in an ON state. The error between the actual (i_a) and the generated reference ($i_{a/c}^*$) of phase-A is processed via the current controller. The current controller generates the switching signals for regulating switch Q1.

With switch Q1 turned ON, labeled a state-1 in **Fig. 3.3. (b)**, a positive voltage is applied to phase-A windings, and the corresponding mode of operation is shown in **Fig. 3.4. (a)**. With switch Q1, an OFF state, labeled a state-2, a zero voltage is applied across phase-A windings, and the corresponding mode of operation is shown in **Fig. 3.4. (b)**. At the end of the turn-on period for the phase-A switch, Q2 changes from an ON state to an OFF state, and the generated $i_{a/c}^*$ is also changed to zero. The zero $i_{a/c}^*$ current reference results in switching Q1 OFF, which further applies a negative voltage across phase-A, as shown in **Fig. 3.4. (c)**.

For phase B, the active/turn-on period, switch Q6, is operated in an ON state. The phase-B actual (i_b) and the generated reference ($i_{b/d}^*$) are compared for difference, and the corresponding error is processed via the current controller block. The current controller generates the switching signals for regulating switch Q5. To avoid repetition, phase-B operating states are not discussed as the improved miller converter holds symmetry and can be derived accordingly.

Thus, the improved miller converter reduces the switch count in comparison to the switch count of the conventional AHB converter without affecting the driving performance of the SRM drive.

TABLE III. I
PHASE TURN-ON SIGNAL GENERATION LOGIC

H_a and H_b	ON signal generated for	$i_{a/c}^*$	$i_{b/d}^*$
0 and 0	Q2	$Q2 \times i_x^*$	0
0 and 1	Q6	0	$Q6 \times i_x^*$
1 and 0	Q3	$Q3 \times i_x^*$	0
1 and 1	Q7	0	$Q7 \times i_x^*$

3.2. PROPOSED IC DURING BATTERY CHARGING MODE

When the EV is idle, the power electronics of the proposed IC and phase windings of the employed 4-phase SRM are not engaged. Thus, they are reutilized as a single-phase, two-stage battery charger. The two-stage battery charger is realized by the BB- PFC stage cascaded to a BDC. The inductors for the BB-PFC are realized via the phase-windings of the 4-phase SRM. The present section discusses the configuration and working/control of the integrated two-stage battery charger.

3.2.1. CONFIGURATION OF THE INTEGRATED TWO-STAGE CHARGER

The single-phase AC grid is connected between terminal-A and terminal-B, as seen in **Fig. 3.1**. With the integrated improved miller converter, quadrature-phase pairs are connected to a common terminal, i.e., phase-C, phase-A are connected to terminal-A, and phase-D, phase-B are connected to terminal-B, as shown in **Fig. 3.1. (a)**. Thus, quadrature phase windings are connected parallel, i.e., $L_c \parallel L_a$ and $L_d \parallel L_b$, when reconfigured as inductors in the BB-PFC charger.

For reconfiguring the phase/s as an inductor/s, the switch assigned to the particular phase is controlled via PWM signals. For phase-A to be reconfigured as an inductor, switch Q2 is applied with a PWM signal. Similarly, for phase-B, phase-C, and phase-D switches, Q6, Q3, and Q7 are controlled via PWM signals. The phase/s to be reconfigured as inductor/s depends on the rotor position, discussed later in the subsequent sections.

Thus, from the parallel connection of quadrature-phase, phase-A or/and phase-C can be reconfigured as inductor/s. Similarly, from another quadrature-phase pair, phase-B or/and phase-D can be reconfigured as inductor/s. Switches Q1, Q4, Q5, and Q8 are operated in the OFF state. The simplified reconfiguration of the realized two-stage battery charger is given in **Fig. 3.5**. For realizing the cascade BDC stage, the front-end BDDC is operated in buck mode by regulating the switching of the S_{buck} switch.

3.2.2. WORKING/CONTROL OF THE TWO-STAGE CHARGER

The control technique of the BB-PFC and the cascade BDC stage is shown in **Fig. 3.5**. The adopted control for BB-PFC employs a double-loop control scheme. The outer voltage control maintains the DC-link voltage (across C1) constant to a preset value greater than the input AC voltage peak. The inner current loop regulates the input AC current in-phase to the AC voltage, resulting in unity power factor operation. To achieve the stated objectives, switching of switches Q2, Q3, Q6, and Q7 are controlled.

For positive half-cycle, the input AC current enters through terminal-A and leaves through terminal-B, as shown in **Fig. 3.6. (a)** and **Fig. 3.6. (b)**. Here for discussion, it is assumed that all four phases of the employed SRM are reutilized as active inductors. During the turn-on interval of switches Q2 and Q3, the path of input AC current is through $L_a \parallel L_c$, switches Q2, Q3, diodes of switches Q6, Q7, and completes its path via $L_b \parallel L_d$,

resulting in charging of inductors via the input power, as shown in **Fig. 3.6. (a)**. Also, depending upon the inductance offered by parallel-connected quadrature-phases, the AC current (i_{ac}) is split equally or unequally among parallelly connected phases, i.e., the node equation at terminal-A is given as

$$i_{ac} = i_a + i_c. \quad (3.1)$$

For completing the current path, the input AC current also flows through $L_b \parallel L_d$. The parallel connection of phase-B and phase-D windings provides two paths for completing the input AC current path. The input AC current flows within the phase having a minimum inductance. The node equation at terminal-B is given as

$$i_b + i_d = -i_{ac}. \quad (3.2)$$

During the turn-off interval of switches Q2 and Q3, the input AC current path is through $L_a \parallel L_c$, diodes D1, D2, capacitor C1, diodes of switches Q6, Q7 and completes its path via $L_b \parallel L_d$, resulting in applying a higher voltage across C1, as shown in Fig. 3.6. (b). For the negative half-cycle, as shown in Fig. 3.6. (c) and Fig. 3.6. (d), the input AC current enters through terminal-B and leaves through terminal-A. The working of the BB-PFC for the negative half-cycle is similar to that of the positive half-cycle. Hence not discussed to avoid repetition. The tuning of inner and outer loop PI controller gains is discussed in appendix section.

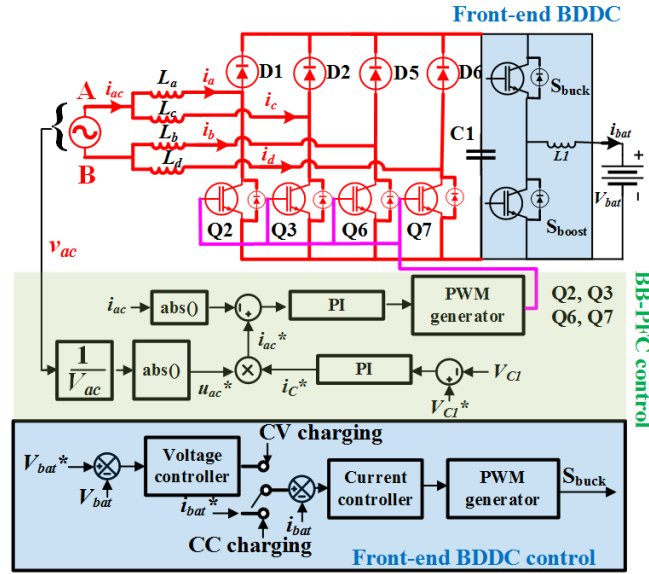
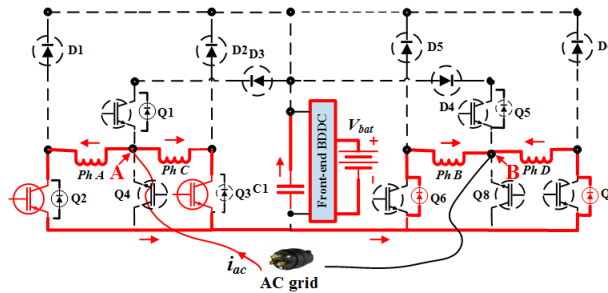


Fig. 3. 5. Simplified and complete diagram of battery charging scheme with the employed control strategy.



(a)

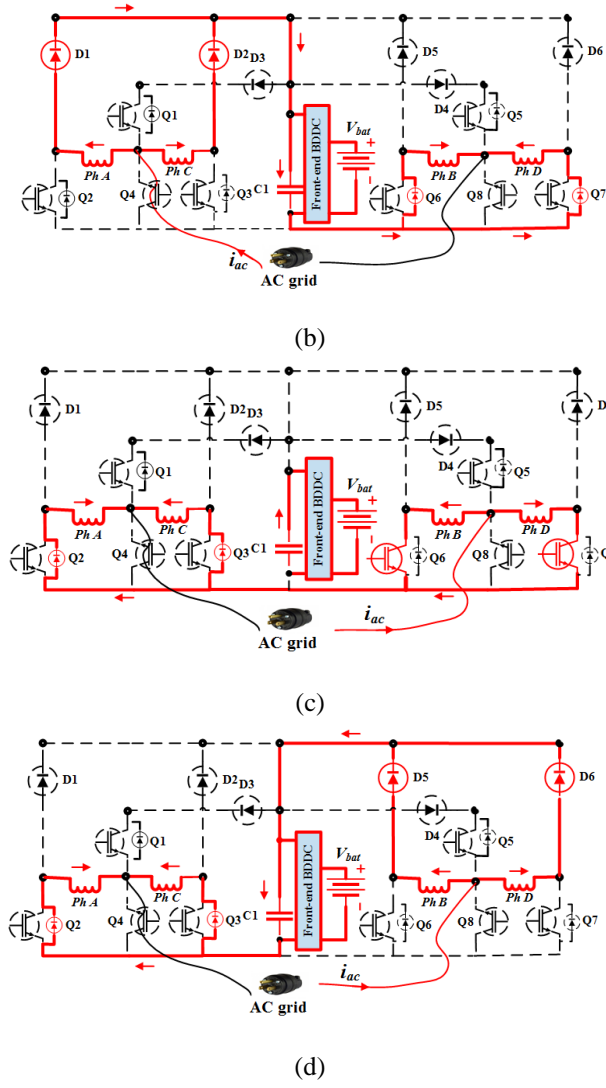


Fig. 3. 6. Operating modes of the BB-PFC during battery charging mode. (a) Positive half-cycle, switch (Q2, Q3) ON state. (b) Positive half-cycle, switch (Q2, Q3) OFF state. (c) Negative half-cycle, switch (Q6, Q7) ON state, and (d) Negative half-cycle, switch (Q6, Q7) OFF state.

3.3. NOVEL CHARGING ROTOR POSITIONS FOR ZCT AND SIMULATION RESULTS

As discussed in the previous section, the 4-phase SRM winding/s are reutilized as working inductors in the BB-PFC charger. However, for SRM, charging torque is generated due to the current flowing within the phase windings. The approximated partial differential equation for the instantaneous phase torque ($T_e(\theta, i)$) for SRM is given by

$$T_e(\theta, i) = i^2 \frac{\partial L(\theta, i)}{\partial \theta}, \quad (3.3)$$

where, $L(\theta, i)$ is the phase inductance as a function of rotor position and phase current. Thus, the present section discusses the proposed novel charging rotor positions at which ZCT is achieved. The designed 4-phase SRM prototype in ANSYS and the corresponding actual inductance profile are shown in **Fig. 3.7. (a)** and **Fig. 3.7. (b)**. The zero-rotor position of the 4-phase SRM is fixed at a position where phase-A is completely unaligned, and phase-C is wholly aligned, as marked and seen in **Fig. 3.7. (a)**. According to the inductance profile, the proposed

charging rotor positions are grouped into two categories, i.e., rotor positions A1, A2, A3, A4, and rotor positions B1, B2, B3, B4, as shown in **Fig. 3.7. (b)**.

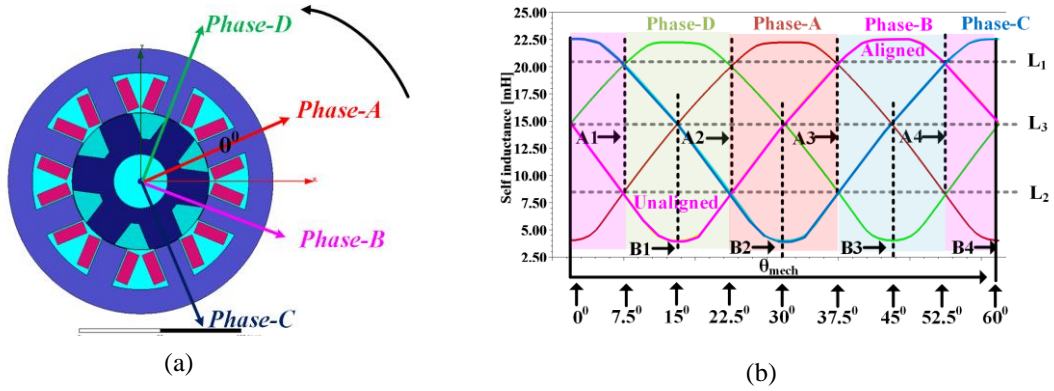


Fig. 3.7. (a) Designed prototype 4-phase SRM. (b) Actual inductance profile of the 4-phase SRM.

3.3.1. ROTOR POSITIONS A1, A2, A3, A4

At rotor positions A1, A2, A3, and A4, all the 4-phase windings are reconfigured as inductors. At rotor position A1, the input AC current is divided between $L_a \parallel L_c$ while entering terminal-A and $L_b \parallel L_d$ while leaving terminal-B, as inferred from **Fig. 3.6**. Phase-A and phase-B windings at rotor position A1 offer L_2 inductance and are near to their unaligned inductance position. Similarly, phase-C and phase-D windings offer L_1 inductance and are near their aligned inductance position, as inferred from **Fig. 3.7. (b)**. Thus, the total inductance offered by the parallel combination of $L_a \parallel L_c$ and $L_b \parallel L_d$ equals $L_1 \parallel L_2$.

Within the parallelly connected quadrature-phase windings, the phase winding/s with lower inductance will allow the flow of majority input AC current through them. At rotor position A1, adjacent phase-A and phase-B windings near their unaligned inductance offering lesser inductance (i.e., L_2) will allow the flow of majority input AC current through them. Similarly, at rotor positions A2, A3, and A4, the phase windings near their unaligned inductance will offer lower inductance, thus leading to majority of the input current flowing through them. **Table. III. II** gives detailed information on the phases near unaligned and aligned inductance positions.

At rotor positions A1, A2, A3, and A4, all the four phases are reconfigured as inductors, resulting in current through them. At rotor position A1, the torque generated due to current in phase-A and phase-C (at terminal A) is given by

$$T_a = \frac{1}{2} K_a i_a^2 \quad \text{and} \quad T_c = \frac{1}{2} K_c (i_{ac} - i_a)^2, \quad K_a > 0, K_c < 0 \quad (3.4)$$

where i_a and i_c are the currents through phase-A and phase-C windings. And K_a and K_c denote the slope of the inductance profile with respect to the rotor position for phase-A and phase-C windings, respectively. At rotor position A1, K_a is positive, resulting in positive torque, and K_c is negative, resulting in negative torque production. Similarly, the resultant torque from charging current in phase-B and phase-D (at terminal B) is expressed as

$$T_b = \frac{1}{2} K_b i_b^2 \quad \text{and} \quad T_d = \frac{1}{2} K_d (i_{ac} - i_b)^2, \quad K_d > 0, K_b < 0 \quad (3.5)$$

where i_b and i_d are the currents through phase-B and phase-D windings. And K_b and K_d denote the slope of the inductance profile with respect to the rotor position for phase-B and phase-D windings, respectively. At rotor

position A1, K_d is positive, resulting in positive torque, and K_b is negative, resulting in negative torque production. Also, the inductance offered by phase-A, phase-B, and phase-C, phase-D is equal, resulting in equal magnitude of current through them, i.e., $i_a = i_b$, and $i_c = i_d$. Thus from (3.4) and (3.5), the net charging torque (T_{net}) generated because of current in all the 4-phases is zero, mathematically given as

$$T_a = -T_b, \text{ and } -T_c = T_d, \text{ and} \quad (3.6)$$

$$T_{net} = T_a + T_b + T_c + T_d = 0 \quad (3.7)$$

TABLE III. II
CHARGING POSITIONS A1, A2, A3, A4 CHARACTERISTICS

Position	Phase near aligned inductance	Phase near unaligned inductance	Net inductance	Phase torque	Torque magnitude
A1-7.5°	Phase-C	Phase-A	$(L_1 L_2)$	$+T_a - T_c$	$ T_a = T_b $
	Phase-D	Phase-B	$(L_1 L_2)$	$-T_b + T_d$	$ T_c = T_d $
A2-22.5°	Phase-A	Phase-C	$(L_1 L_2)$	$-T_c + T_a$	$ T_c = T_b $
	Phase-D	Phase-B	$(L_1 L_2)$	$+T_b - T_d$	$ T_a = T_d $
A3-37.5°	Phase-A	Phase-C	$(L_1 L_2)$	$+T_c - T_a$	$ T_c = T_d $
	Phase-B	Phase-D	$(L_1 L_2)$	$-T_d + T_b$	$ T_a = T_b $
A4-52.5°	Phase-C	Phase-A	$(L_1 L_2)$	$-T_a + T_c$	$ T_a = T_d $
	Phase-B	Phase-D	$(L_1 L_2)$	$+T_d - T_b$	$ T_c = T_b $

3.3.2. ROTOR POSITIONS B1, B2, B3, B4

At rotor positions B1, B2, B3, and B4, selected 3-phase windings are reconfigured as inductors. At rotor position B1, phase-A, phase-B, and phase-C windings are reconfigured as inductors. The input AC current while entering terminal-A is equally divided between phase-A and phase-C. The current is equally divided because both the phases offer equal inductance (L_3), as seen in **Fig. 3.7. (b)**. And while leaving at terminal-B, the AC current only flows through the phase-B winding as the offered inductance by phase-D is higher (>10) than that of phase-B. **Table. III. III** gives the information of the selected phases to be reconfigured as inductors for rotor positions B2, B3, and B4.

At rotor position B1, the torque due to current within phase-A and phase-C windings (at terminal A) is given by

$$T_a = \frac{1}{2} K_a i_a^2 \quad \text{and} \quad T_c = \frac{1}{2} K_c (i_{ac} - i_a)^2, \quad K_a = -K_c \quad 3. (8). (a)$$

$$T_b = \frac{1}{2} K_b i_b^2, \quad K_b = 0 \quad 3. (8). (b)$$

where K_a and K_c are equal and opposite, as seen from **Fig. 3. 7. (b)**. Thus, the net torque from current in phase-A and phase-C is zero. Similarly, while at terminal-B, the total AC current in phase-B winding results in zero torque as K_b is zero.

$$T_a = -T_c, \text{ and } T_b = 0 \quad (3.9)$$

$$T_{net} = T_a + T_b + T_c = 0. \quad (3.10)$$

Thus, the net torque due to current in three-phase windings is zero. **Table. III. III** gives the information of the phases reconfigured as inductors and the corresponding instantaneous torque produced by them for rotor positions B2, B3, and B4.

To perform battery charging at any one of the discussed novel charging rotor positions, the rotor must be displaced from the initial EV parking position. For this, firstly, the clutch is disengaged, and then the nearest rotor position is identified. For knowing the nearest rotor position, the displacement of rotor from initial parking position to the charging rotor position is measured. And the charging position offering minimum rotor displacement is selected, and the rotor is displaced to that charging rotor position by controlling the excitation of appropriate phases.

TABLE III. III
PHASE CHARACTERISTICS AT CHARGING POSITIONS B1, B2, B3, B4.

Position	Phase reconfigure as inductors		Phase torque	Torque magnitude
B1-15°	Phase-A	Phase-C	$+T_a - T_c$	$ T_a = T_c $
	Phase-B		T_b	$ T_b = 0$
B2-30°	Phase-C		T_c	$ T_c = 0$
	Phase-B	Phase-D	$+T_b - T_d$	$ T_b = T_d $
B3-45°	Phase-A	Phase-C	$-T_a + T_c$	$ T_a = T_c $
	Phase-D		T_d	$ T_d = 0$
B4-0°/60°	Phase-A		T_a	$ T_a = 0$
	Phase-B	Phase-D	$-T_b + T_d$	$ T_b = T_d $

3. 3. 3. SIMULATION RESULTS

For the simulation results shown in **Fig. 3.8**, the input AC voltage (v_{ac}) is 230V RMS, and the BES nominal voltage, charging current are selected to be 72 V and 15 A, respectively. The BES charging power is then calculated as $72V \times 15A = 1080$ W.

Fig. 3.8. (a) shows the simulated result during battery charging at rotor position A1. As discussed at rotor position A1, all the 4-phases are reconfigured as active inductors. And adjacent phase-A and phase-B near the unaligned inductance position offering lesser inductance allows majority flows of the input AC current. Also, from (4.1) and (4.2) for the positive half-cycle, $i_{ac} = i_a + i_c$, and $i_b + i_d = -i_{ac}$. From **Fig. 3.8. (a)**, it is observed that the total/net torque (T_{net}) due to the currents within the phase winding/s is zero. This is because equal and opposite torque is produced by phase-A, phase-B, and phase-C, phase-D winding which ultimately results in ZCT production as derived using (3.6) and (3.7).

Fig. 3.8. (b) shows the simulated result during battery charging at rotor position B1. As discussed at rotor position B1, selected 3-phase windings are reconfigured as inductors. And at terminal-A, phase-A and phase-C windings offer equal inductances resulting in an equal division of input AC current among them.

At terminal-B, only phase-B is reconfigured as an inductor resulting in complete AC current through it, as evident from **Fig. 3.8. (b)**. Also, the net torque due to current in 3-phases is zero resulting in ZCT production as derived using (4.9) and (4.10). Thus, the proposed charging rotor positions, grouped into two categories, i.e., rotor positions A1, A2, A3, A4, and rotor positions B1, B2, B3, B4, result in ZCT production.

Fig. 3.9. (a) shows the magnetic field analyzed using ANSYS/Maxwell software for the operating conditions mentioned when charging is done at rotor position A1 for the instant X1 marked in **Fig. 3.9. (a)**. The finite element analysis (FEA) shows that most of the field lines for phase-A, phase-B, and phase-C, phase-D

cancel one another within the rotor structure as the field direction is opposite. Thus, no field lines for a particular phase complete its path via the rotor structure; instead, the field lines for phase-A, phase-B, and phase-C, phase-D form a closed loop, resulting in non-continuous torque leading to a stationary rotor.

Fig. 3.9. (b) shows the magnetic field when charging at rotor position B1 for the instant X2 marked in **Fig. 3.9. (b)**. The figure shows that phase-A and phase-C field lines cancel one another and form a closed loop, holding the rotor stationary. **Fig. 3.9** also shows the magnetic field density (B-tesla) developed during battery charging mode. The developed magnetic field magnitude is far lesser than the rated B of the core used (M43_29G). Thus, the magnetic field developed during charging does not saturate the core and thus is not that considerable.

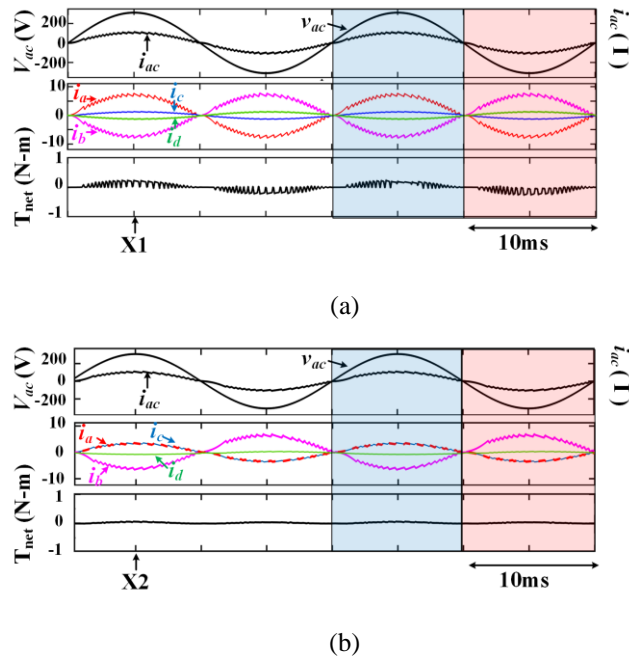
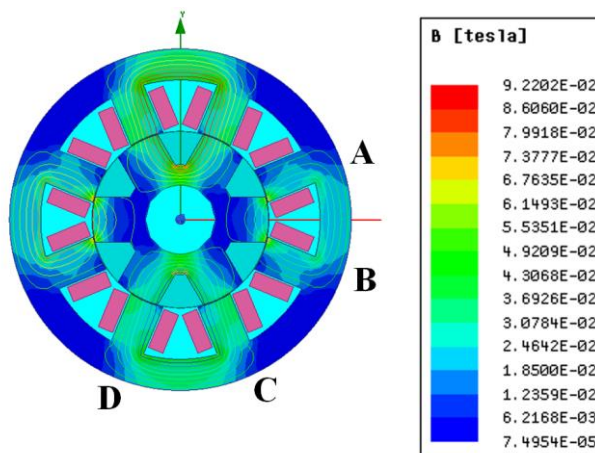
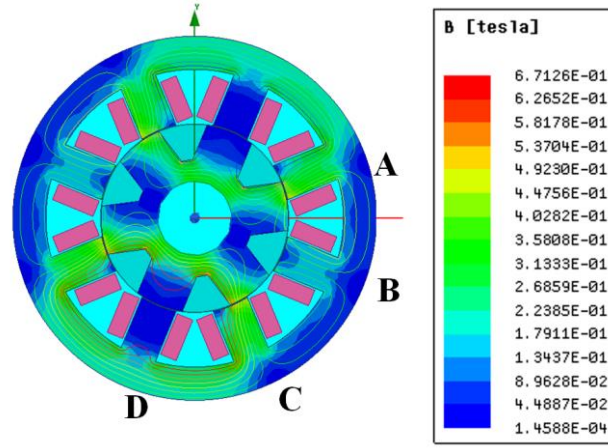


Fig. 3.8. (a) Simulation results when charging at rotor position (a) A1, and (b) rotor position B1.



(a) FEA of magnetic field at rotor position-A1, at the marked instant X1.



(b) FEA of magnetic field at rotor position-B1, at the marked instant X2

Fig. 3. 9. (a) FEA of magnetic field when battery charging at rotor position (a) A1 and (b) rotor position B1.

3.4. EXPERIMENTAL VERIFICATION

The IC proposed is validated using two IGW50N60TP discrete IGBT switches and seven SKM75GB12T4 IGBT switches. The 4-phase 8/6, 1.1 kW SRM designed parameters are given in appendix. The discussed control techniques are implemented on a digital signal processor (DSP) TMS320-F28379D, with a sampling frequency fixed at 50 kHz (20 μ s). The experimental test bench is shown in **Fig. 3.10**.

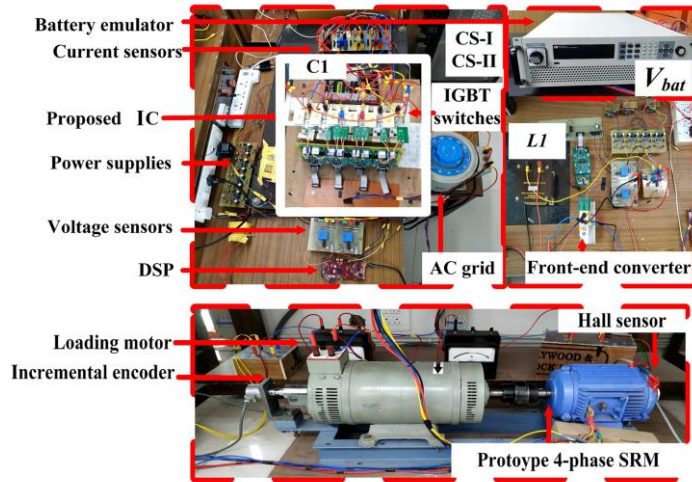


Fig. 3. 10. Experimental test bench.

The torque during driving and battery charging is calculated online via employing a torque v/s current, and position look-up table derived using the FEA analysis. The look-up table derived from the FEA analysis is provided in the appendix.

The battery functionality is emulated via the ITECH-6012B power supply. The nominal battery voltage (V_{bat}) is realized via connecting six 12V/150 Ah cells in series. Thus, for maintaining the battery charging rate as C/10, the battery charging current is regulated at 15 A. The proposed IC is connected to an AC source voltage of 230 V RMS (standard grid voltage) for charging the battery.

3.4.1. DRIVING MODE

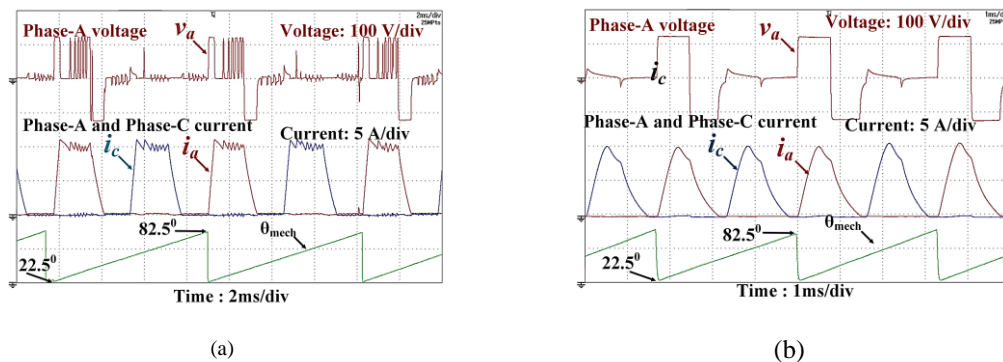
During motoring, the battery voltage ($V_{bat} = 72$ V) is boosted to the rated phase voltage ($V_{cl} = 120$ V) for SRM by controlling the switching signals of S_{boost} switch. The front-end BDDC converter adopted control strategy is shown in **Fig. 3.2**. The switching frequency of the PWM generator is set to 10 kHz. The inductance (L_l) in the front-end BDDC is set to 3 mH. The chosen value of the DC-link capacitance, i.e., C_1 , is 1200 μ F/450V.

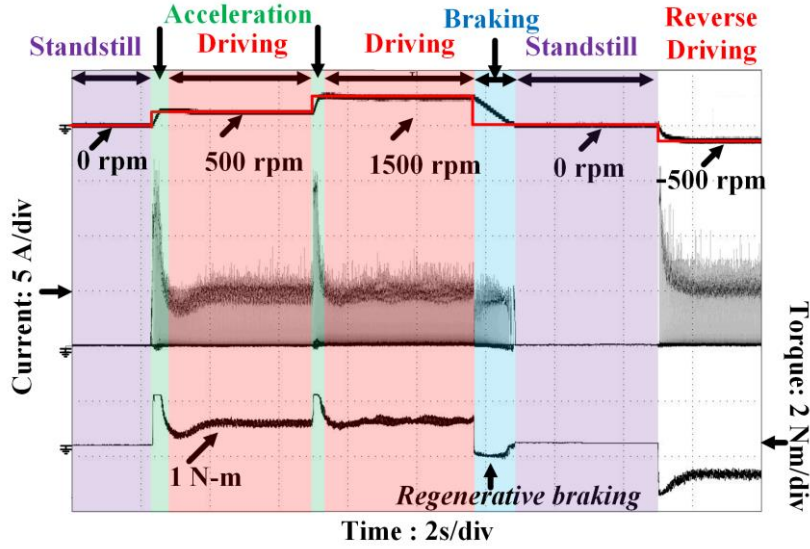
For the driving mode, the proposed IC is reconfigured to an improved miller converter, and constant current control (CCC) is employed for controlling as shown in **Fig. 3.3**. The improved miller converter is switched at 10 kHz.

Fig. 3.11. (a) and **Fig. 3.11. (b)** shows the phase-A voltage, phase-A, and phase-C currents along with the rotor position when operating at 1500 rpm and 3100 rpm (maximum operating speed). The results show that for 4-phase SRM, simultaneous conduction of quadrature phases is not possible. Thus, employing common switches for quadrature phase pairs with the improved miller converter does not affect the driving performance of the SRM drive.

The dynamical response of the 4-phase SRM with the proposed IC is shown in **Fig. 3. 11. (c)**. For demonstrating the start-up response, the speed reference from a standstill is changed to 500 rpm. An increase in the speed reference increases the phase currents to provide maximum acceleration. Thus, to limit the phase current value during acceleration, the saturation limit for current is set to 15 A. Then to demonstrate speed change at constant load, the reference speed is changed to 1500 rpm.

Further, the speed is decreased to zero rpm to demonstrate the de-acceleration and the regeneration/braking capabilities. From the figure, it can be seen that during regenerative braking, the torque is negative. Thus, the power is delivered back to the source. The reference current during regenerative/braking operation is set to 5A. During regeneration operation, switch S_{buck} is applied with PWM signals. The regenerative power is used to charge the battery in constant current (CC) mode. For demonstrating the reverse motoring operation, the speed reference is then set to -500 rpm. Thus, all EV possible working driving modes are shown in **Fig. 3. 11. (c)**.





(c)

Fig. 3. 11. Experimental results for phase-A voltage and current with quadrature phase-C current and rotor position during drive mode of operation (a) 1500 rpm, (b) 3100 rpm, and (c) Dynamic performance with speed, current, and experimental torque waveforms.

3.4. 2. BATTERY CHARGING MODE

The proposed IC for charging mode, is reutilized as a two-stage battery charger realized using a BB-PFC circuit cascaded to a BDC stage. The inductors for the BB-PFC are realized via the phase windings of 4-phase SRM. Thus, for achieving a net ZCT, the rotor is moved to any one of the suitable nearest rotor positions from the eight rotor positions discussed in section IV.

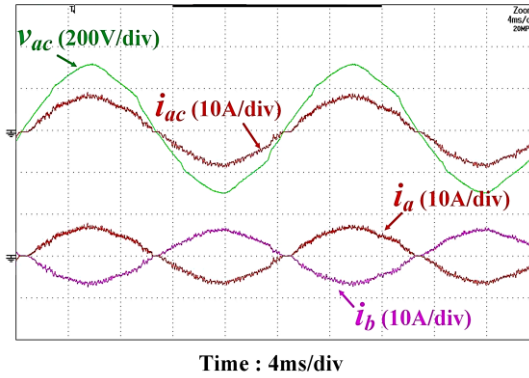
The output voltage of the BB-PFC (i.e., V_{cl}) is controlled at 400 V by applying a closed-loop strategy which is discussed in section III. B and shown in **Fig. 3.5**. The cascaded front-end BDDC maintains the charging profile of the BES. The front-end BDDC adopted control strategy is shown in **Fig. 3.5**.

Fig. 3.12 and **Fig. 3.13** show the experimental results when for performing battery charging rotor position A1 and rotor position B1 are selected. Mechanical fixture/ braking is not applied to rotor for the experimental results. The battery charging current (i_{bat}^*) is maintained at 15A (C/10 charging rate).

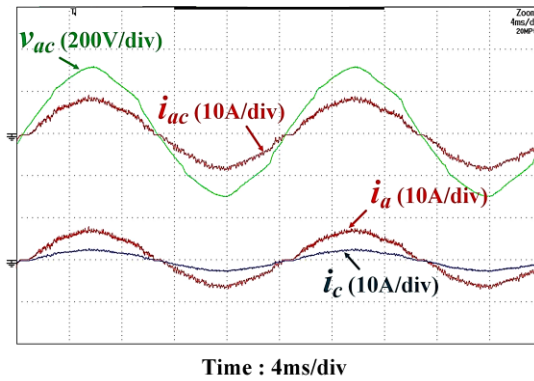
Fig. 3.12. (a) and **Fig. 3.12. (b)** gives the experimental input AC current and voltage, and the current within phase-B, and quadrature phase pair, i.e., phase-C and phase-A, for charging at rotor position A1. It can be inferred from the figures that for the positive half-cycle, the input AC current while entering terminal A is unequally divided between phase-C and phase-A, i.e., $i_{ac} = i_a + i_c$. And while leaving at terminal B, phase-B and phase-D currents add up to the total input AC current, which is mathematically given by (3.1) and (3.2). The unequal division of input AC current among quadrature phases is because of the lesser inductance of phase-B and phase-A windings that flow most of the input AC current. **Fig. 3.12. (c)** shows all the 4-phase currents in one window, and the input AC current is derived by adding phase-C and A currents using the MATH operation and is mathematically given by (3.1).

Fig. 3.13. (a) and **Fig. 3.13. (b)** gives the experimentally input AC current and voltage, and the current within phase-B and quadrature phase-C and phase-A, when charging at rotor position B1. It can be inferred from the figures that for the positive half-cycle, the input AC current while entering terminal A is equally divided between phase-C and phase-A windings. This is because both the phase windings offer equal inductance. And while leaving at terminal B, complete input AC current flows through phase-B. **Fig. 3.13. (c)** shows the 3-phase windings currents, along with the input AC current derived by adding phase-A and phase-C currents, and mathematically given by

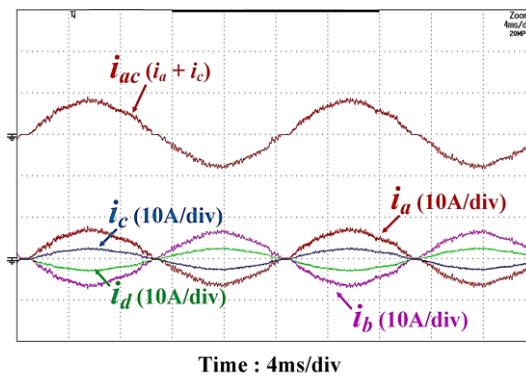
$$i_{ac} = i_a + i_c, \text{ also } i_{ac} = -i_b \quad (3.11)$$



(a)

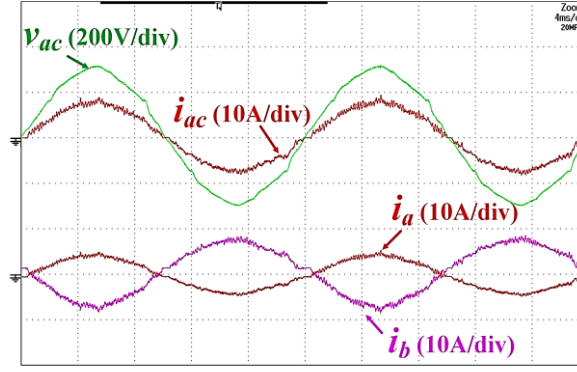


(b)

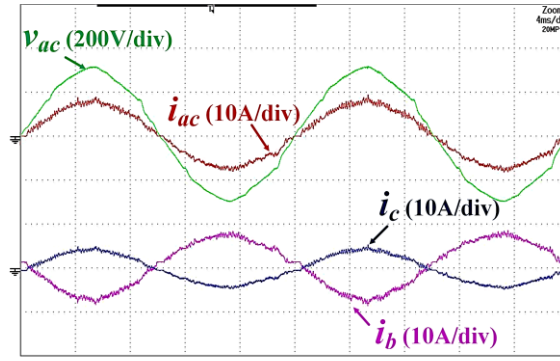


(c)

Fig. 3.12. Experimental results when charging at rotor position A1. (a) Input AC voltage, current with adjacent phase-A and phase-B currents (b) Input AC voltage, current with quadrature phase-A and phase-C currents. (c) All four phase currents with input AC current using MATH operation.

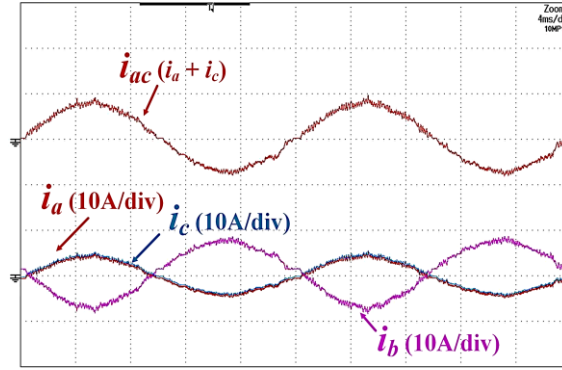


(a)



Time : 4ms/div

(b)_



Time : 4ms/div

(c)

Fig. 3. 13. Experimental results when charging at rotor position B1. (a) Input AC voltage, current with adjacent phase-A and phase-B currents (b) Input AC voltage, current with adjacent phase-B and phase-C currents. (c) Three phase currents with input AC current using MATH operation.

3.4.3. RESULTANT NET CHARGING TORQUE DURING CHARGING

The current in the phase winding/s when charging at rotor positions A1 and B1 results in ZCT, as discussed in previous subsections. **Fig. 3.14. (a)** and **Fig. 3.14 (b)** show the stationary rotor position (θ_{mech}) during charging at rotor positions A1 and B1, respectively. Also, the total charging torque i.e., (T_{net}) which is the total torque from all the phases is shown. Mathematically T_{net} is given as

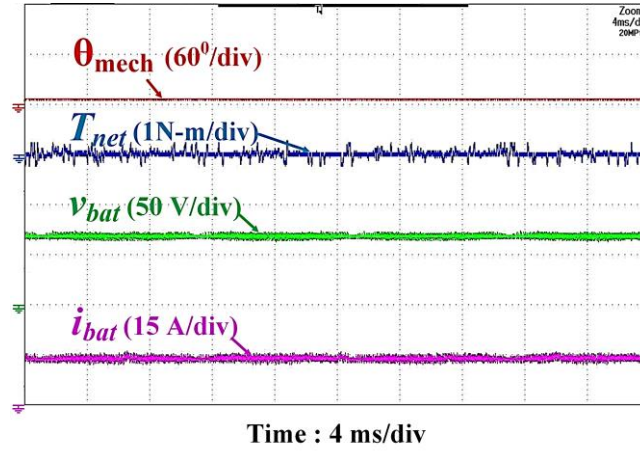
$$T_{net} = T_a + T_b + T_c + T_d. \quad (3.12)$$

Fig. 3.14, also shows the BES voltage and current when charged in CC mode with a user defined current reference of 15 A. The BES charging power (i.e., P_{bat}) and the drawn input power (i.e., P_{ac}) can be calculated using

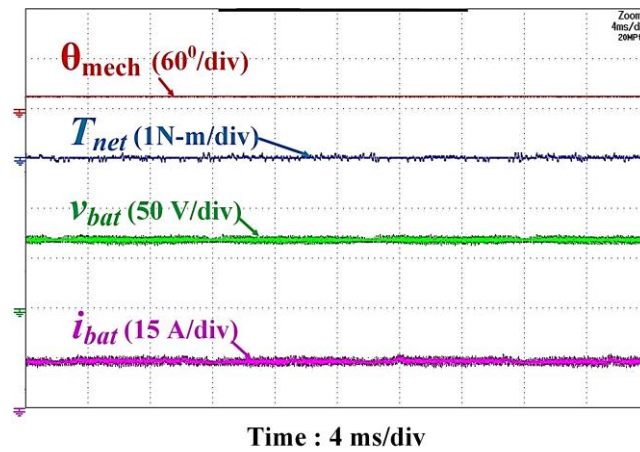
$$P_{bat} = V_{bat} * i_{bat} = 72 * 15 = 1080 \text{ W}, \text{ and} \quad (3.13)$$

$$P_{ac} = V_{ac} * i_{ac} * \cos \theta = 230 * i_{ac} * \cos \theta = \frac{P_{bat}}{\eta} \quad (3.14)$$

where η denotes the efficiency of the two-stage battery charger. The input power drawn from the single-phase AC supply is measured using FLUKE 43B power quality analyzer. The input AC power required to for charging the battery at 1080 W is approximately 1290 W. Thus, the efficiency of the two-stage battery charger from (3.14) comes out as 83.7 %. **Fig. 3.15**. shows the FFT analysis of the input AC current waveform. The calculated total harmonic distortion (THD) is 6.49%.



(a)



(b)

Fig. 3. 14. Rotor position (θ_{mech}) with total charging torque generated with battery voltage and current when charging battery at (a) rotor position A1, and (b) rotor position B1.

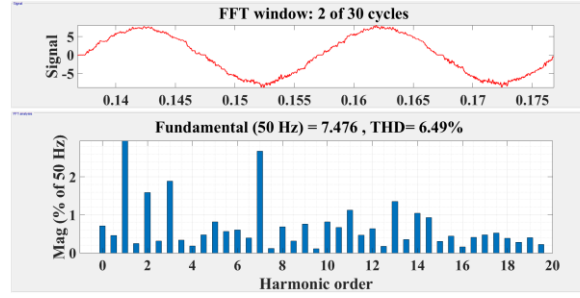


Fig. 3. 15. Experimental input AC current FFT analysis.

3.5. CONCLUSION

The chapter proposes a fully IC with charging and driving capabilities for EV application incorporating 4-phase SRM. The proposed IC configuration is an improved miller converter with a cascaded front-end BDDC converter. The front-end BDDC during the drive mode of operation boosts the BES voltage, and during regenerative braking, it maintains the charging profile of the BES. During charging operation, the proposed IC is reconfigured as a single-phase two-stage battery charger. The inductors for the front-end BDDC are realized via the phase winding/s of the traction SRM. However, for SRM, the current in the phases leads to torque production.

With the proposed IC, eight novel rotor positions are proposed at which ZCT is achieved. Thus, for reaching the nearest rotor position for charging, the maximum displacement is reduced to mechanical, which any other IC does not achieve for SRM drive. Also, the magnetic field density at the proposed charging rotor is not that considerable, which verified using FEA analysis. The ZCT at the proposed rotor positions is verified by observing the total charging torque at the specified rotor positions via simulation and experimental studies.

CHAPTER 4

FULLY INTEGRATED MULTI-LEVEL POWER CONVERTER FOR SRM DRIVE WITH CHARGING CAPABILITIES (G2V) FOR ELECTRIC VEHICLE APPLICATION

The present chapter investigates a fully integrated multi-level power converter topology (IML-PCT) with integrated battery charging capability for SRM drive. The proposed IML-PCT applies higher energization and de-energization voltage during the driving mode, leading to an enhanced constant torque region for SRM drive. For applying higher voltage levels, a capacitor is connected in series with the DC-link. The DC-link is derived via a battery energy storage system (BESS) powered bidirectional DC-DC converter (BDDC) serving as a front-end.

During battery charging mode, the proposed IML-PCT exhibits the characteristics of an on-board charger (OBC) capable of charging BESS directly via a standard AC outlet. The OBC functionality is realized by reconfiguring the proposed IML-PCT into an interleaved bridgeless boost power factor correction circuit (IBB-PFCC). The DC-DC/charging inductors of the IBB-PFCC are realized by reutilizing/reconfiguring all the windings of the 4-phase SRM. Also, with the proposed IBB-PFCC configuration, the charging current in the windings leads to an average zero torque production. Thus, the rotor is kept stationary during battery charging mode without any external braking mechanism. To maintain the BESS charging voltage and current profile, the IBB-PFCC is operated in cascade with a front-end BDDC.

4.1. OPERATING MODES AND CONTROL TECHNIQUES OF THE PROPOSED IML-PCT

The proposed IML-PCT for a 4-phase SRM drive is shown in **Fig. 4.1**. **Fig. 4.1. (b)** shows the BESS powered front-end BDDC providing bidirectional power flow. The operating modes and the adopted control strategies of the IML-PCT during driving and battery charging modes are discussed in detail in the sub-sections following.

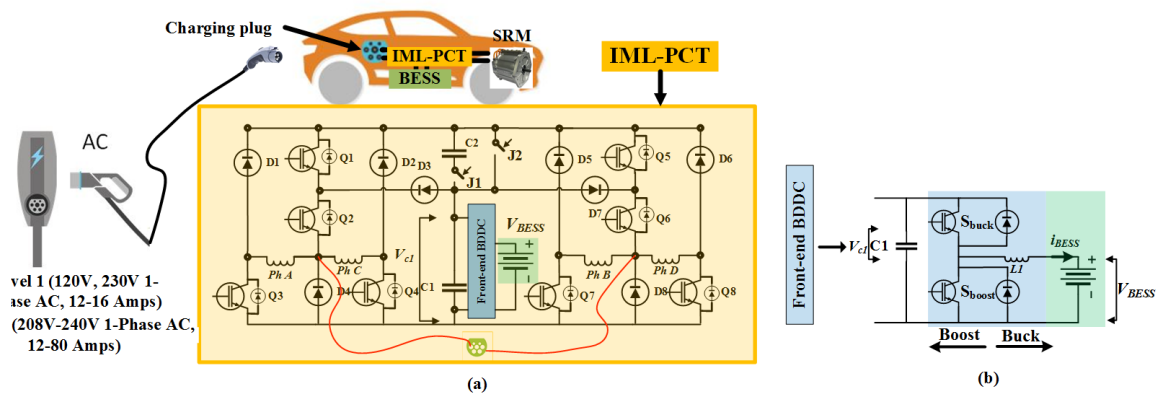


Fig. 4. 1. Proposed IML-PCT with driving and charging capabilities for 4-phase SRM drive-based EV application.

4.1.1. DRIVING MODES

(1) Front-end BDDC as buck/ boost converter: The front-end BDDC performs two functions during motoring mode. First, it boosts the BESS voltage to the DC-link voltage (V_{cl}), which is kept equal to the rated voltage for the SRM drive.

And second, it maintains the DC-link voltage constant by regulating the S_{boost} switching pulses via a closed voltage control loop, as shown in **Fig. 4.2**.

During regeneration/braking mode, the front-end BDDC charge the BESS in CC mode via the regenerative power generated. The CC charging of BESS is achieved by applying S_{buck} with the switching pulses generated via a closed current control loop, as shown in **Fig. 4.2**.

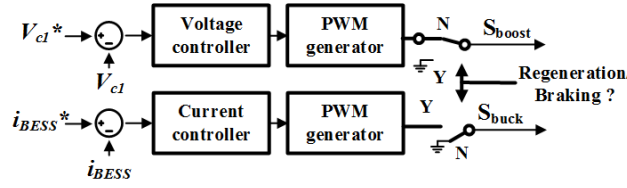


Fig. 4. 2. Control strategy for the front-end BDDC during the driving mode.

(2) Operating modes of the proposed IML-PCT during motoring: During driving mode, relay J1 is closed, and J2 is opened, resulting in capacitor C2 connecting in series with the DC-link capacitor C1. The resulting configuration of the IML-PCT during driving mode is shown in **Fig. 4.3. (a)**.

For driving SRM in motoring mode, the positive slope of the inductance profile is utilized to energize the respective active phase/s. For analyzing the operating modes of IML-PCT during motoring, phase-A conduction is considered. The possible four operating modes of the IML-PCT are discussed below.

Mode- I- [Fig. 4.3. (b)]: During this mode, switches Q1, Q2 and Q3 are turned ON. And phase-A winding is applied with $(V_{cl} + V_{c2})$ voltage. By applying mode-I, the phase current energization is accelerated. Moreover, the required angular width/rotor position for incoming phase current energization reduces in comparison to the angular width required when the incoming phase is energized with V_{cl} voltage (i.e., the rated phase voltage) applied, as shown in **Fig. 4.4**.

Thus, by applying higher phase voltage, the incoming phase energization in lower $\frac{d\phi}{d\theta}$ region, marked as region A1 in **Fig. 4.4**, can be avoided. It results in an improved RMS value of the phase current, which leads to improved torque output and the torque-per-ampere ratio. Also, by applying higher phase voltage, the base speed for SRM drive increases which is mathematically given by

$$\frac{d\phi}{d\theta} = \frac{V_{ph}}{\omega_{max}}, \quad (4.1)$$

where V_{ph} is the applied phase-voltage, ϕ is the phase flux-linkage and ω_{max} denotes the maximum operating speed. Thus from (4.1), it is observed that for a fixed $\frac{d\phi}{d\theta}$, increasing V_{ph} increases the maximum operating speed range.

Mode- II- [Fig. 4.3. (c)]: During this mode, switch Q1 is turned OFF, and Q2, Q3 are maintained in an ON state. And phase-A winding is applied with V_{c1} voltage.

Mode- III- [Fig. 4.3. (d)]: During this mode, switches Q1, Q2 are turned OFF, and Q3 is maintained in an ON state. And phase-A winding is applied with zero voltage across it.

Mode- IV- [Fig. 4.3. (e)]: During this mode, switches Q1, Q2 and Q3 are turned OFF, resulting in phase-A winding applied with $-(V_{c1} + V_{c2})$ voltage. Thus, by applying mode-IV, the phase current de-energization is accelerated. And the required angular width/rotor position for complete de-energization of the outgoing phase current reduces compared to the angular width required when the outgoing phase is de-energized with $-V_{c1}$ voltage applied, as shown in **Fig. 4.4**.

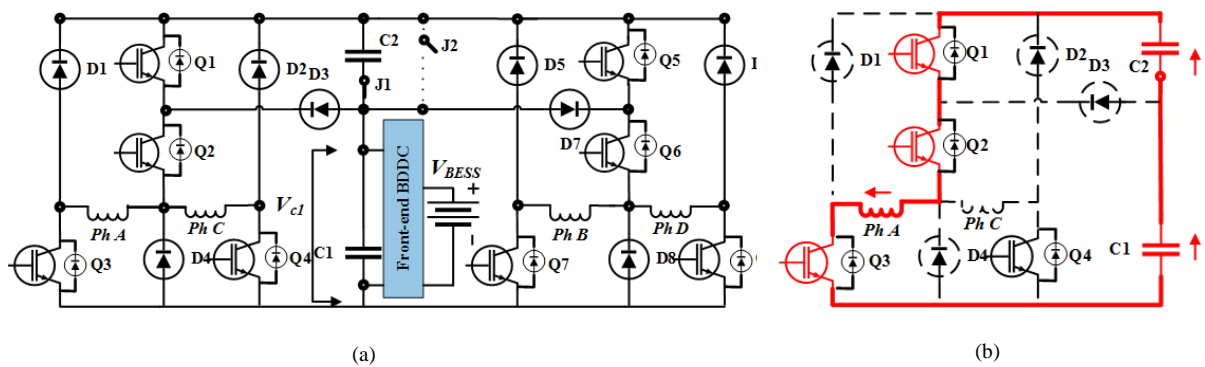
Thus, at higher operating speeds, outgoing phase tail current can be suppressed within the positive slope of inductance slope, marked as region A2 in **Fig. 4.4**, restricting the negative torque production. A detailed discussion on the advantages of applying higher phase de-energization is available in existing literature.

(4.2) gives the mathematical relation of the rate-of-change of phase current with respect to rotor position, which is given as

$$\frac{di}{d\theta} = \frac{V_{ph} - \omega \frac{d\phi(\theta, i)}{d\theta}}{\omega \frac{d\phi(\theta, i)}{di}}, \quad (4.2)$$

where, $\omega \frac{d\phi(\theta, i)}{d\theta}$ is the back electromotive force (BEMF). Thus from (2), it is seen by applying $V_{c1} + V_{c2}$ as V_{ph} , the effect of BEMF (which is speed-dependent) is compensated, resulting in an increased positive slope of $\frac{di}{d\theta}$ i.e., faster energization. And by applying $-(V_{c1} + V_{c2})$ as V_{ph} , the negative slope of $\frac{di}{d\theta}$ increases, i.e., faster de-energization.

Thus, by applying mode-I, phase current energization is accelerated, leading to improved torque output. And by applying mode-IV, phase current de-energization is accelerated, which restricts the negative torque production. To conclude, applying higher phase voltages during energization and de-energization results in extending the constant torque region for SRM drive.



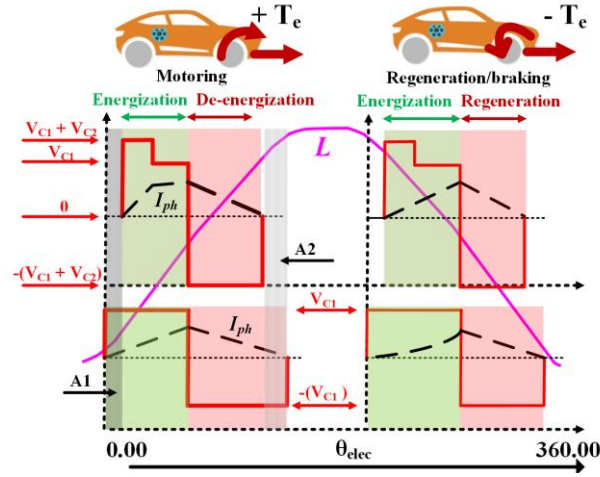


Fig. 4. 4. Comparison of voltage levels of the IML-PCT with 3-level AHB/miller converter.

(3) Operating modes of the proposed IML-PCT during regeneration/braking: SRM is a singly excited system. Thus, for driving SRM in regenerative/braking mode, respective active phase/s need to be excited for its regeneration. During regenerative braking, the inductance profile negative slope is utilized to energize the active phase/s, which is shown in **Fig. 4.4**.

During regeneration, the proposed IML-PCT applies mode-I for faster energization of phase current. In (5.2) it is mathematically shown that the regenerative /braking power output increases by faster energization of the incoming phase to its reference value. Thus, improving the regenerative efficiency.

Further, due to negative BEMF during regeneration mode, from (1), it is observed that applying a zero voltage (i.e., mode-III) results in a positive slope of $\frac{di}{d\theta}$. And or having the negative slope of $\frac{di}{d\theta}$, the phase winding/s is/are applied with a negative phase voltage (i.e., mode-IV). Thus, for regulating the phase current at its reference value, phase winding/s is/are applied with mode-III and mode-IV.

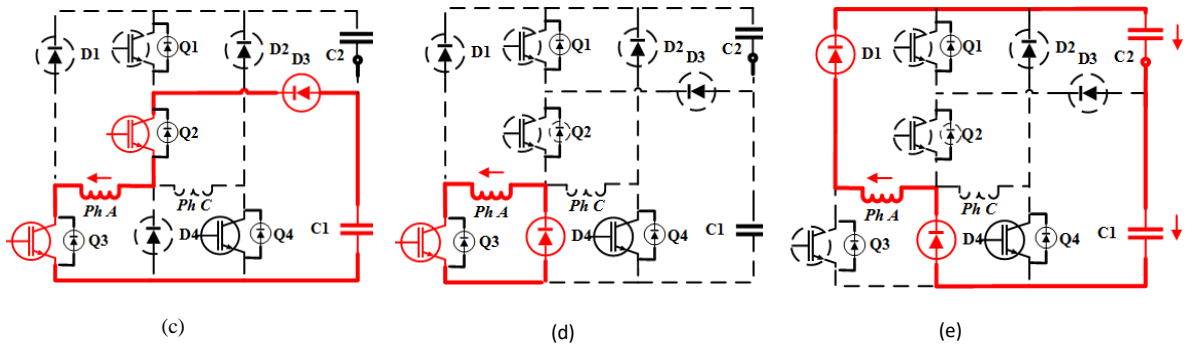


Fig. 4. 3. (a) IML-PCT configuration during driving mode. Operating modes of the IML-PCT (b) Mode-I, (b) Mode-II, (d) Mode-III, and (e) Mode-IV.

4.1.2 Battery charging mode

For battery charging mode, relay J1 is opened, and J2 is closed, resulting in capacitor C2 disconnecting from the IML-PCT. Also, switches Q1, Q2, Q5 and Q6 are maintained in an OFF state. The resulting configuration of the IML-PCT during battery charging mode is shown in **Fig. 4.5**.

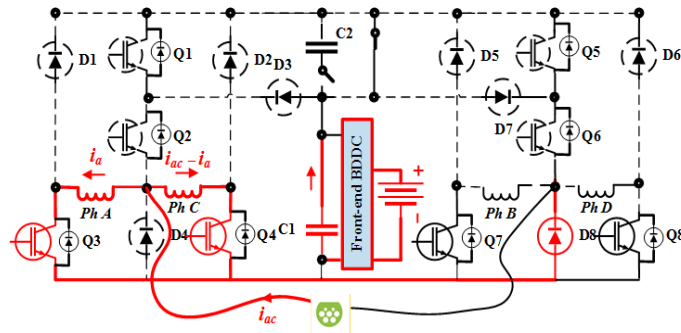
The configuration/working, selection of charging rotor positions, and analysis for torque produced at selected charging rotor position (i.e., charging torque) when the proposed IML-PCT is reconfigured as IBB-PFCC based OBC is discussed in the sub-sections following.

(1) Configuration/working of the IBB-PFCC: For IBB-PFCC configuration, the DC-DC/charging inductors are realized by reconfiguring the phase windings of SRM.

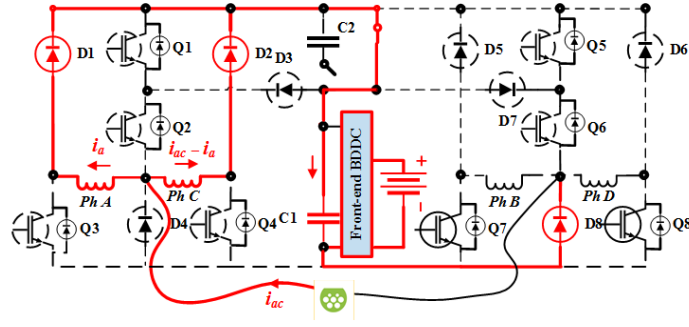
For realizing the charging inductor during the positive half-cycle, quadrature phase-A and phase-C windings are connected in parallel. Furthermore, as shown in **Fig. 4.5. (a)** and **Fig. 4.5. (b)**, switches Q3, Q4 and diodes D1, D2 with charging inductor ($L_a \parallel L_c$) forms an IBB converter through the diode D8. Similar to the IBB converter working, when switches Q3 and Q4 are turned ON, the charging inductor ($L_a \parallel L_c$) is charged via the input AC current flowing through it, as shown in **Fig. 4.5. (a)**. And when switches Q3 and Q4 are turned OFF, the developed voltage across the charging inductor ($L_a \parallel L_c$), in addition to the AC voltage, is applied across capacitor C1, as shown in **Fig. 4.5. (b)**. Thus, resulting in a boost voltage across capacitor C1.

Similarly, for realizing the charging inductor during the negative half-cycle, quadrature phase-B and phase-D windings are connected in parallel. Furthermore, as shown in **Fig. 4.5. (c)** and **Fig. 4.5. (d)**, switches Q7, Q8 and diodes D5, D6 with charging inductor ($L_b \parallel L_d$) forms an IBB converter through the diode D4. The working of the IBB converter during the negative half-cycle is shown in **Fig. 4.5. (c)** and **Fig. 4.5. (d)**. The resulting simplified circuit diagram of the IBB-PFCC is shown in **Fig. 4.6**. **Fig. 4.6** also shows the adopted control strategy for switching Q3, Q4 and Q7, Q8 in respective half-cycles.

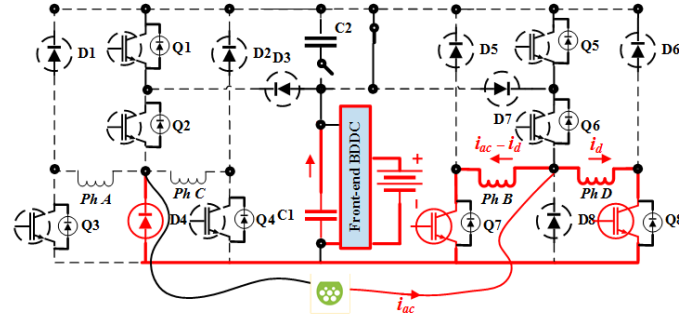
The front-end BDCC control strategy is also shown in **Fig. 4.6**. For battery charging mode, S_{boost} is always maintained in an OFF state. And S_{buck} depending on the BESS voltage/state-of-charge, is applied via a closed-loop current or voltage control loop for achieving CC/CV mode of charging.



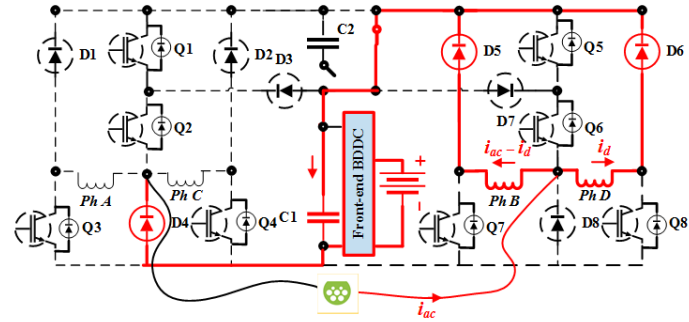
(a) Positive cycle of AC (switches Q3 and Q4 are in an ON state, resulting in inductor $L_a \parallel L_c$ charging).



(b) Positive cycle of AC (switches Q3 and Q4 are in an OFF state, resulting in inductor $L_a \parallel L_c$ discharging).



(c) Negative cycle of AC (switches Q7 and Q8 are in an ON state, resulting in inductor $L_b \parallel L_d$ charging).



(d) Negative cycle of AC (switches Q7 and Q8 are in an OFF state, resulting in inductor $L_b \parallel L_d$ discharging).

Fig. 4. 5. IBB-PFCC operating modes during battery charging.

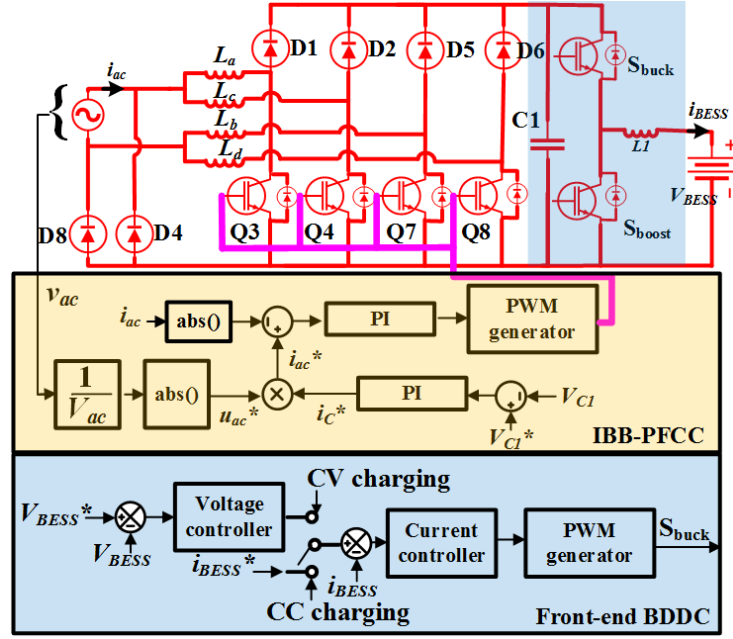


Fig. 4. 6. Resulting IBB-PFCC with employed control strategy.

(2) Charging rotor position selection: For having symmetrical IBB-PFCC, i.e., equal inductance from the realized charging inductors for the respective half-cycles, rotor positions were $(L_a \parallel L_c) = (L_b \parallel L_d)$ are considered for charging.

For 4-phase SRM, due to symmetry in inductance profile, $(L_a \parallel L_c) = (L_b \parallel L_d)$ can be obtained at four different rotor positions, which are marked as rotor position A, B, C and D in **Fig. 4.7**. At any of the charging rotor positions discussed, the net inductance is equal to $(L_1 \parallel L_2)$. Thus, resulting in a symmetrical IBB-PFCC.

However, during the positive half-cycle, quadrature phases, i.e., phase-A and phase-C, connected parallelly $(L_a \parallel L_c)$, do not offer equal inductance to the flow of input AC current. The phase winding, near the aligned inductance position having L_1 inductance, offers higher inductance to the flow of input AC current than the phase winding near the unaligned inductance position having L_2 inductance. This, during the positive half-cycle, results in unequal distribution of the input AC current flowing through phase-A and phase-C windings.

Similarly, during the negative half-cycle, quadrature phases, i.e., phase-B and phase-D, connected parallelly $(L_b \parallel L_d)$, do not offer equal inductance to the flow of input AC current. This, during the negative half-cycle, results in unequal distribution of the input AC current flowing through phase-B and phase-D windings.

Thus, from the above discussion, it is concluded that the phase windings near unaligned inductance position, offering L_2 inductance in the respective half-cycles, will flow most of the input AC current through them. And since the phases near to unaligned inductance, which in the ideal case are not sensitive to magnetic saturation, will not saturation when high current flows through them. Thus, the IBB-PFCC configuration with the above-discussed charging rotor positions is not sensitive to magnetic saturation. **Table. IV. I** summarize the phase windings characteristics at different charging rotor positions discussed.

The above discussion assumes that current flowing in the phase windings near unaligned inductance position corresponding to AC level-1 and AC level-2 charging will be less than the rated current of the employed traction

SRM. In extreme high input AC current wherein the currents in the phase windings near unaligned position reach the rated phase current of the employed traction SRM, saturation is inevitable due to the highly non-linear nature of SRM.

For performing BESS charging with symmetrical IBB-PCCC configuration, the rotor is displaced to one of the nearest charging rotor positions. For locating the nearest charging rotor position, one electrical cycle is divided into four equal sectors, as shown in **Fig. 4. 7**. Depending on the EV parking position's sector, the nearest charging rotor position is decided. **Table. IV. II** gives the information for the nearest charging rotor position for the EV parking position in sectors I, II, III or IV. **Table. IV. II** also gives the information of the phases that need to be excited for reaching the nearest charging rotor position.

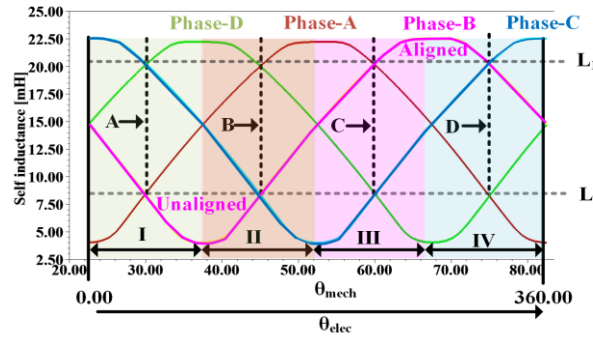


Fig. 4. 7. Charging rotor positions during the battery charging mode.

TABLE. IV. I
PHASE CHARACTERISTICS AT DIFFERENT CHARGING ROTOR POSITIONS

AC cycle	Charging rotor position	Phase near unaligned inductance	Phase near aligned inductance	Net inductance offered	Net torque produced
+	A	Phase-A	Phase-C	$L_1 L_2$	$+T_a - T_c$
-	A	Phase-B	Phase-D	$L_1 L_2$	$-T_b + T_d$
+	B	Phase-C	Phase-A	$L_1 L_2$	$-T_c + T_a$
-	B	Phase-B	Phase-D	$L_1 L_2$	$+T_b - T_d$
+	C	Phase-C	Phase-A	$L_1 L_2$	$+T_c - T_a$
-	C	Phase-D	Phase-B	$L_1 L_2$	$-T_d + T_b$
+	D	Phase-A	Phase-C	$L_1 L_2$	$-T_a + T_c$
-	D	Phase-D	Phase-B	$L_1 L_2$	$+T_d - T_b$

TABLE. IV. II
NEAREST CHARGING ROTOR POSITION FROM THE EV PARKING POSITION

EV parking position sector	Nearest charging rotor position	Phases to be excited	Maximum rotor displacement
I	A	C and D	7.5^0 mech
II	B	D and A	7.5^0 mech
III	C	A and B	7.5^0 mech
IV	D	B and C	7.5^0 mech

(3) Charging torque produced: The current flowing in the phase windings of 4-phase SRM when reconfigured as charging inductors results in torque production. Thus, fundamental analysis for the torque produced during the BESS charging process is carried out in this sub-section.

As discussed in the earlier sub-section, the magnetic saturation at rotor positions A, B, C, and D can be neglected. Thus, the absolute value of the slope of the inductance at unaligned inductance position is fixed and denoted by K_2 , and at aligned inductance position, it is denoted by K_1 . For charging torque analysis, the rotor is assumed to be at charging rotor position B.

In the positive half-cycle of the AC supply, the net torque generated from the quadrature phases (phase-A and phase-C) can be expressed as:

$$T_a = \frac{1}{2} K_1 i_a^2 \quad \text{and} \quad T_c = -\frac{1}{2} K_2 (i_{ac} - i_a)^2, \quad (4.3)$$

where, i_a is the current flowing through phase-A winding and $(i_{ac} - i_a)$, is the current through the phase-C winding, as shown in **Fig. 4.5. (a)** and **Fig. 4.5. (b)**. Similarly, in the negative half-cycle of the AC supply, the net torque generated from quadrature phases (phase-B and phase-D) can be expressed as

$$T_d = -\frac{1}{2} K_1 i_d^2 \quad \text{and} \quad T_b = \frac{1}{2} K_2 (i_{ac} - i_d)^2, \quad (4.4)$$

where, i_d is the current flowing through phase-D winding and $(i_{ac} - i_d)$, is the current through the phase-B winding, as shown in **Fig. 4.5. (c)** and **Fig. 4.5. (d)**. At rotor position B, because of the similar inductance (i.e., L_1) offered by phase-A and phase-D, equal current flow through them, i.e., $i_a = i_d$. Thus, in an AC cycle, the torque produced due to current in phase windings is given as:

$$T_a + T_b + T_c + T_d = 0. \quad (4.5)$$

Similarly, charging rotor positions A, C and D, results in a zero average torque production in an AC cycle. It is already established that an average zero-charging torque in an AC cycle does not produce any starting torque during charging. Thus, eliminating the requirement of external braking. **Table. IV.I** give the net torque produced by the quadrature phases in each half-cycle for all charging rotor positions discussed.

4.2. EXPERIMENTAL VERIFICATION

For validating the proposed IML-PCT characteristics, experiments are performed on 4-phase 8/6 SRM. The experimental platform is shown in **Fig. 4.8**. For realizing the battery functionality ITECH-6012B battery emulator feature is used. The BESS voltage (V_{BESS}) is realized via serial connection of six 12V/120 Ah cells. Detailed analyses during driving and battery charging modes are as follows.

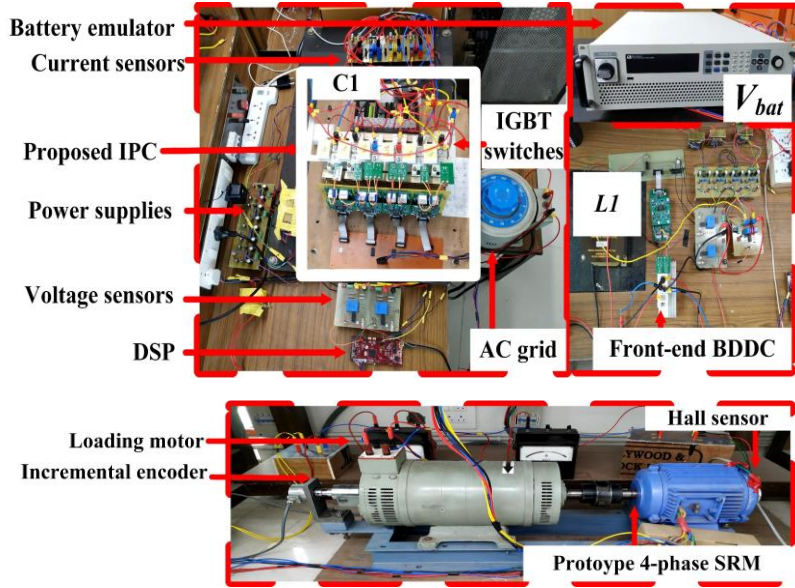


Fig. 4. 8. Experimental setup.

(1) **Driving mode:** During driving mode, the front-end BDDC depending upon motoring or regenerative mode, applies PWM signals to either S_{buck} or S_{boost} via a closed control loop, as shown in **Fig. 4.2**. The BESS powered front-end BDDC boost the BESS voltage (72V) to the rated phase voltage for SRM (120V) during motoring mode.

For driving the 4-phase SRM in motoring mode, constant current control (CCC) is adopted. The voltage across capacitor C2 is maintained constant at 50V by controlling mode-I duration via a closed control loop.

The proposed IML-PCT performance is compared with conventional AHB/miller for highlighting its advantages. **Fig. 4. 9. (a)** shows the steady-state performance of the proposed IML-PCT when operated as a conventional AHB/miller converter at 1500 rpm, along with the time required for phase current energization and de-energization.

Fig. 4. 9. (b) shows the steady-state performance of the proposed IML-PCT at 1500 rpm. During phase energization, mode-I is applied, resulting in $V_{c1} + V_{c2}$ (170 V) applied across the phase winding. Thus, applying mode-I leads to faster energization of the phase current in comparison to the phase current energization when only V_{c1} applied, as shown in **Fig. 4. 9. (a)** and **Fig. 4. 9. (b)**. Similarly, during phase de-energization, applying mode-IV (i.e., -170 V) results in faster phase current de-energization in comparison to the phase current de-energization when only $-V_{c1}$ applied, as shown in **Fig. 4. 9. (a)** and **Fig. 4. 9. (b)**. Thus, the phase current energization and de-energization are accelerated with the proposed IML-PCT. **Fig. 4. 9. (c)** shows the maximum operating speed for the SRM drive when operated with the proposed IML-PCT.

The experimental torque/speed characteristics of the SRM drive when driven with conventional AHB/miller converter and with proposed IML-PCT are shown and compared in **Fig. 4. 10**. The effect of applying higher energization and de-energization voltage extends the constant torque region, with a corresponding improvement in the constant power region for SRM drive.

(2) **Battery charging mode:** During battery charging mode, the proposed IML-PCT is utilized as IBB-PFCC based OBC. For demonstrating the battery charging mode operation, the rotor is displaced to rotor position B.

The IBB-PFCC based OBC boosts the AC grid voltage (230 V, 50 Hz) to the set V_{cl} reference voltage (i.e. 400 V). The IBB-PFCC with the control strategy, as shown in Fig. 6, maintains the V_{cl} voltage constant to the set reference. The BESS charging current (i.e., i_{BESS}) is kept at 12 A (C/10 charging).

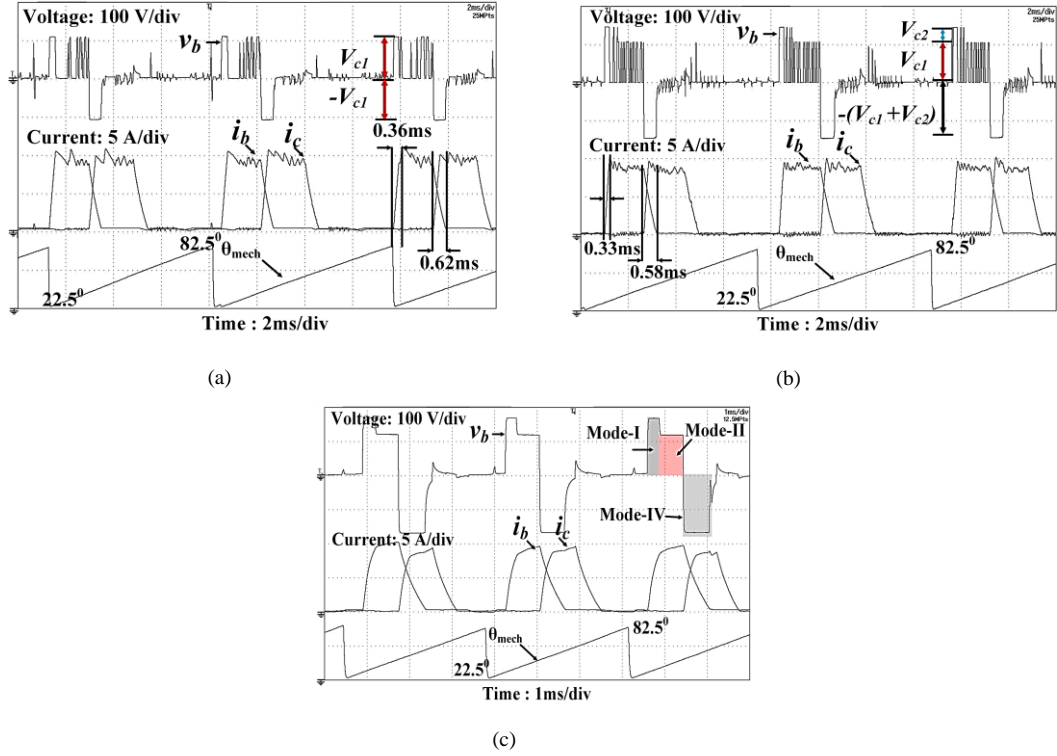


Fig. 4. 9. Proposed IML-PCT experimental results during the motoring mode (a) 1500 rpm, $T_L = 1.9$ N-m (when operated as conventional AHB/miller converter) (b) 1500 rpm, $T_L = 1.9$ N-m and (c) 3150 rpm [maximum operational speed].

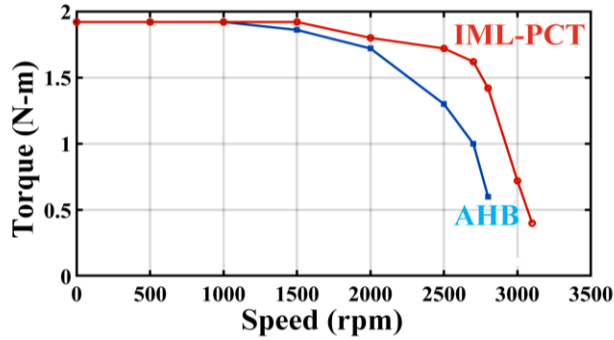


Fig. 4. 10. Torque-speed curve with AHB/miller converter and proposed IML-PCT.

During the positive half-cycle, parallelly connected quadrature windings, i.e., $L_a \parallel L_c$, conduct simultaneously to form an IBB configuration. **Fig. 4. 11. (a)** and **Fig. 4. 11. (b)** shows the AC grid voltage, current along with phase currents waveform. Also, charging at rotor position B implies unequal inductance offered via parallelly connected quadrature windings, resulting in an unequal division of input current among them, as observed from **Fig. 4. 11. (b)**.

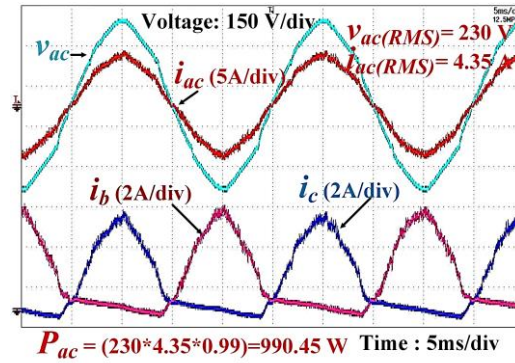
Phase-C winding, near to unaligned inductance position with inductance L_2 lesser than the inductance (L_1) of phase-A winding allows most of the input AC current to flow through them, which can be observed from **Fig. 4. 11. (b)**. Similarly, during the negative half-cycle, most of the input AC current flows through phase-B winding as it is near its unaligned inductance position, as shown in **Fig. 4. 11. (a)**.

The standstill rotor position during battery charging mode is shown in **Fig. 4. 11. (c)**. Thus, it can be seen that the rotor is stationary without any external braking. The generated transient torque due to charging current in phase windings is also shown in **Fig. 4. 11. (c)**. An average zero-charging torque in an AC cycle does not produce any starting torque, which results in a standstill rotor. The transient torque leads to vibrations in the motor setup. But in the actual case, the shaft vibrations are nullified by the cart weight when the proposed IML-PCT is incorporated in the EV application. **Fig. 4. 11. (c)** also shows the BESS voltage and the charging current magnitude when charged in CC mode for a reference current of 12 A. The BESS charging power (i.e., P_{BESS}) for the result shown in **Fig. 4. 11. (c)** is 816 W. And the corresponding drawn AC power (i.e., P_{ac}) is 990.45 W.

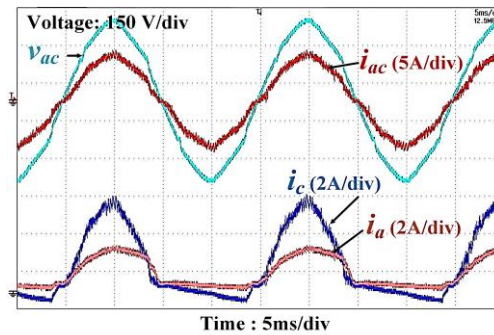
For evaluating the performance of the IBB-PFCC, the input power factor (IPF) and total harmonic distortion (THD) of the experimentally obtained input AC current is analyzed. The calculated THD is 6.32%. The measured IPF is higher than 0.99. The charging efficiency of the IBB-PFCC based OBC is calculated using (4.6), which is given as

$$\text{efficiency} = \frac{P_{BESS}}{P_{ac}} = \frac{v_{bat} * i_{bat}}{v_{ac} * i_{ac} * \cos \theta} , \quad (4.6)$$

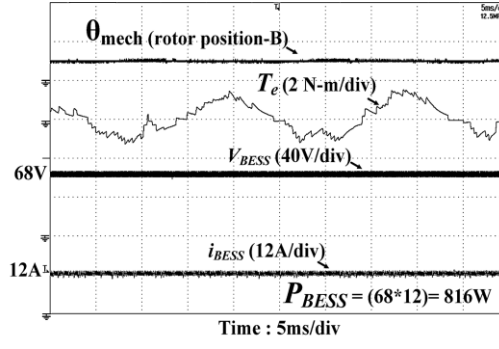
where P_{BESS} denotes the BESS charging power, P_{ac} is the AC grid power. θ denotes the IPF. The charging efficiency of the IBB-PFCC is always greater than 82.66%.



(a)



(b)



(c)

Fig. 4.11. Proposed IML-PCT experimental results during battery charging (a) input AC voltage and current with phase-B and phase-C windings current, (b) input AC voltage and current waveform with phase-A and phase-C windings current, and (c) BESS voltage and current with transient torque generated.

4.3. CONCLUSION

The chapter proposed a fully IML-PCT with driving and battery charging capabilities for SRM drive-based EV application. The main features of the proposed IML-PCT are as follows.

(1) During driving mode, the proposed IML-PCT applies higher phase voltage leading to faster energization and de-energization of the phase current/s. It resulted in an enhanced constant torque and power region for SRM drive.

(2) During battery charging mode, the proposed IML-PCT was utilized as an OBC, which is realized using an IBB-PFCC. The IBB-PFCC cascade with a BDDC facilitates battery charging in CC/CV modes directly via an AC outlet.

Furthermore, when phase windings are reconfigured as charging inductors, the current flowing in it results in zero torque production. Thus, the rotor is standstill without external braking.

CHAPTER 5

INTEGRATED CONVERTER WITH G2V, V2G, AND DC/V2V CHARGING CAPABILITIES FOR SWITCHED RELUCTANCE MOTOR DRIVE-TRAIN BASED EV APPLICATION

The present chapter investigates an IC with driving, grid-to-vehicle (G2V), vehicle-to-grid (V2G), and DC/vehicle-to-vehicle (V2V) charging capabilities for EV drive-train employing SRM. During drive mode, the battery supplies the driving power, and the proposed IC independently controls the individual phases of the SRM. When EV is standstill/ idle, the proposed IC can charge the battery via standard AC and DC charging sockets. For charging the battery via a single-phase residential/public AC outlet, i.e., G2V charging, the proposed IC exhibits a PFC charger. The reconfigured switches are bidirectional, facilitating the flow of power in both directions, i.e., G2V and V2G charging. For fast charging of the battery via DC source, which includes emerging DC grids, solar photovoltaic systems, and battery source of another EV, i.e., V2V charging, the proposed IC exhibits a four-quadrant DC-DC converter (FQDDC). For realizing the inductors of the PFC charger and FQDDC converter, the phase windings of SRM are reconfigured. Thus, the proposed IC eliminates the requirement of any additional non-integrated circuit, which reduces the total switch count. Also, proposed way of reconfiguring inductors results in a standstill rotor at appropriate rotor positions.

5.1. PROPOSED IC DURING DRIVE MODE

Fig. 5.1 shows the proposed IC topology for a 4-phase SRM drive-based EV application. The following subsections in detail discuss the operational modes and the control strategies of the employed IC under the driving mode.

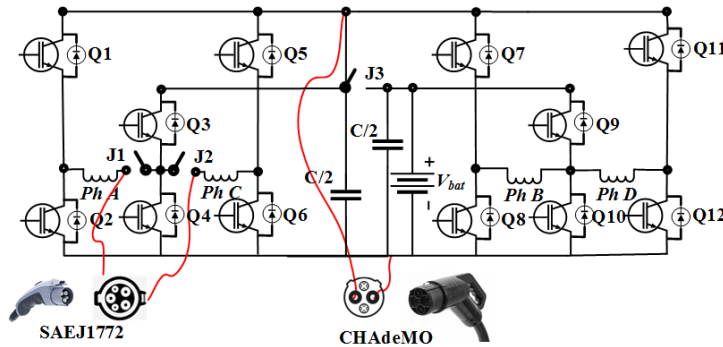


Fig. 5. 1. Proposed IC topology for 4-phase SRM.

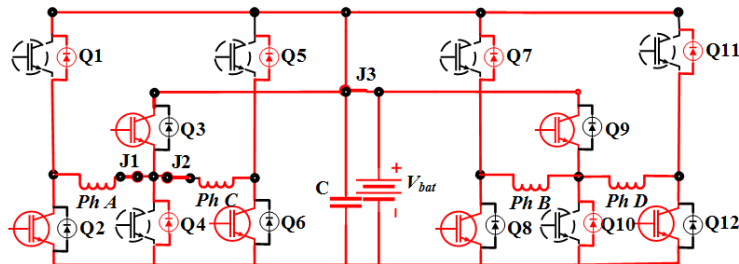


Fig. 5. 2. Proposed IC during drive mode of operation.

5.1.1. OPERATION STATES OF THE PROPOSED IC UNDER DRIVING MODE

During the driving mode, the proposed IC is utilized as a drive converter by closing relay J1, J2, and J3. The resulting drive converter is shown in **Fig. 5.2**. During drive mode, switches Q1, Q4, Q5, Q7, Q10, and Q11 are maintained in an OFF state.

The employed BESS voltage, i.e., V_{bat} , is selected in accordance with the rated SRM voltage. The reconfigured drive converter can apply three voltage levels, i.e., V_{bat} , 0, $-V_{bat}$, as shown in **Fig. 5.3**.

Mode-I-[Fig. 5.3. (a)]: For having a positive phase voltage, i.e., V_{bat} across phase-A winding, switches Q3 and Q2 are switched ON.

Mode-II-[Fig. 5.3 (b)]: For having a zero-phase voltage across phase-A winding only switch, Q2 is switched ON.

Mode-III-[Fig. 5.3. (c)]: For having a negative phase, i.e., $-V_{bat}$ across phase-A winding switches Q1 and Q4 are switched OFF.

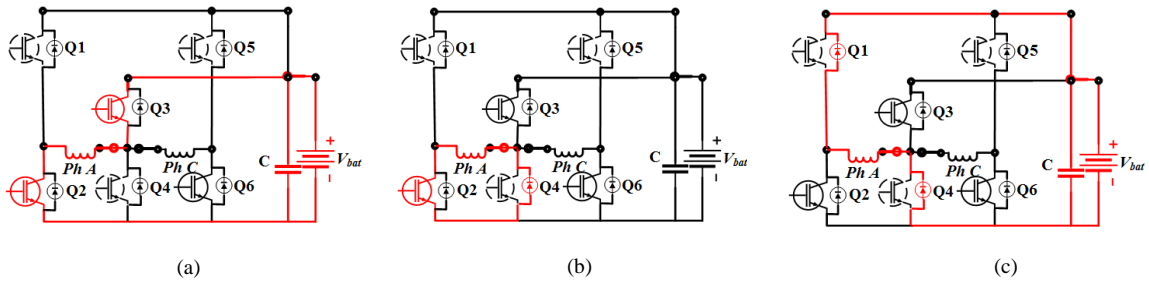


Fig. 5.3. Operating modes during drive mode of operation (a) motoring, (b) free-wheeling, and (c) de-energization.

5.1.2. CONTROL TECHNIQUE

Fig. 5.4. (a) shows the adopted control strategy for controlling the proposed IC during the drive mode of operation. Depending upon the hall sensor inputs (H_a , and H_b), the turn-on signal/s (Q2/Q8/Q6/Q12) corresponding to the active phase/s are generated, as given in **Table. V. I**. The generated phase turn-on signals are given to the current reference generator (CRG) block. The reference current (i_x^*) generated from the outer speed loop is also given as an input to the CRG block.

As shown in **Fig. 5.4. (a)**, the CRG block employs two XOR gates whose output is multiplied by i_x^* for generating the current references, $i_{a/c}^*$ and $i_{b/d}^*$. The input signals for the individual XOR gates are the generated turn-on signals of quadrature-phase pairs (phase-A, phase-C, and phase-B, phase-D). The generated output of the CRG block for the different turn-on signals is given in **Table. V. I**. Two current controllers are employed, whose output is given to the PWM generators, which generate the PWM signals for switches Q3 and Q9.

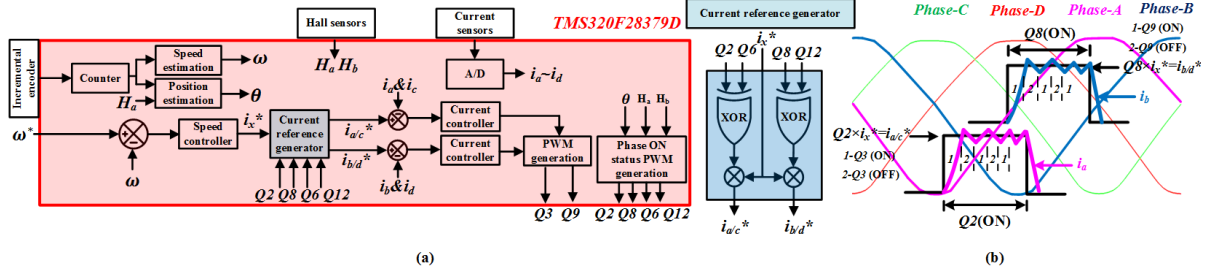


Fig. 5. 4. Adopted control strategy for the proposed IC during the driving mode. (a) control technique, and (b) switching states for the corresponding reference and actual phase currents.

Fig. 5. 4. (b) shows phase-A and phase-B reference and actual phase currents with the switching states of the corresponding switches. During the entire turn-on period of phase-A, switch Q2 is maintained in an ON state. The reference current, i.e., $i_{a/c}^*$, and the actual phase current for phase-A (i_a) are compared, and the output error is given to a current controller block that generates the PWM signal for switch Q3. When switch Q3 is turned ON, i.e., state-1, the phase-A winding is applied with the positive DC-link voltage, as shown in **Fig. 5. 3. (a)**. And when switch Q3 is turned OFF, i.e., state-2, the phase-A winding is applied with a zero-phase voltage, as shown in **Fig. 5. 3. (b)**. Once the turn-on period of phase-A is completed, the status of switch Q2 is set to zero, and the corresponding current reference, i.e., $i_{a/c}^*$ is also set to zero. The zero $i_{a/c}^*$ reference switches the switch Q3 OFF, resulting in a negative DC-link voltage applied across phase-A winding, as shown in **Fig. 5. 4. (c)**.

During the turn-on period of phase-B, switch Q8 is maintained in an ON state. The reference, i.e., $i_{b/d}^*$, and the actual phase currents for phase-B (i_b) are compared, and the error is given to a current controller block that generates the PWM signal for switch Q9. Due to symmetry in the integrated drive converter, the operating states of phase-B are not discussed to avoid repetition.

TABLE. V. I
PHASE TURN-ON SIGNAL GENERATION LOGIC

H_a and H_b	ON signal generated for	$i_{a/c}^*$ (XOR output)	$i_{b/d}^*$ (XOR output)
0 and 0	Q2 (phase-A)	$Q2 \times i_{a/c}^*$	0
0 and 1	Q8 (phase-B)	0	$Q8 \times i_{b/d}^*$
1 and 0	Q6 (phase-C)	$Q6 \times i_{a/c}^*$	0
1 and 1	Q12 (phase-D)	0	$Q12 \times i_{b/d}^*$

5. 2. CONFIGURATION AND CONTROL OF THE PROPOSED IC DURING G2V CHARGING MODE

5.2.1. CONFIGURATION OF THE PROPOSED IC UNDER G2V MODE

When the EV is standstill/idle, the BESS can be charged via a single-phase AC outlet, i.e., G2V charging. For this mode relay, J3 is kept open. The simplified form of the resulting G2V charging topology is shown in **Fig. 5. 5**. The single-phase AC terminals are directly connected to phase-A and phase-C winding nodes. The charging topology is a BB-PFC cascaded to an FQDDC. The switches and inductors required for BB-PFC and FQDDC converter are reconfigured from the drive converter and phase windings. Thus, no additional non-integrated circuit is required.

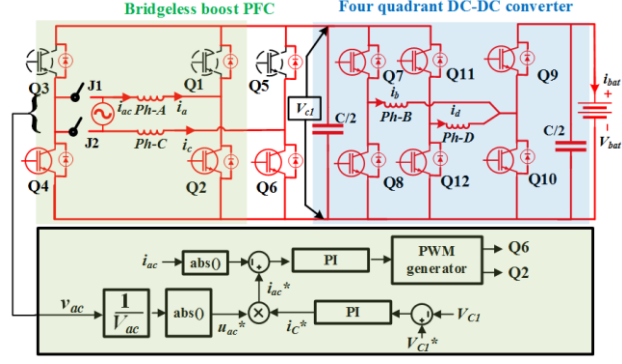


Fig. 5. 5. Proposed IC topology under G2V/V2G charging mode.

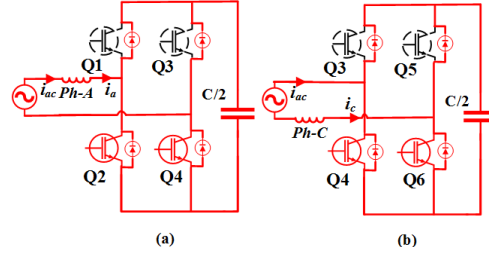


Fig. 5. 6.. Reconfigured boost inductor for BB-PFC when (a) J1- opened, and J2 closed, and (b) J1-closed, and J2-opened.

The additional half-bridge (switches Q3, Q4) available with integrated G2V charger and relays J1 and J2 allow different phase winding/s configurations to be reconfigured as boost inductors in BB-PFC. For reconfiguring both phase-A and phase-C windings as boost inductors, relays J1 and J2 are opened. The BB-PFC is formed using switches Q1, Q2, Q5, and Q6, as shown in **Fig. 5. 5**. For reconfiguring only phase-A winding as boost inductor, relay J1 is opened, relay J2 is closed, and the BB-PFC is formed using switches Q1, Q2, Q3, and Q4, as shown in **Fig. 5. 6. (a)**. Similarly, for reconfiguring only phase-C winding as boost inductor, relay J1 is closed, and relay J2 is opened. The BB-PFC is formed using switches Q3, Q4, Q5, and Q6, as shown in **Fig. 5. 6. (b)**. Thus, depending on the state of relays J1 and J2, phase-A, phase-C, or both phase-A and phase-C windings can be reconfigured as boost inductors, as shown in **Fig. 5. 5** and **Fig. 5. 6**.

The inductor/s for the FQDDC can be realized either via phase-B, phase-D, or both phase-B and phase-D windings. With phase-B winding reconfigured as an inductor, the FQDDC is formed using switches Q7, Q8, Q9, and Q10. And with phase-D winding reconfigured as an inductor, the FQDDC is formed using switches Q11, Q12, Q9, and Q10.

The switching state of relays (J1 and J2) and FQDDC for reconfiguring suitable winding/s as inductor/s in BB-PFC and FQFFC depends on the charging rotor position, which is discussed later in the sections of the chapter.

5. 2. 2. WORKING OF THE INTEGRATED G2V CHARGER

The integrated BB-PFC converts the input AC power to DC power while maintaining the drawn AC power quality. The further discussion assumes that both phase-A and phase-C windings are reconfigured as inductors by opening relay J1 and J2, as shown in **Fig. 5. 5**.

The adopted control strategy for the BB-PFC is shown in **Fig. 5. 5**. The outer voltage control loop aims at maintaining voltage across the DC-link capacitor (V_{cl}) constant to set the reference value (V_{cl}^*). The reference voltage for the DC-link capacitor is set to be greater than the peak voltage of the input AC voltage waveform. The inner control loop maintains the input AC voltage and current in phase by regulating the PWM signals of switch Q2 and Q6 for the positive and negative half cycle, respectively.

Fig. 5. 7 and **Fig. 5. 8** show the operating stages during rectification for the positive and negative half-cycle, respectively. For the positive half-cycle when switch Q2 is ON, the charging current flows through phase-A, Q2, the diode of Q6, and phase-C, as shown in **Fig. 5. 7. (a)**. During this state, the energy is stored in phase-A and phase-C windings. When switch Q2 is switched OFF, stored energy in the windings and AC supply is transferred to the DC-link capacitor through the diodes of switches Q1 and Q6, as shown in **Fig. 5. 7. (b)**. Similarly, the operating states when switch Q6 is controlled during the negative half-cycle are shown in **Fig. 5. 8**. The DC power across DC-link capacitance is then processed via the integrated FQDDC, which maintains the charging profile of the BESS. The further discussion assumes that both phase-B and phase-D windings are reconfigured as inductors in the FQDDC.

For BESS voltage (V_{bat}) smaller than the set voltage across the DC-link capacitor (V_{cl}), the FQDDC is operated in buck mode, i.e., the voltage across the DC-link capacitor is stepped down. When switches Q7 and Q11 are switched ON, the current flows through Q7/ Q11, phase-B/ phase-D, and the diode of Q9, as shown in **Fig. 5. 9. (a)**. When switches Q7 and Q11 are switched OFF, the stored energy in phase-B/phase-D windings is transferred to the BESS through diodes of Q8/Q12 and Q9, as shown in **Fig. 5. 9. (b)**.

For BESS voltage greater than the set voltage across the DC-link capacitor, the FQDDC is operated in boost mode, i.e., the voltage across the DC-link capacitor is stepped up. For boost mode of operation, switches Q7 and Q11 are maintained in an ON state. When switch Q10 is switched ON, the current flows through Q7/ Q11, phase-B/ phase-D, and Q10 resulting in charging the reconfigured inductors, as shown in **Fig. 5. 10. (a)**. When switch Q10 is switched OFF, the stored energy in phase-B/phase-D windings and the DC-link capacitor is applied to the BESS through the diode of Q9, as shown in **Fig. 5. 10. (b)**. **Table. V. II** gives the operational modes and switching states of the switches in the FQDDC.

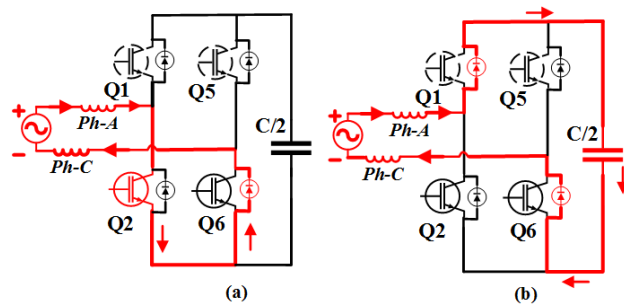


Fig. 5. 7. PFC operation of the BB-PFC during the positive half cycle. (a) Switch ON state. (b) Switch OFF state.

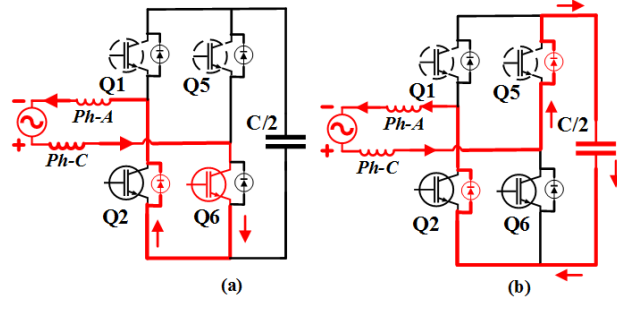


Fig. 5. 8. PFC operation of the BB-PFC during the negative half cycle. (a) Switch ON state. (b) Switch OFF state.

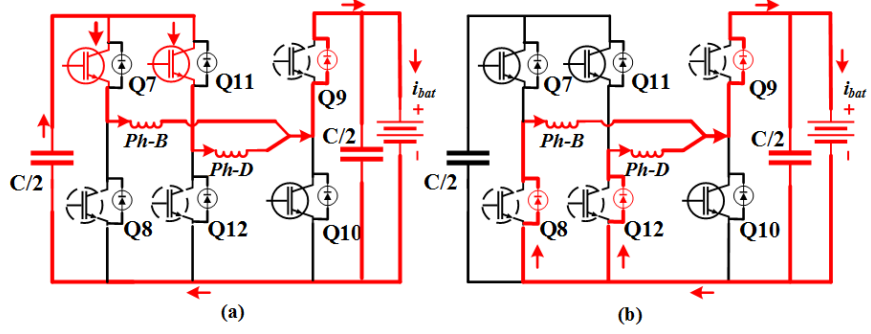


Fig. 5. 9. FQDDC operational states under buck mode of operation. (a) Switch ON state. (b) Switch OFF state.

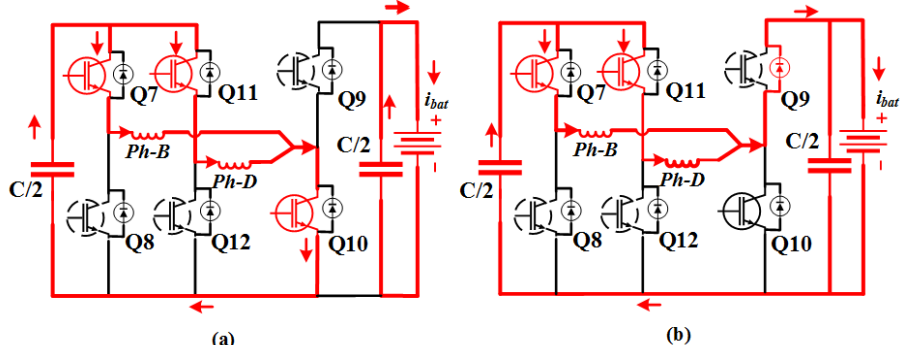


Fig. 5. 10. FQDDC operational states under boost mode of operation. (a) Switch ON state. (b) Switch OFF state.

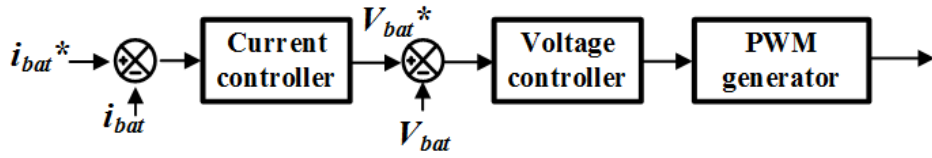


Fig. 5. 11. Control scheme for the FQDDC.

TABLE V. II
OPERATION MODES OF FQDDC DURING G2V CHARGING

Voltage	Mode	Q7/Q11	Q8/Q12	Q9	Q10
$V_{cl} > V_{bat}$	Buck	Active	OFF	OFF	OFF
$V_{cl} < V_{bat}$	Boost	ON	OFF	OFF	Active

Fig. 5. 11. shows the control scheme for the FQDDC. The scheme is mainly comprised of two control loops. The outer current control loop regulates the switching to track the voltage control loop regulates the charging voltage. For instance, constant current charging is implemented if the output of the outer current loop (V_{bat}^*) does not exceed the specified charging voltage ($V_{bat-max}$). If the output of the outer current loop exceeds the specified charging voltage, constant voltage charging is implemented. These correspond to the case wherein the outer current loop operates in saturation.

5. 3. CONFIGURATION OF THE PROPOSED IC DURING DC/V2V CHARGING MODE

When the EV is standstill/idle for fast charging of BESS via DC source, the proposed IC is reconfigured as FQDDC. The DC source/load is connected across the DC-link capacitor, i.e., terminals A and B (V_{AB}), as shown in **Fig. 5. 12**. Relay J1, J2, and J3 are kept open for this mode of operation.

The voltage rating of the source/load with respect to the BESS voltage is not a matter of concern, as the FQDDC can operate in buck and boost mode bidirectional.

5. 3. 1. BESS CHARGING VIA SOLAR PV

With the proposed IC, the BESS can be charged through a solar PV system by connecting it to BESS through the integrated FQDDC. The solar PV system can be installed on (EV1) or external to the EV, as shown in **Fig. 5. 12**. The integrated FQDDC implements the maximum power point tracking (MPPT) algorithm, thus eliminating the need for an additional DC-DC converter. The perturbed and observed-based MPPT algorithm is implemented to optimize the performance of the solar PV system. For a solar PV system of voltage rating higher than the BESS voltage, i.e., the voltage across $V_{AB} > V_{bat}$, the FQDDC operates in buck mode. And for a solar PV system of voltage rating lesser than the BESS voltage, i.e., the voltage across $V_{AB} < V_{bat}$, the FQDDC operates in boost mode. The operating states of the FQDDC during the buck and boost mode of operation are shown in **Fig. 5. 9** and **Fig. 5. 10**, respectively.

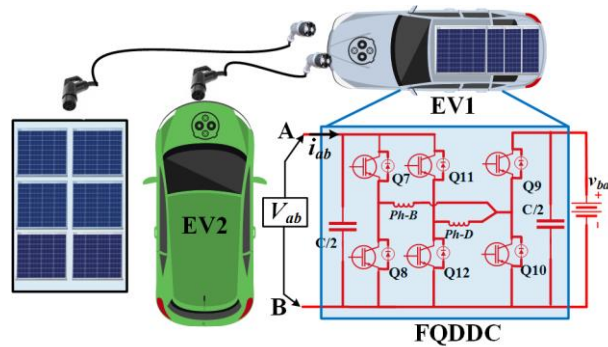


Fig. 5. 12. Proposed IC configuration during DC/V2V charging mode.

5. 3. 2. BESS CHARGING/DISCHARGING VIA ANOTHER EV BESS (EV2), I.E., V2V CHARGING/DISCHARGING

With the proposed IC, the BESS (of EV1) can be charged/discharged through another EV (EV2) via the integrated FQDDC. To simplify the discussion, the power flow direction is considered *forward* if the power flow direction is from EV2 to EV1, where EV2 is considered the *provider*. And the power flow direction is considered *reverse* if the power flow direction is from EV1 to EV2, where EV2 is considered the *receiver*. The forward/reverse buck or forward/reverse boost mode of operation is decided based on EV1 BESS voltage (V_{bat}), the voltage output of EV2 connected across terminals A and B (V_{AB}), and the role of EV2 (*provider/receiver*).

The operating modes under the forward buck and forward boost mode of operation are discussed and shown in **Fig. 5. 9** and **Fig. 5. 10**. For the reverse buck and reverse boost mode of operation, the BESS of EV1 discharges to EV2.

For discharging BESS of EV1 to EV2 of a smaller rating, i.e., $V_{AB} < V_{bat}$, the FQDDC is operated in reverse buck mode. When switch Q9 is switched ON, the current flows through Q9, phase-B/ phase-D, and the diodes of Q7/ Q11, as shown in **Fig. 5. 13. (a)**. When switch Q9 is switched OFF, the current flows through the diode of Q10, phase-B/ phase-D, and the diodes of Q7/ Q11, as shown in **Fig. 5.13. (b)**.

For discharging BESS of EV1 to EV2 of a higher rating, i.e., $V_{AB} > V_{bat}$, the FQDDC is operated in reverse boost mode. For the reverse boost mode of operation, switch Q9 is maintained in an ON state. When switches Q8 and Q12 are switched ON, the current flows through Q9, phase-B/ phase-D, and Q8/Q12 resulting in charging the reconfigured inductors, as shown in **Fig. 5. 14. (a)**. When switches Q8 and Q12 are switched OFF, the stored energy in phase-B and phase-D windings and BESS voltage is applied to the DC-link capacitor through diodes of Q7/Q11, as shown in **Fig. 5. 14. (b)**.

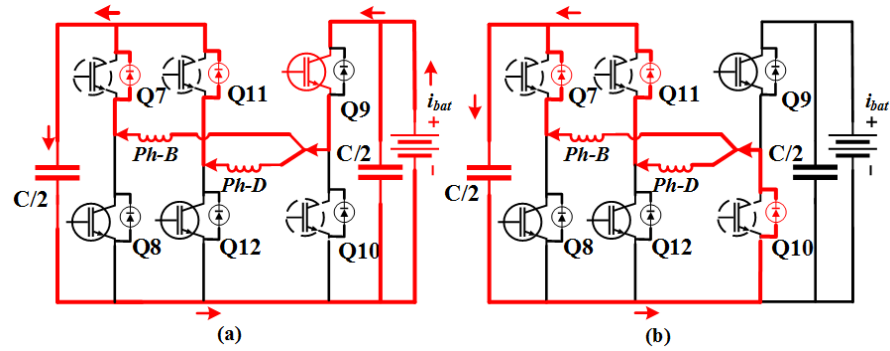


Fig. 5. 13. FQDDC operational states under reverse buck mode of operation. (a) Switch ON state. (b) Switch OFF state.

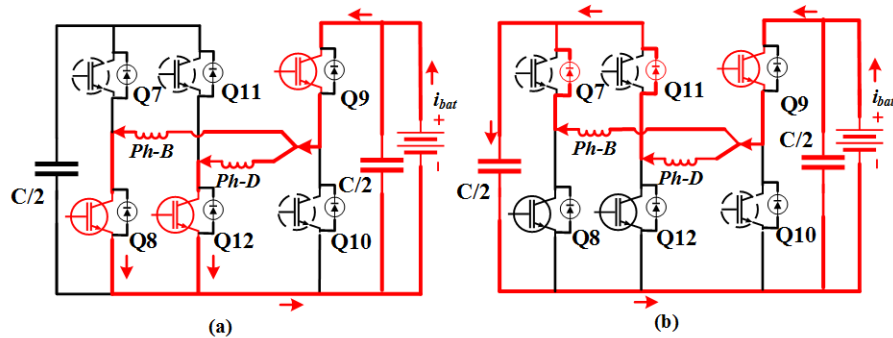


Fig. 5. 14. FQDDC operational states under reverse boost mode of operation. (a) Switch ON state. (b) Switch OFF state.

5. 4. CONFIGURATION AND CONTROL OF THE PROPOSED IC DURING V2G CHARGING MODE

When the EV is standstill/idle, the BESS can be discharged to a single-phase AC grid, i.e., V2G charging. For this mode relay, J3 is kept open. Similar to G2V charging, the single-phase AC grid terminals are directly connected to phase-A and phase-C winding nodes. Also, the simplified form of the resulting V2G charging topology is similar to that of the G2V charging topology which is shown in **Fig. 5. 5**. Thus, simultaneous G2V and V2G charging can be done depending on the control/ user input.

Similar to G2V mode, the filter inductance/s during V2G mode can be reconfigured via phase-A, phase-C, or both phase-A and phase-C windings. The operating state of relay J1 and J2 decides which phase winding/s to be reconfigured.

The integrated FQDDC operates in reverse buck or reverse boost mode to achieve the required DC-link voltage. The operating states of the FQDDC during the reverse buck and reverse boost mode of operation are shown in **Fig. 5.13** and **Fig. 5. 14**, respectively. The required DC-link voltage depends on the AC grid voltage connected across phase-A and phase-C winding nodes. **Fig. 5. 15** and **Fig. 5.16** show the half-cycle operation of the cascaded inverter stage of the integrated V2G charger.

During the positive half-cycle ($V_{ac} > 0$), Q6 is always ON, and Q5 and Q2 are OFF. The PWM signal generated via the control loop control is applied to Q1. During the ON state of switch Q1, negative grid current ($i_{ac} < 0$) flows through phase-A, phase-C windings, switch Q6, the DC-link capacitor, and switch Q1, as shown in **Fig. 5. 15. (a)**. During the OFF state of switch Q1, only Q6 is ON, which implies that the negative grid current flows through phase-A, phase-C windings, switch Q6, and the diode of switch Q2, as shown in **Fig. 5. 15. (b)**. Similarly, for the negative half-cycle ($V_{ac} < 0$), Q2 is always ON, and Q1 and Q6 are OFF. The PWM signal is applied to Q5, and the path of positive grid current ($i_{ac} > 0$) for switching states of Q5 is shown in **Fig. 5. 16**.

Fig. 5. 17 shows the control scheme during V2G charging. The negative grid current ($-1 * i_{ac}$) implies that real power is injected into the connected single-phase AC grid.

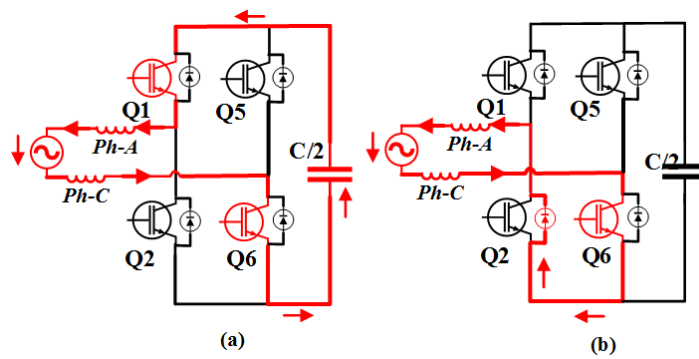


Fig. 5. 15. Current path during V2G operation for the positive half cycle. (a) Switch ON state. (b) Switch OFF state.

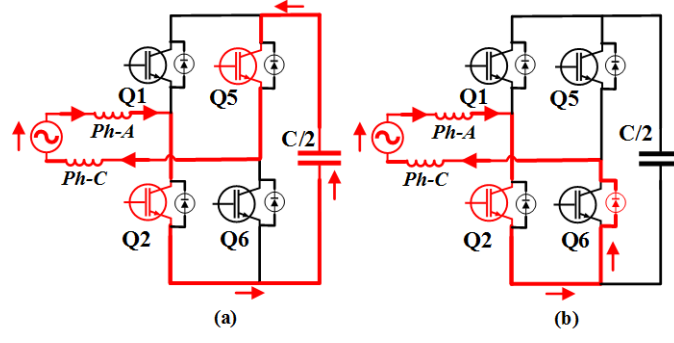


Fig. 5. 16. Current path during V2G operation for the negative half cycle. (a) Switch ON state. (b) Switch OFF state.

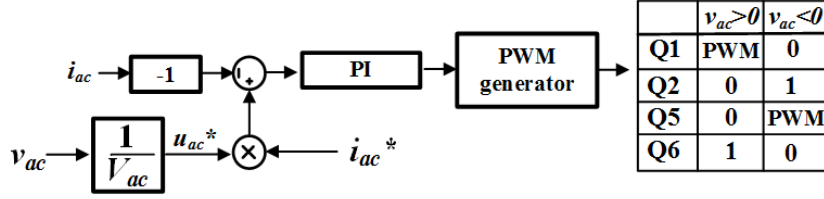


Fig. 5. 17. Adopted control technique during V2G mode of operation.

5. 5. CHARGING ROTOR POSITIONS AND TORQUE ANALYSIS

As discussed in earlier sections, the phase windings of the SRM are reconfigured to achieve various functionalities related to inductors. Phase-A and phase-C windings are reconfigured as boost inductor/s in BB-PFC during G2V charging and filter inductance/s during V2G charging mode. The reconfiguration of either phase-A, phase-C, or both as inductors depends on the switching state of relay J1 and J2. Similarly, for DC/ V2V charging/discharging mode, phase-B and phase-D winding/s are reconfigured as inductors in the FQDDC. The reconfiguration of either phase-B, phase-D, or both as inductors depends on the switching of FQDDC. The switching state of relays and FQDDC is depended on the charging rotor position.

The present section discusses four charging positions at which the total charging torque (TCT) due to current in selected reconfigured phases results in a net-zero charging torque (ZCT). The approximated partial differential equation for the instantaneous phase torque ($T_e(\theta, i)$) for SRM is given by

$$T_e(\theta, i) = i^2 \frac{\partial L(\theta, i)}{\partial \theta} \quad (5.1)$$

where, $L(\theta, i)$ is the phase inductance as a function of rotor position and phase current. The TCT at any of the proposed rotor positions is given by

$$T_{\text{net}} = T_a + T_b + T_c + T_d \quad (5.2)$$

where T_a , T_b , T_c , and T_d denote the phase torque for phase-A, phase-B, phase-C, and phase-D, respectively.

Fig. 5.18 shows the actual inductance profile obtained using the finite element analysis (FEA) of the prototype 4-phase SRM. The proposed four charging rotor positions, i.e., A1, A2, A3, and A4, are marked. And the discussion on the TCT and the phase winding/s to be reconfigured as inductors is carried out below.

5.5.1. ROTOR POSITION-A1 AND ROTOR POSITION-A3

At rotor position-A1 and A3, the torque generated due to current in phase-A and phase-C windings is given by

$$T_a = \frac{1}{2} K_a i_a^2, \text{ and } T_c = \frac{1}{2} K_c i_c^2 \quad (5.3)$$

where i_a and i_c are the currents through phase-A and phase-C windings. And K_a and K_c denote the slope of the inductance profile with respect to the rotor position for phase-A and phase-C windings, respectively. At rotor position-A1 and A3, K_a and K_c are equal and opposite, as seen in **Fig. 5. 18**, and mathematically given by

$$K_a = - K_c. \quad (5.4)$$

When both phase-A and phase-C are reconfigured as inductors, the integrated G2V/V2G charger topology allows an equal flow of current in both phases, i.e., $|i_a| = |i_c|$. The working of the integrated G2V/V2G charger is shown in **Fig. 5. 7** and **Fig. 5. 15**. Thus, the torque produced due to equal charging current in phase-A and phase-C winding is equal and opposite, i.e.,

$$T_a = - T_c. \quad (5.5)$$

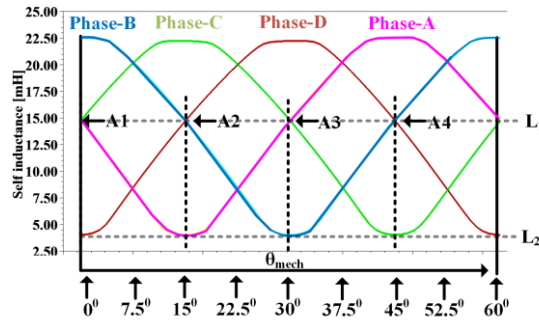


Fig. 5. 18. Inductance profile of prototype 4-phase SRM.

Form (6.5), the net torque due to current in phase-A and phase-C windings is zero. For the FQDDC, at rotor position-A1, phase-D winding is reconfigured as an inductor. This is because the current in phase-D winding results in zero-torque production as K_d is zero. Similarly, at rotor position-A3, the phase-B winding is reconfigured as an inductor for the FQDDC.

Thus, at rotor position-A1, the TCT due to current in phase-A, phase-C, and phase-D windings reconfigured as inductors result in net ZCT. Similarly, at rotor position-A3, the TCT due to current in phase-A, phase-C, and phase-B windings reconfigured as inductors result in net ZCT.

$$T_{net} = T_a + T_c + T_b / T_d = 0 \quad (5.6)$$

5.5.2 ROTOR POSITION-A2

At rotor position-A2, the torque generated due to current in phase-A results in zero-torque production as K_a is zero. Thus, only phase-A winding is reconfigured as an inductor in the G2V/V2G charger topology by opening relay J1 and closing relay J2, as shown in **Fig. 5.7. (a)**.

For the FQDDC, both phase-B and phase-D windings are reconfigured as inductors. This is because K_b and K_d , which denotes the slope of the inductance profile for phase-B and phase-D windings, are equal and opposite, as seen in **Fig. 5.18**, and mathematically given by

$$K_b = - K_d. \quad (5.7)$$

Thus, according to (6.1), if equal current flows in phase-B and phase-D windings, it produces equal and opposite torque. As seen from **Fig. 5.6**, phase-B and phase-D windings connects in parallel if the same PWM signal is applied to switches Q7 and Q11. Moreover, as seen from **Fig. 5.18**, the inductance offered by phase-B and phase-D at rotor position-A2 is equal, implying equal current division among the parallelly connected phase windings, i.e., $|i_b| = |i_d|$. Thus the charging torque due to the charging current in phase-B and phase-D is equal and opposite, resulting in canceling out one another torque, i.e.,

$$T_b = - T_d. \quad (5.8)$$

At rotor position-A2, the TCT due to current in phase-A, phase-B, and phase-D windings reconfigured as inductors result in net ZCT, i.e.,

$$T_{net} = T_a + T_b + T_d = 0. \quad (5.9)$$

5.5.3. Rotor position-A4

At rotor position-A4, the torque generated due to current in phase-C results in zero-torque production as K_c is zero. Thus, only phase-C winding is reconfigured as an inductor in the G2V/V2G charger topology by closing relay J1 and opening relay J2, as shown in **Fig. 5.6. (b)**.

For the FQDDC, both phase-B and phase-D windings are reconfigured as inductors. The operating conditions are similar to that discussed for rotor position-A2. Hence not discussed here to avoid repetition. Thus, at rotor position-A4, the TCT due to current in phase-C, phase-B, and phase-D windings reconfigured as inductors result in net ZCT, i.e.,

$$T_{net} = T_c + T_b + T_d = 0 \quad (5.10)$$

Thus, from (6.6), (6.9), and (6.10), it is observed that for G2V/V2G charging with selected reconfigured phases at any of the rotor positions discussed results in net ZCT. **Table. V. III** summarizes the reconfigured phase windings at different charging rotor positions discussed.

For displacing the rotor to the nearest charging rotor position from the EV parking position, the control disengages the clutch, which disengages the power transmission from the drive shaft to the driven shaft. After shaft power disengagement, appropriate phases are excited for rotor displacement to its nearest charging rotor position.

TABLE V. III
RECONFIGURED PHASE WINDING/S FOR DIFFERENT ROTOR POSITIONS

J1 and J2 status	Boost inductor/ Filter inductor	Inductor in FQDDC	Position
O O	Phase-A and Phase-C	Phase-D	A1
O O	Phase-A and Phase-C	Phase-B	A3
O C	Phase-A	Phase-B and Phase-D	A2
C O	Phase-C	Phase-B and Phase-D	A4
C C	--Not Valid--		

O-Open, C-Closed

5. 6. EXPERIMENTAL RESULTS

For experimentally validating the stated claims of the employed IC, experiments are performed on a prototype 1.1 kW 4-phase 8/6 SRM. For the digital implementation of all the control strategies, TMS320-F28379D DSP is employed. The sampling frequency of the DSP is set to 50 kHz, and the operating switching frequency across all control strategies is 15 kHz. Six SKM75GB12T4 IGBT half-bridge modules from SEMIKRON are used for building the proposed IC. For emulating the BESS (V_{bat}), the battery emulator feature of a bidirectional power supply (ITECH-6012B) is used. The battery emulator voltage (V_{bat}) is set at 120 V, a serial connection of ten 12V/15 AH cells.

For emulating the solar PV system and BESS of EV2 for DC/V2V charging, an SM500-CP-90 bidirectional power supply from DELTA is used. The experimental testbench is shown in **Fig. 5. 19**.

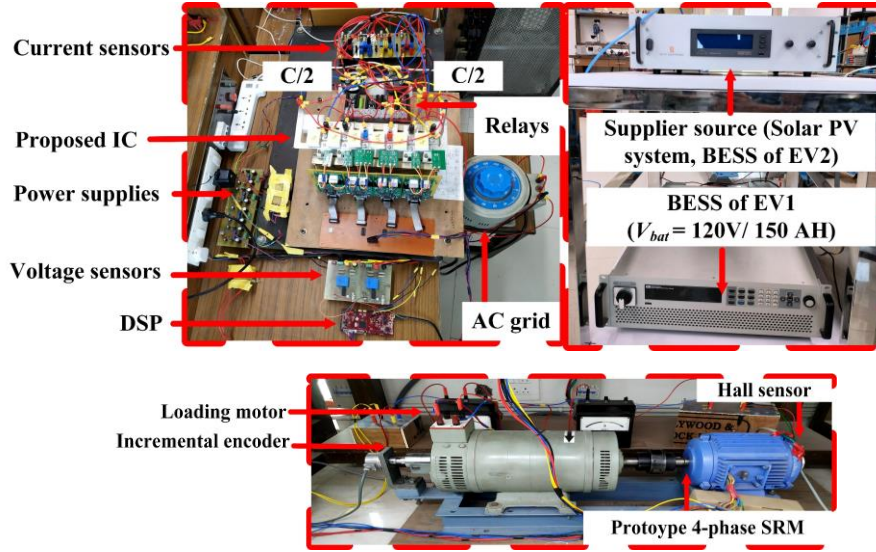


Fig. 5. 19. Experimental testbench.

5.6.1. EXPERIMENTAL RESULTS UNDER DRIVING MODE

For the driving mode, the SRM is coupled to a loading motor, as shown in **Fig. 5.19**. **Fig. 5. 20. (a)** and **Fig. 20. (b)** shows the steady-state response for 500 rpm (load torque =1.9 N-m) and 3000 rpm (maximum operating speed) when the proposed IC is reconfigured as a drive converter. **Fig. 5. 20** shows the experimental phase-A voltage and current waveforms with adjacent phase-B and quadrature phase-C current waveforms.

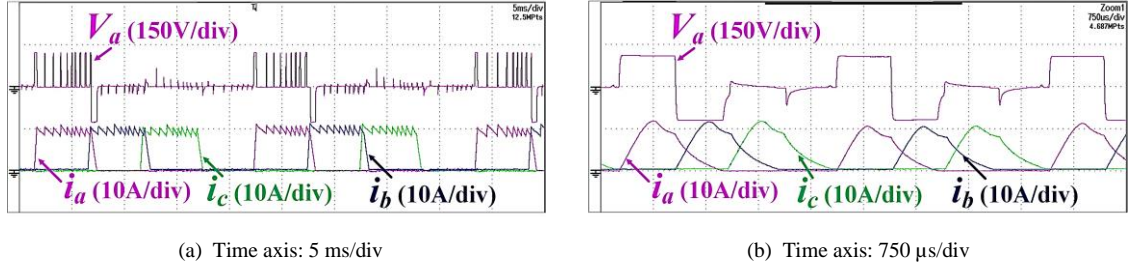


Fig. 5. 20. Steady state response during drive mode of operation for (a) 500 rpm, and (b) 3000 rpm.

5.6.2. G2V CHARGING

For charging BESS via single-phase AC supply, the AC terminals are connected to the phase-A and phase-C winding nodes, and the proposed IC is reconfigured as BB-PFC cascaded to FQDDC, as shown in **Fig. 5.5**. Depending on the charging position, the proposed IC allows different phase- winding configurations to be reconfigured as inductors in BB-PFC and FQDDC to achieve ZCT, as discussed in earlier subsections.

The experimental AC grid voltage and current waveform for different charging rotor positions discussed with a battery charging current reference (i_{bat}^*) of 10A are shown in **Fig. 5.21**. **Fig. 5.21** also shows the phase-A, and phase-C currents waveform, which depending on the charging rotor position, is/ are reconfigured as boost inductor/s.

The voltage across the DC-link capacitor (V_{cl}^*) is set and maintained at 400 V by the control strategy, as shown in **Fig. 5.5**. The BB-PFC maintains the voltage across the DC-link capacitor to a set value of 400 V. Thus, for maintaining the charging voltage and current profile of BESS, the FQDDC is operated in buck mode. **Fig. 5.22** shows the phase-B, and phase-D currents waveform, which depending on the charging rotor position, is/ are reconfigured as inductor/s in FQDDC.

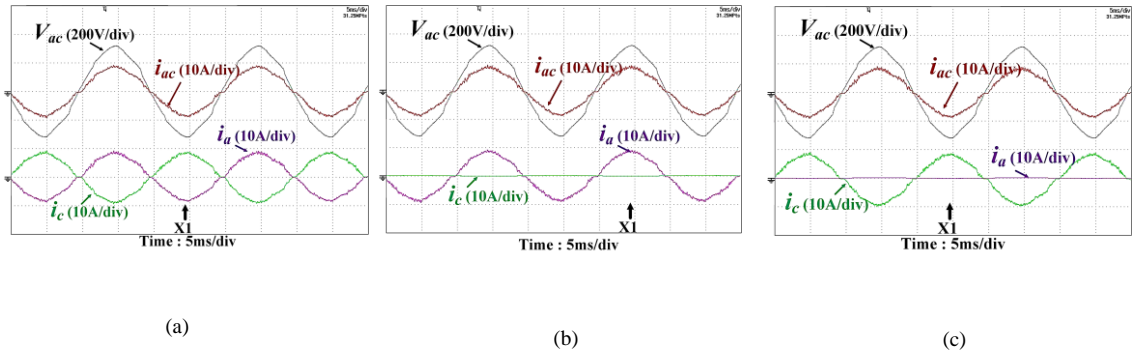


Fig. 5. 21. Experimental waveforms for AC grid voltage, current and phase-A, phase-C currents for a battery charging current reference of 10A when charging is performed at rotor position (a) A1, (b) A2, and (c) A4.

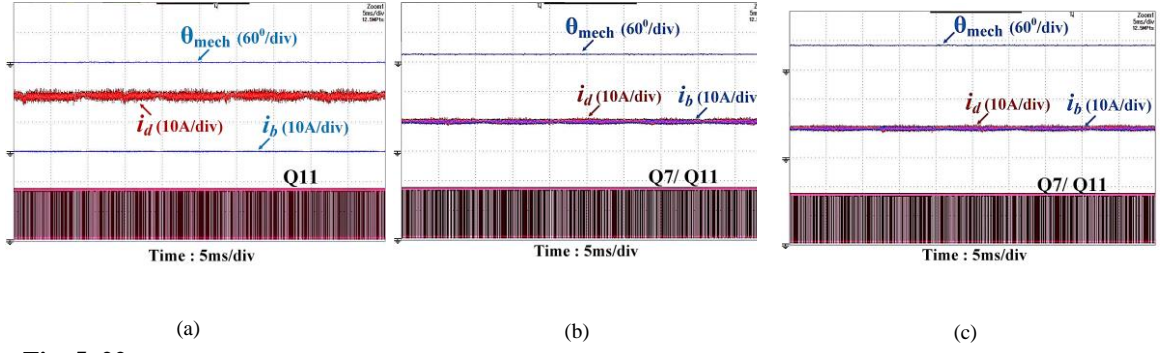


Fig. 5. 22. Experimental obtained rotor position, phase-B, and phase-D currents for a battery charging current reference of 10A when charging is performed at rotor position (a) A1, (b) A2, and (c) A4.

Fig. 5. 21. (a) shows the results when battery charging is performed at rotor position-A1. At rotor position-A1, both phase-A and phase-C windings are reconfigured as inductors in the BB-PFC, discussed in prior sub-sections. When both phase-A and phase-C windings are reconfigured, the AC current flows through both the phase windings, as shown in **Fig. 5.7** and **Fig. 5.8**. Thus, both phases have equal and opposite currents in them, i.e., $i_{ac} = i_a = -i_c$, as seen in **Fig. 5. 21. (a)**.

Fig. 5. 22. (a) shows the stationary rotor position during charging at rotor position-A1. Also, at rotor position-A1, only phase-D winding is reconfigured as an inductor in FQDDC. Thus, the complete battery charging current flows through phase-D winding only, i.e., $i_d = i_{bat}$, and $i_b = 0A$, as seen in **Fig. 5. 22. (a)**. The corresponding PWM signals of switch Q11 for operating the FQDDC in buck mode are also shown.

Fig. 5. 21. (b) shows the results when battery charging is performed at rotor position-A2. At rotor position-A2, only phase-A winding is reconfigured as an inductor in the BB-PFC, as discussed. Thus, the AC current flows only through phase-A winding, i.e., $i_{ac} = i_a$, as seen in **Fig. 5. 21. (b)**. **Fig. 5. 22. (b)** shows the stationary rotor position during charging at rotor position-A2. For the FQDDC, both phase-B and phase-D are reconfigured as inductors. Thus, the total battery charging current is equally divided among phase-B and phase-D windings, i.e., $i_{bat}/2 = i_b = i_d$, as seen in **Fig. 5. 22. (b)**. The corresponding PWM signals for switches Q7 and Q11 for operating the FQDDC in buck mode are also shown.

Fig. 5. 21. (c) shows the results when battery charging is performed at rotor position A4. At rotor position A4, only phase-C winding is reconfigured as an inductor in the BB-PFC as discussed. Thus, the AC current flows only through phase-C winding, i.e., $i_{ac} = -i_c$, as seen in **Fig. 5.21. (c)**. **Fig. 5.22. (c)** shows the stationary rotor position during charging at rotor position-A4. For the FQDDC, both phase-B and phase-D are reconfigured as inductors.

Thus, the total battery charging current is equally divided among phase-B and phase-D windings, i.e., $i_{bat}/2 = i_b = i_d$, as seen in **Fig. 5.22. (c)**. The corresponding PWM signals for switches Q7 and Q11 for operating the FQDDC in buck mode are also shown.

The response of the G2V charger when charging at the rotor position-A3 is similar to that of rotor position-A1. The only difference is that at rotor position-A3 for the FQDDC, instead of phase-D, phase-B is reconfigured as an inductor (i.e., $i_b = i_{bat}$, and $i_d = 0A$). Hence not shown to avoid repetition. The efficiency (η) of the G2V charger is calculated using (6.11),

$$\eta = \frac{P_{BESS}}{P_{ac}} = \frac{v_{bat} * i_{bat}}{v_{ac} * i_{ac} * \cos \theta} \quad (5.11)$$

where P_{BESS} is the BESS charging power, and power drawn from the AC source is given by P_{ac} . The input power factor angle is denoted by, θ , which is always greater than 0.98. The calculated efficiency is around is 83.6%.

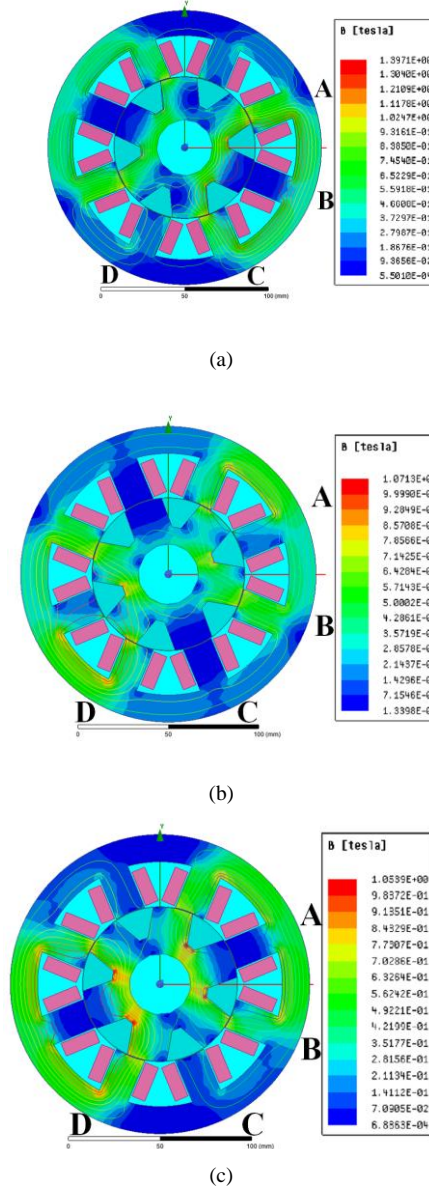


Fig. 5. 23. FEA of magnetic flux density (B) for the marked instant when charging is performed (a) rotor-position A1, (b) rotor-position A2, and (c) rotor-position A4.

Fig. 5.23 shows the FEA of magnetic flux density when charging at rotor positions A1, A2, and A4. The X1 instant for which the FEA is shown is marked in **Fig. 5.21**. Here, the FEA analysis shows that the developed magnetic field density is still lesser than the rated B of the core used (M43-29G). Thus the core remains unsaturated when rated current flows in the reconfigured winding/s during G2V charging.

5.6.3. DC/ V2V CHARGING/DISCHARGING

The DC source/load terminals are connected across the DC-link capacitor (*terminals A and B*), as shown in **Fig. 5.12** for charging/discharging of BESS. The proposed IC during DC/V2V charging is reconfigured as an FQDDC.

The solar PV system is connected across terminals A and B for charging BESS. The solar PV system source can be on or external to the EV. The solar PV system is operated at 600W/m^2 irradiation and the maximum supplied power at the specified irradiation is 1200 W. The integrated FQDDC implements the MPPT algorithm. Moreover, the FQDDC can be operated in buck or boost mode depending on the output switching. For experimental demonstration, the FQDDC is operated in buck mode, as $V_{AB}(200\text{V}) > V_{bat}(120\text{V})$. The operating states of FQDDC for buck mode of operation are shown in **Fig. 5.9**.

Fig. 5. 24 represents the behavior of “ $i_{PV-V_{PV}}$ ” and “ $P_{PV-V_{PV}}$ ” curves for the working condition mentioned. The measured solar PV system voltage ($V\text{-mea}$), current ($I\text{-mea}$), power ($P\text{-mea}$), and MPPT tracking efficiency are 201.129V, 5.581 A, 1172.792 W, and 97.82 %, respectively, as shown in **Fig. 5.24**.

Fig. 5. 25. (a) and **Fig. 5. 25. (b)** shows the response of the employed IC when for V2V operation, the

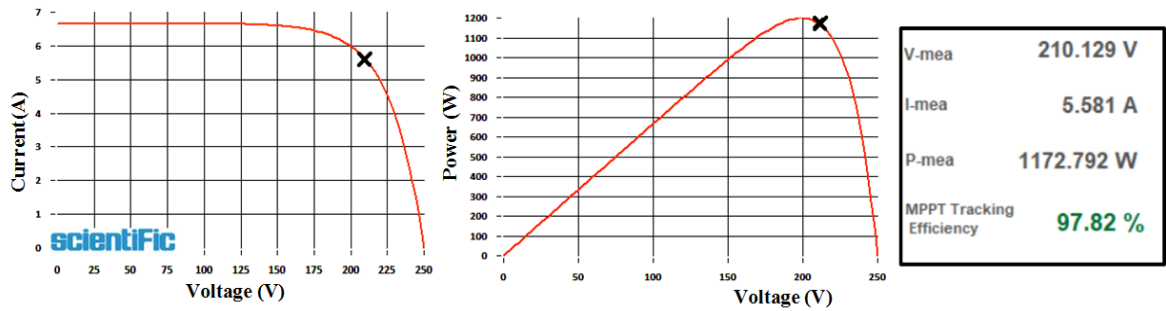


Fig. 5. 24. “ $i_{PV-V_{PV}}$ ” and “ $P_{PV-V_{PV}}$ ” curves and MPPT performance.

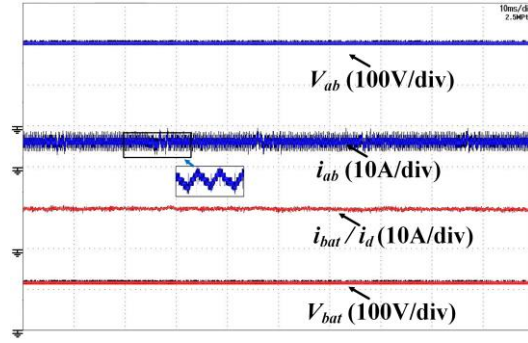
integrated FQDDC is tested for buck mode of operation. The connected voltage across terminals A and B (*EV2 voltage*) is set to 200V, and the control scheme, as shown in **Fig. 5. 11**, is applied for charging the BESS. The reference BESS charging current is set to 10A.

Fig. 5. 25. (a) and **Fig. 5. 25. (b)** shows the voltage and the current flowing in from terminals A and B with BESS voltage and current when charging at rotor position-A1 and rotor position-A2, respectively. At rotor position-A1, only phase-D winding is reconfigured as an inductor. Thus, total BESS current flows through phase-D winding, i.e., $i_d = i_{bat}$. At rotor position-A3, both phase-B and phase-D windings are reconfigured as inductors. Thus, the BESS current is equally divided among phase-B and phase-D windings, i.e., $i_{bat}/2 = i_b = i_d$, and $i_{bat} = i_b + i_d$.

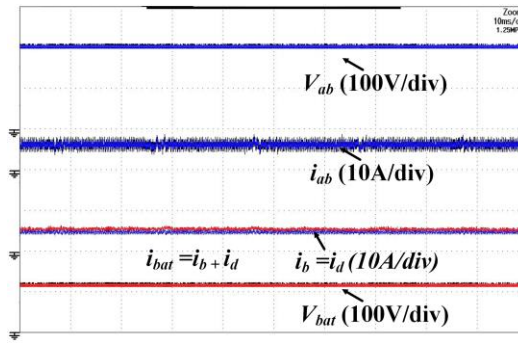
The response of the integrated FQDDC during buck mode of operation for rotor position-A3 and rotor position-A4 is similar to that of rotor position-A1 and rotor position-A3, respectively. Hence not shown to avoid repetition.

Fig. 5.25. (c) shows the V2V discharging mode of operation. Here the BESS discharges to BESS of EV2 connected across terminals A and B. The voltage of EV2 connected across terminals A and B is 200 V. Thus, for experimental demonstration, the FQDDC is operated in reverse boost mode, as $V_{AB}(200\text{V}) > V_{bat}(120\text{V})$.

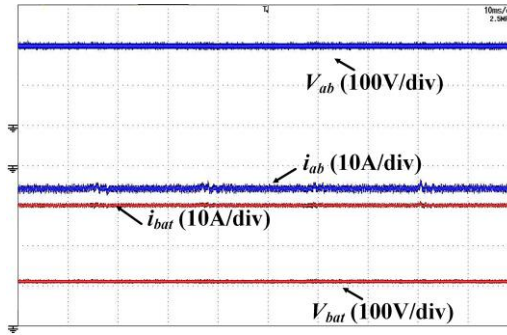
Here both i_{ab} and i_{bat} are negative as the current flowing out of the terminal A and B, and the battery is considered negative.



(a)



(b)



(c)

Fig. 5. 25. Experimental waveform for V2V charging operation when integrated FQDDC operates in buck mode at (a) rotor position-A1, (b) rotor position-A3. (c) Experimental waveform for V2V discharging operation when integrated FQDDC operates in reverse boost mode at rotor position-A1.

5.6.4. V2G charging

For V2G charging, the AC terminals are connected to the windings nodes, and the proposed IC is reconfigured as FQDDC cascaded to a voltage source inverter (VSI).

For V2G mode the reconfiguration of phase winding/s as filter inductor/s depends upon the charging rotor position, as discussed. The experimental AC grid voltage and current waveform when charging at rotor position-A1 for a reference AC current (i_{ac}^*) of 10A are shown in **Fig. 5. 26**. **Fig. 5. 17** shows the control strategy for V2G mode of operation. At rotor position-A1, both phase-A and phase-C windings are reconfigured as inductors.

Thus equal and opposite current flows through both the phases, as seen in **Fig. 5. 26. Fig. 5.15** and **Fig. 5. 16** show the operating states of the VSI during the V2G mode of operation.

The FQDDC depending upon the required DC-link voltage, operates in reverse buck or reverse boost mode of operation. The DC-link voltage is set to 400V; thus, for experimental demonstration, the FQDDC is operated in reverse boost mode, as $V_{AB} > V_{bat}$.

In summary, the provided experimental results show that the proposed IC for SRM drive can operate during driving, G2V mode, V2G mode, and DC/V2V charging/discharging mode with phase winding/s reconfigured as inductor/s. Thus, the proposed IC eliminates the requirement of an additional non-integrated component. The flowchart diagram of steps involved in selecting and operating during different modes of the proposed IC is shown in **Fig. 5. 27**.

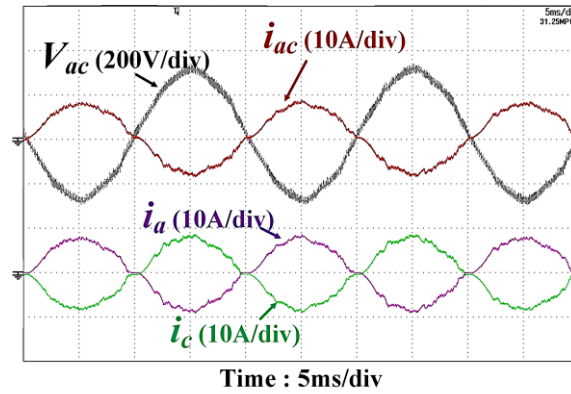


Fig. 5. 26. Experimental waveform of AC grid voltage, current and respective phase currents during V2G operation.

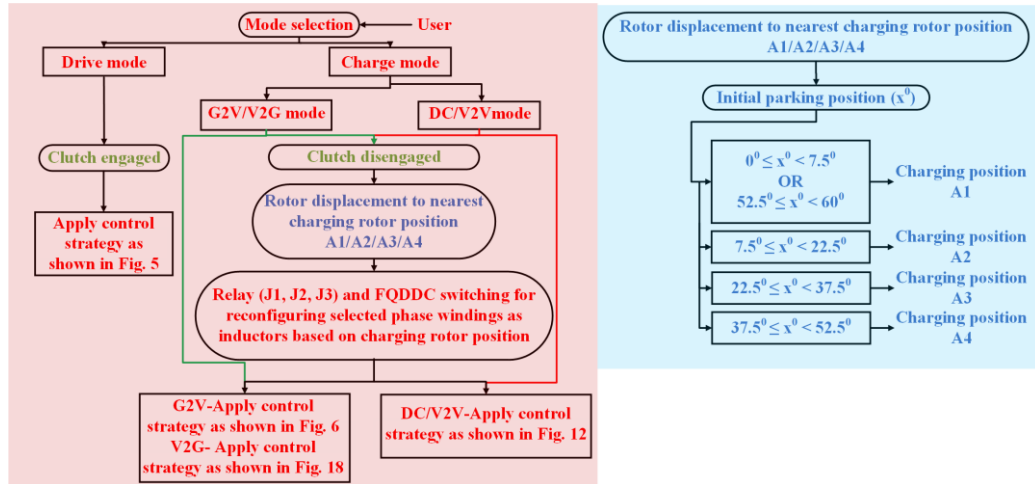


Fig. 5. 27. Flowchart diagram.

5. 7. Conclusion

The paper presents an IC with integrated G2V, V2G, and DC/V2V charging capabilities for SRM drive-train-based EV applications. The proposed IC does not require any additional non-integrated power electronics component/s and/or inductor/s for its operation.

During G2V/V2G mode, the AC grid terminals are directly connected to the winding nodes. Moreover, the reconfigured bidirectional G2V/V2G charger allows BESS charging/ discharging via an AC grid of any voltage rating. For DC/V2V charging, the DC-link of the proposed IC can be connected to a DC source/load of any voltage rating as the integrated DC charger is capable of operating in all four quadrants. Also, the proposed IC connects the solar PV system to the BESS via integrated FQDDC, eliminating the requirement of an external DC-DC converter. The inductors required for the integrated BB-PFC/VSI and FQDDC are reconfigured from the phase windings of the SRM. Moreover, the charging current flowing in the reconfigured phase windings results in net ZCT production at appropriate rotor positions.

The stated claims of the proposed IC are validated experimentally.

CHAPTER 6

A UNIVERSAL-INPUT INTEGRATED POWER CONVERTER FOR 4-PHASE SWITCHED RELUCTANCE MOTOR DRIVE BASED EV APPLICATION

Since asymmetric half-bridge (AHB) converter is widely accepted and used by the industry for SRM drive-train, this chapter proposes a novel IC for EV application based on 4-phase SRM drive which can be further extended to n -phase configuration. While driving, the proposed IC configuration is similar to a conventional AHB converter for n -phase for SRM drive. However, during battery charging mode, the proposed IC is utilized as an integrated OBC by reconfiguring it into an $(n-2, n-3, \dots, 1)$ phase interleaved buck cascaded buck-boost (IBuCBB) converter. The $(n-2, n-3, \dots, 1)$ charging inductors for the IBuCBB configuration are realized via the phase windings of the SRM. Thus, the proposed IC eliminates the requirement of an additional circuit for battery charging. The integrated OBC facilitates battery charging via a single-phase residential/public outlet, i.e., AC level-1 and AC level-2 charging, over a universally available input voltage range, i.e., 85-265 V rms (root mean square), with acceptable performance and efficiency. In addition, the proposed IC for n -phase SRM drives employs same number of power electronic switches as in the conventional AHB converter for n -phase SRM drive. Detailed theoretical analysis and experimental verification on a 4-phase SRM prototype are presented to evaluate the proposed IC's driving and on-board battery charging features.

6.1. LITERATURE REVIEW FOR UNIVERSAL CHARGER

Conventionally the boost PFC configuration is widely adopted for on-board chargers [58]. However, it suffers from charging inductor oversizing and high conduction losses when operated at lower line voltages (85-120 V rms), resulting in lower charging efficiency [58]. Also, employing boost PFC requires the BESS voltage to be slightly greater than the peak value of the input AC voltage. Thus, a step-down DC-DC converter is cascaded with the boost PFC to extend the output DC range, as implemented and discussed in chapter-3, chapter-4 and chapter-5.

The cascade connection facilitates BESS charging with voltages lower than the peak value of the input AC voltage [59]. However, the cascade connection results in reduced charging efficiency. Thus, for the employed PFC to be operational over the universal input voltage range and to have the charging capability over a wide range of BESS voltages, it must operate simultaneously in buck and boost modes.

In this regard, single-switch inverting buck-boost, SEPIC and Cuk PFC converters are employed for on-board chargers [60]. However, single-switch buck-boost converters increase the component stresses and the energy storage element requirement. This is because, for the above-mentioned buck-boost converters, the input and output are not directly connected for any switching instant. The input AC power is first stored in the energy storage element/s and then transferred to the output, resulting in reduced charging efficiency compared with boost PFC [61]. And thus, they are not suitable for EV applications where high-power BESS charging with high efficiency and lesser space occupancy are major constraints.

To mitigate the shortcoming associated with single-switch buck-boost PFCs, and for high power BESS charging, two-switch buck-boost PFCs, i.e., buck-cascaded buck-boost (BuCBB) and boost cascade buck-boost (BoCBB) configurations are developed [61].

Further, the BuCBB configuration has an advantage over the BoCBB configuration in terms of inductor utilization and the associated conduction loss as the latter uses two charging inductors. However, BuCBB advantages are partially offset due to higher conduction losses associated with the input switch, when BuCBB majorly operates in boost mode.

In addition, the BuCBB configuration mandatory requires a large input filter to meet the line current harmonics standards. Thus, for incorporating the advantages of BuCBB and BoCBB, in the further development stage, boost interleaved buck-boost (BoIBB) and interleaved BuCBB (IBuCBB) are developed [61], [62].

The BoIBB configuration still requires two charging inductors as in BoCBB configuration but mitigates the higher inductor conduction losses associated with BoCBB. However, the BuCBB configuration still has the least charging inductor conduction losses compared with BoCBB and IBuCBB configurations [61]. In addition, the BuCBB configuration only requires one charging inductor for implementation, which makes it economical and most favorable configuration for on-board chargers with the universal-input operation. The only shortcoming associated with BuCBB configuration is the higher conduction loss associated with the input switch when BuCBB majorly operates in boost mode. In this regard, though IBuCBB increases the switch count but it achieves high charging efficiency and eliminates higher conduction losses associated with the input switch of the BuCBB configuration. IBuCBB also minimizes/eliminates the requirement of an input filter (for a specific range of DC outputs) [62]. Thus, IBuCBB and BuCBB are the most promising PFC configurations for universal-input operation and for charging a wide range of BESS outputs [62], [63]. Hence, they are still researched and developed for EV applications.

Thus chapter-6 of the thesis investigates a way to integrate a universal charger for 4-phase SRM drive which can be further extended for n-phase SRM.

6.2. OPERATIONAL MODES OF THE PROPOSED IC

If the proposed IC configuration is extended for n-phase SRM its configuration is shown in **Fig. 6. 1**. For implementation, 4-phase SRM drive is considered, i.e., $n=4$. Thus the 4-phase configuration of the proposed IC for driving is shown in **Fig. 6. 2. (a)**.

During driving mode, relay J1 is closed, and the proposed IC is reconfigured as a conventional AHB converter for 4-phase SRM, as shown in **Fig. 6. 2. (a)**. Node-A, Node-B, and Node-C, as shown in **Fig. 6.2. (a)**, are connected to the positive DC bus of the conventional AHB converter by closing relay J1. The adopted control scheme for controlling the proposed IC while driving is shown in **Fig. 6.2. (b)**.

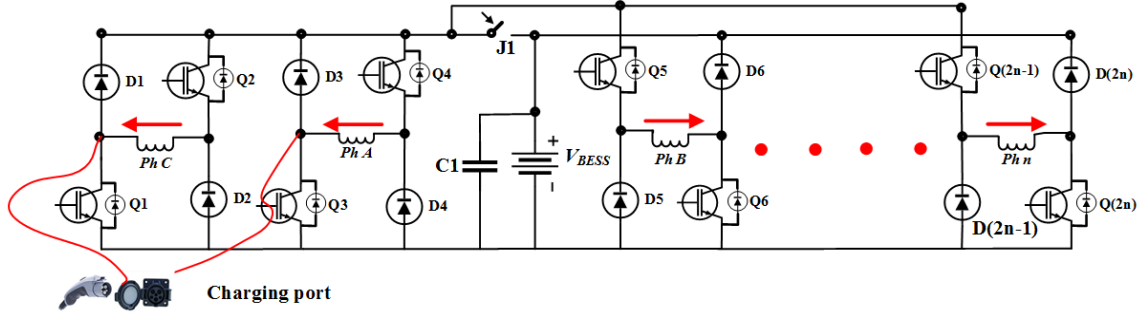


Fig. 6. 1. Proposed IC configuration for n-phase SRM drive.

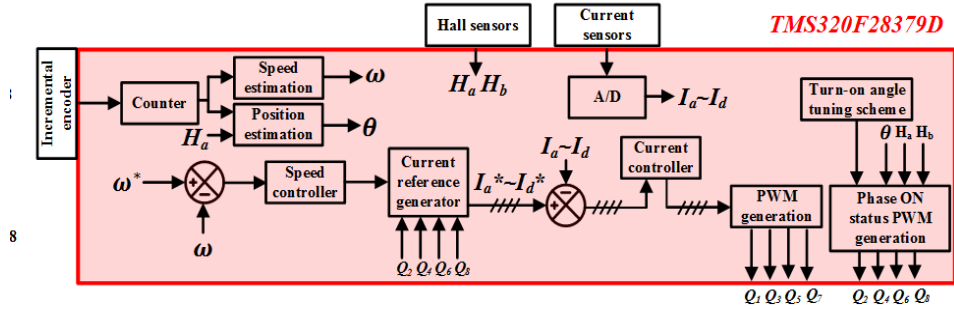
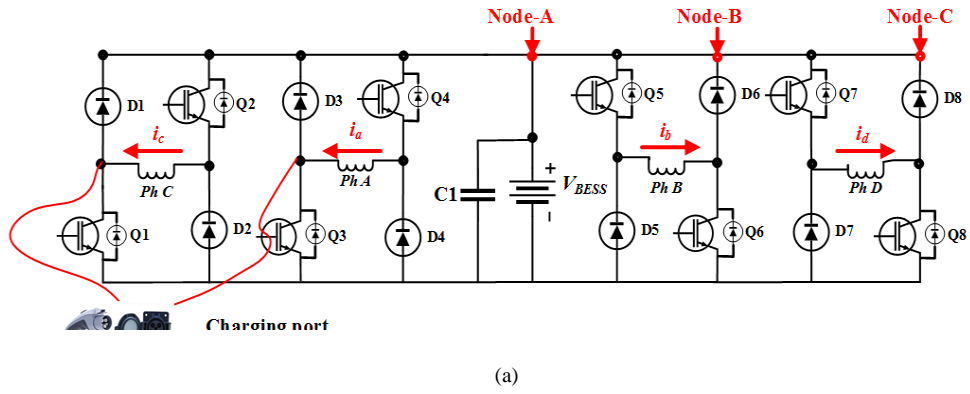


Fig. 6. 2. (a) Proposed IC configuration for 4-phase SRM drive. (For driving mode, relay J1 is closed). (b) Adopted control scheme while driving.

6. 2. 1. BATTERY CHARGING MODE: CONFIGURATION

For operation during battery charging mode, relay J1 is opened, and the proposed IC is utilized as a universal input on-board charger based on (n-2, n-3..., 1) phase IBuCBB converter configuration. For design and implementation, 4-phase configuration of the proposed IC is considered. Thus, the proposed IC can be reconfigured as a two-phase IBuCBB or a single-phase BuCBB configuration, as shown in **Fig. 6. 3**.

The connecting terminals of the single-phase AC supply within the IC are shown in **Fig. 6. 1** and **Fig. 6. 2**. Diodes D1, D3 and the diodes of switches Q1, Q3 forms the single-phase diode bridge rectifier configuration, as shown in Fig. 3. Switches Q5, Q7 and diodes D5, D7 forms the two-phase interleaved buck unit followed by a two-phase interleaved boost unit formed by diodes D6, D8 and switches Q6, Q8. The two-phase interleaved buck and boost units are connected via the two-phase windings of SRM, i.e., phase-B and phase-D windings, reconfigured as charging inductors. The resulting two-phase IBuCBB configuration is shown in **Fig. 6. 3**.

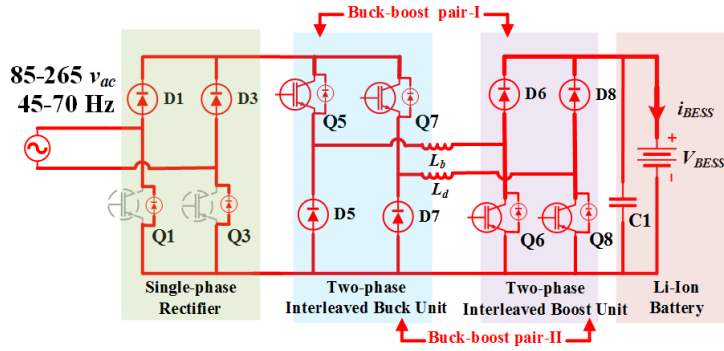


Fig. 6. 3. Proposed IC configuration during battery charging mode (J1-open).

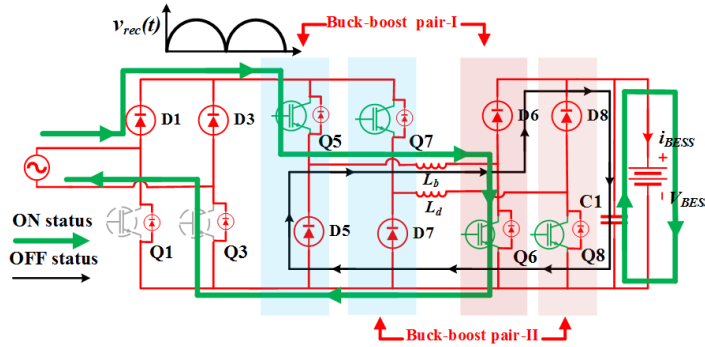


Fig. 6. 4. Synchronous switching/cascade buck-boost operation of the two-phase IBuCBB or single-phase BuCBB configuration.

The power electronics switches and the inductor required for the realization of the two phase IBuCBB configuration are derived from the proposed IC and the SRM windings respectively. Thus, as discussed in the earlier, the shortcomings associated with IBuCBB configuration in terms of higher switch requirement and extra inductor/s is not a constraint with the proposed IC configuration.

The two-phase IBuCBB configuration can also be utilized as a single-phase BuCBB configuration by using any one buck-boost pair from the two-phase IBuCBB configuration.

Meanwhile, the other buck-boost pair switches are kept in an OFF state. The first buck-boost pair is formed by utilizing switch Q5, diode D5 from the two-phase interleaved buck unit along with diode D6, switch Q6 from the two-phase interleaved boost unit connected via phase-B winding. The second buck-boost pair is formed by utilizing switch Q7, diode D7 from the two-phase interleaved buck unit along with diode D8, switch Q8 from the two-phase interleaved boost unit connected via phase-D winding, as shown in **Fig. 6.3**.

The DC-link capacitor C1 across the BESS facilitates a constant current charging of BESS with reduced current ripple. In addition, when the proposed IC is reconfigured as a two-phase IBuCBB, no additional off-board circuit/passive element is required to realize it. Also, no additional diode/ switch falls in the line current path of the two-phase IBuCBB/ BuCBB configuration, which does not result in any additional conduction loss during charging.

6.2.2. BATTERY CHARGING MODE: OPERATION

The basic operational principle of the integrated on-board charger is shown in **Fig. 6. 4**. The switches of the two-phase interleaved buck unit (i.e., Q5, Q7) and two-phase interleaved boost unit (i.e., Q6, Q8) execute step-

up and step-down operation simultaneously when operated in synchronous switching/cascade buck-boost mode. As shown in **Fig. 6. 4**, when switches Q5, Q7 and Q6, Q8 are switched ON, the input power is utilized in charging the inductors L_b and L_d (connected in parallel). Furthermore, when switches Q5, Q7 and Q6, Q8 are switched OFF, the stored inductor energy is transferred to the output/load.

Also, from **Fig. 6. 4** it can be inferred that the input AC current of the two-phase IBuCBB configuration or the BuCBB configuration, when operated in cascade buck-boost mode, is discontinuous due to the switching in the buck unit. Thus, a large input filter is required for meeting the line current harmonics standard.

However, the advantage of the two-phase IBuCBB configuration is that the input filter requirement can be minimized/eliminated by operating the two buck-boost pairs via 180° phase-shifted PWM signals. In other words, when the switches of the buck-boost pair-I are in ON-status, the switches of the buck-boost pair-II are in OFF-status and vice-versa.

The voltage gains of the BuCBB or two-phase IBuCBB configuration is similar to the conventional buck-boost converter, i.e.,

$$\frac{V_{BESS}}{v_{rec}} = \frac{D}{1-D}, \quad (6.1)$$

where V_{BESS} is the BESS voltage, v_{rec} is the input rectified voltage applied to the two-phase interleaved buck unit. And D denoted the duty cycle of the two-phase IBuCBB configuration. Thus, depending upon the peak value of the rectified input AC voltage and the BESS voltage, the duty cycle of the IBuCBB is calculated. And depending upon the duty cycle, the IBuCBB either boost or buck the output voltage with respect to the input voltage.

When the instantaneous value of the rectified input AC voltage is lesser than the BESS voltage, the IBuCBB boost the output voltage with respect to the input voltage. Moreover, the individual duty cycle of the 180° phase-shifted buck-boost pairs of the two-phase IBuCBB is greater than or equals 0.5. In this case, the input AC current is continuous and is shared among the buck-boost pairs of the two-phase IBuCBB, as shown in **Fig. 6. 5. (a)**. When the instantaneous value of the input AC voltage is greater than the BESS voltage, the IBuCBB buck the output voltage with respect to the input voltage. Moreover, the individual duty cycle of the 180° phase-shifted buck-boost pairs of the two-phase IBuCBB is less than 0.5. In this case, the input AC current is discontinuous and flows only through any one of the buck-boost pairs, as shown in **Fig. 6. 5. (b)**. Thus, when the buck-boost pairs of the two-phase IBuCBB operate in 180° phase shifts from each other with a duty cycle greater than 0.5, the filter requirement can be minimized. The adopted control for cascade buck-boost mode of operation is shown in **Fig. 6. 5. (c)**. **Fig. 6. 5. (c)** shows that depending upon the outer voltage (G_{vl}) or current loop (G_{cl}) adopted the BESS can be charged in CC or CV mode respectively. **Fig. 6. 5. (d)** shows the individual duty ratio of the buck and boost units during operation.

Also, when buck-boost cascade mode is employed for simultaneous step-up and step-down operation, there is no direct path from input to output, resulting in reduced efficiency and increased component stresses.

Hence, employing buck-boost cascade mode for the complete input-output voltage range is not practically adopted. The cascade buck-boost mode is only advantageous to be applied when the input and output voltages overlap.

For improving the charging efficiency, the additional operating modes of the two-phase IBuCBB, i.e., boost and buck modes, are applied with respect to the instantaneous value of the rectified AC voltage and the BESS voltage. The boost and buck modes provide a direct path/connection of the input and the output, resulting in higher charging efficiencies.

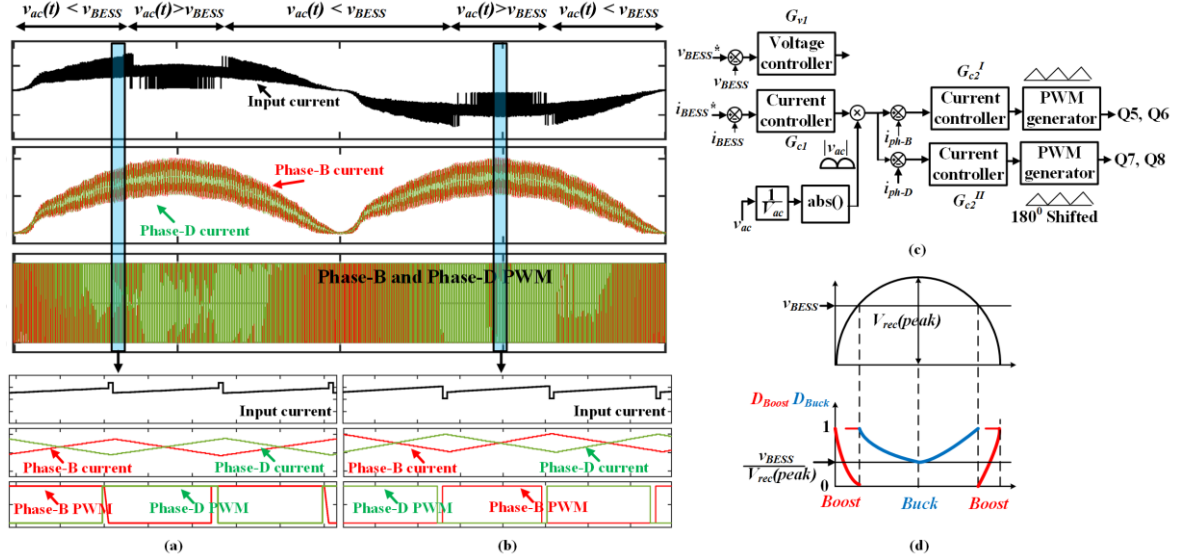


Fig. 6. 5. Input AC current, and phase-B and phase-D currents when two 180° phase shifted buck-boost pairs operate with (a) $D \geq 0.5$, and (b) $D < 0.5$. (Simulated result). (c) Control scheme for cascade buck-boost mode of operation. (d) Duty ratio during buck and boost operation.

6.2.3. BATTERY CHARGING MODE: MODE SELECTION

Depending upon the input and output conditions, the IBuCBB operates in three modes, i.e., boost mode, buck mode and cascade buck-boost mode, which is already discussed above. When the instantaneous value of the input AC voltage is lesser than the output BESS voltage, the IBuCBB operates in boost mode, as shown in **Fig. 6. 6**. During boost operation, the IBuCBB operates similar to conventional boost PFC converter. For achieving boost type PFC characteristics, the switches in the interleaved buck unit, i.e., Q5 and Q7, are always kept in an ON state, and the switches of the interleaved boost unit, i.e., Q6 and Q8, are controlled via PWM signals. When Q6 and Q8 are switched ON, the input AC power charges the charging inductor $L_b \parallel L_d$. And when Q6 and Q8 are switched OFF, a direct path from input to output is created via the charged charging inductors $L_b \parallel L_d$, as shown in **Fig. 6. 6**.

Similarly, when the instantaneous value of the input AC voltage is greater than the output BESS voltage, the IBuCBB operates in buck mode, as shown in **Fig. 6. 7**. During buck mode operation, the IBuCBB operates similar to a conventional buck converter. For achieving buck type PFC characteristics, the switches in the interleaved boost unit, i.e., Q6 and Q8, are always kept in an OFF state, and the switches of the interleaved buck unit, i.e., Q5 and Q7, are controlled via PWM signals. When Q5 and Q7 are switched ON, a direct path from input to output is created via charging inductors $L_b \parallel L_d$, as shown in **Fig. 6. 7**. And when Q5 and Q7 are switched OFF, the charging inductors $L_b \parallel L_d$ discharges to the load.

As inferred from **Fig. 6. 7**, the input AC current is discontinuous during buck-mode of operation. Thus, a large input filter is required to make the input AC current continuous and meet the line current harmonics standards.

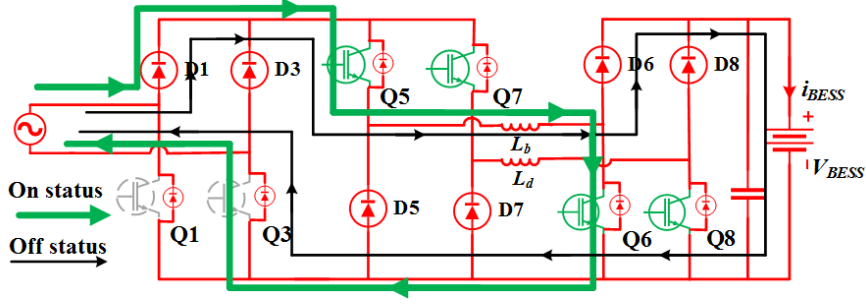


Fig. 6. 6. Proposed IC during battery charging mode, when operating in boost mode.

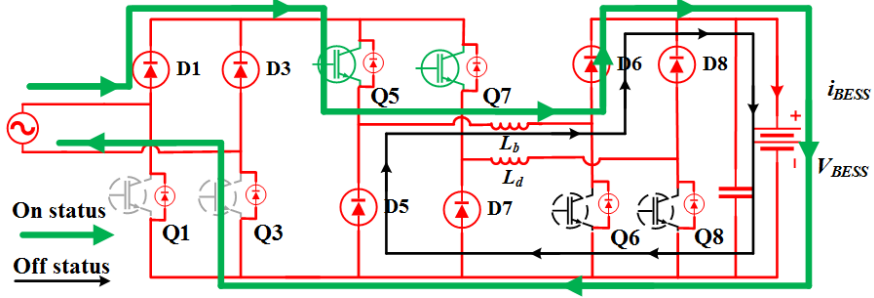


Fig. 6. 7. Proposed IC during battery charging mode, when operating in buck mode.

When the BESS voltage is lesser than the peak value of the rectified input AC voltage, the IBuCBB changes its mode of operation from boost mode to buck mode and vice-versa. The mode change is performed whenever the input and output voltages overlap. And since the rectified input AC voltage is a periodic waveform, the mode change/transition is performed twice in each half-cycle, as shown in **Fig. 6. 8. (a)**.

The mode change/transition involves a non-linear transfer function which results in transients in the input AC current, as discussed in [64]. Thus, the buck-boost cascade mode is inserted between the boost and buck modes for reducing the input AC current transients [64] and [65].

Fig. 6. 8. (a) shows the operating mode of the IBuCBB with respect to the input and output voltages. As shown in **Fig. 6. 8. (a)**, when BESS voltage is lesser than the peak value of input rectified AC voltage, the IBuCBB twice changes the mode of operation, i.e., from boost to buck and then again from buck to boost. The buck-boost mode is inserted during the IBuCBB transition for reducing the transients in the AC current.

Fig. 6. 8. (b) shows the IBuCBB operating mode when the BESS voltage is greater than the peak value of the input AC voltage. For BESS voltages greater than the peak value of the input AC voltage IBuCBB only operates in the boost mode. Moreover, when the BESS voltage range overlaps with the peak value of the input AC voltage, the IBuCBB only operates in buck-boost cascade mode. However, as discussed above, the buck-boost cascade mode leads to reduced charging efficiency. And thus, the range of BESS voltages that need to be charged via buck-boost cascade is decided based on performance and efficiency consideration.

Also, as discussed, the buck-mode requires a large input filter for implementation. Thus, considering the compactness of the proposed IC as a priority, the buck-mode is replaced via cascade buck-boost mode for simulation and hardware verification.

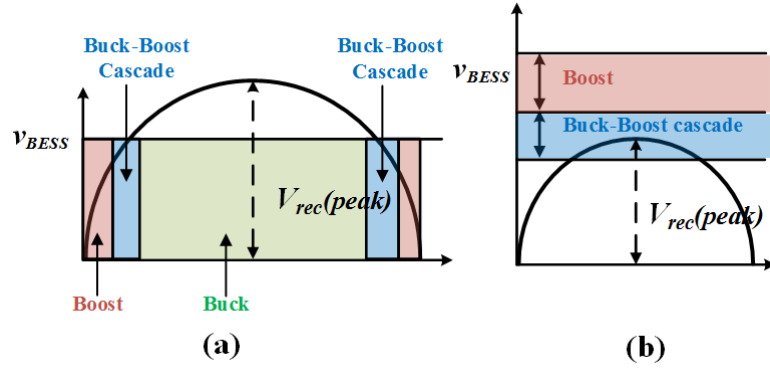


Fig. 6. 8. Mode selection based on input-output condition.

6. 3. TORQUE PRODUCTION VIA CHARGING CURRENT IN PHASE WINDING/S

The proposed IC reconfigures/reutilizes the phase windings as two-phase charging inductors for the two-phase IBuCBB configuration. Thus, the charging current in the phase windings leads to torque production. Hence an analysis of the resultant torque produced is carried out in this section.

For SRM drive, the torque produced due to the current flowing in the phase winding depends on the phase current and corresponding slope of inductance with respect to the rotor position, i.e., $\partial L/\partial \theta$. Thus, when the phase is excited at the rotor position/s where $\partial L/\partial \theta > 0$, it results in positive torque production. And when the phase is excited at the rotor position/s where $\partial L/\partial \theta < 0$, it results in negative torque production.

The actual inductance profile of the employed 4-phase SRM is shown in **Fig. 6. 9**. The inductance profile shows that charging at rotor position-A and rotor position-B results in equal and opposite torque for phase-B and phase-D windings if excited with equal currents. Thus, the rotor is displaced to any marked rotor positions during battery charging mode, i.e., either at rotor position-A or rotor position-B.

The IBuCBB configuration operates in either boost or cascade buck-boost mode. During boost-mode of operation, the two buck-boost pairs are switched in synchronism. In other words, the phase-B and phase-D windings currents are regulated via similar PWM signals. Thus, resulting in equal currents in the two-phase windings, as shown in **Fig. 6. 10**. Also, due to equal currents in the two-phase windings, the resultant torque when charging at rotor position-A or rotor position-B is zero, as shown in **Fig. 6. 10**.

But during cascade buck-boost mode of operation, the two buck-boost pairs are switched with 180° phase-shifted PWM signals. Thus, the current in the phase windings is not equal. The unequal currents in two-phase windings result in a net torque production when charging at rotor position-A or rotor position-B, as shown in **Fig. 6. 11**.

However, the nature of instantaneous torque produced due to current in phase-B and phase-D is opposite, which results in cancelling the torque of the two-phase windings, as shown in **Fig. 6. 11**. Thus, the magnitude of resultant instantaneous torque generated is very less. Also, for consecutive switching cycles (i.e., one complete switching cycle), the average torque due to the charging current in phase-B and phase-D is zero, as shown in **Fig. 6. 11**.

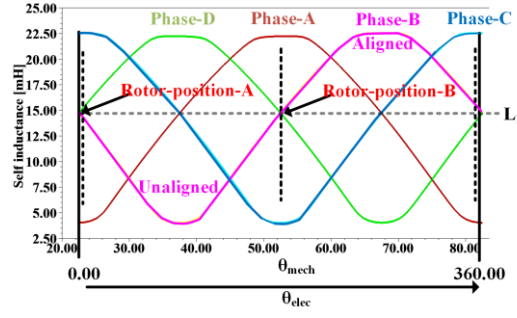


Fig. 6. 9. Selected rotor position for battery charging mode.

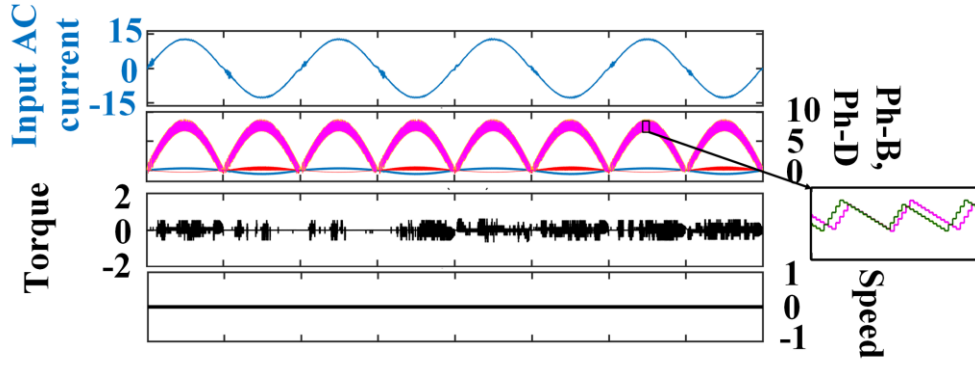


Fig. 6. 10. Torque produced via charging currents when operating in boost mode (Simulated result- ($V_{ac} = 230$ V rms, $V_{BESS} = 400$ V, $i_{BESS} = 5$ A)).

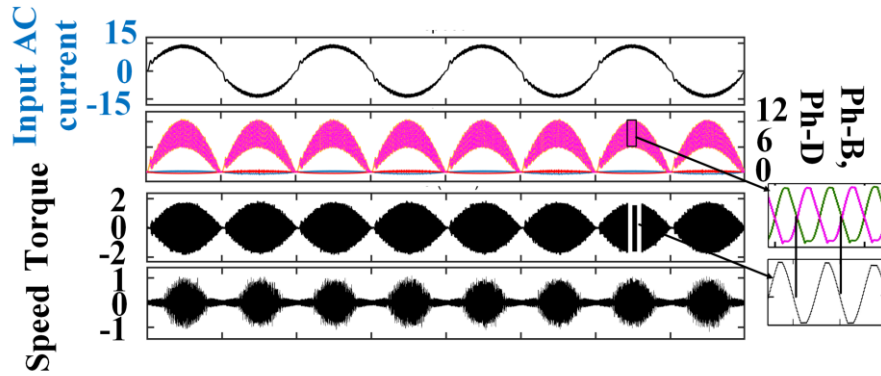


Fig. 6. 11. Torque produced via charging currents when operating in cascade buck-boost mode ($V_{ac} = 230$ V rms, $V_{BESS} = 400$ V, $i_{BESS} = 5$ A))

6. 4. EXPERIMENTAL VALIDATION AND DISCUSSION

For validating the proposed IC, a laboratory prototype is developed with eight SKM75GB12T4 IGBT switches and tested on a 4-phase SRM (2.2 kW). The hardware setup is shown in **Fig. 6. 12**. The battery functionality is emulated via ITECH-6012B. The 4-phase SRM is rated 120 V, and hence the nominal battery voltage (V_{BESS}) during driving charging mode is maintained at 120 V.

During battery charging mode for demonstrating universal-input operation the AC voltage is set to 120 V rms and 230 V rms via an external autotransformer. The commercial EVs BESS is rated from 230 V to 450 V, thus for demonstrating the wide range of BESS voltage charging capability of the integrated on-board charger, the BESS voltage is set to 230 V and 400 V.

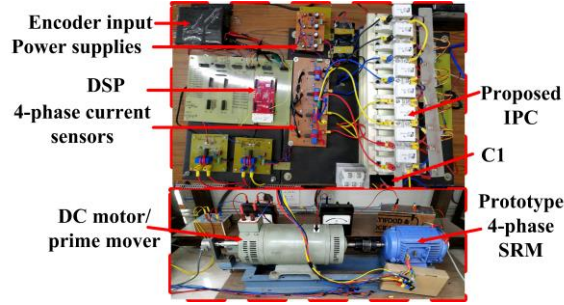


Fig. 6. 12. Experimental setup.

6. 4. 1. Battery charging mode

During battery charging mode, relay J1 is opened and the proposed IC is reconfigured as a two-phase IBuCBB or as a single-phase BuCBB configuration, as shown in **Fig. 6. 3**. Depending upon the input-output condition. the two-phase IBuCBB configuration operates either in boost, or cascade buck-boost mode, as shown in **Fig. 6. 8**. During cascade buck-boost mode, the buck-boost pairs operate with 180° phase shifted PWM signals. An EMI filter is employed after the AC supply to reduce the switching noises generated.

Fig. 6. 13 shows the universal-input operation of the two-phase IBuCBB configuration. **Fig. 6. 13. (a)** and **Fig. 6. 13. (c)** shows the input AC voltage and current when the input voltage is 120 V rms and 230 V rms respectively, and the output BESS voltage is 400 V. Here the IBuCBB operates in boost mode as the BESS voltage is greater than the peak value of the input AC voltage.

Fig. 6. 13. (b) and **Fig. 6. 13. (d)** shows the input AC voltage and current when the input voltage is 230 V rms, and the output BESS voltage is 230 V and 400 V, respectively. Here the IBuCBB operates in cascade buck-boost mode as the BESS voltage of 230 V is smaller than the peak value of the input AC voltage. Moreover, the BESS voltage of 400 V is greater than the peak value of the input AC voltage. Thus, IBuCBB is operated in cascade buck-boost mode to demonstrate simultaneously step-up and step-down characteristics.

For the results shown in **Fig. 6. 13** the BESS is charged in constant current (CC) mode with BESS charging power of approximately 1.8 kW - 2 kW, demonstrating *AC level-1 charging*.

For the input AC voltage of 230 V rms and the output BESS voltage of 400 V, as shown in **Fig. 6. 13. (c)** and **Fig. 6. 13. (d)**, the IBuCBB is operated in boost and cascade buck-boost mode, respectively. The only difference is in terms of charging efficiencies, which is discussed in the subsection following.

Fig. 6. 14 shows the phase-B and phase-D currents during BESS charging, when the IBuCBB operates in boost mode. As discussed, during boost mode, equal currents flow in phase-B and phase-D windings resulting in zero-torque production. During cascade buck-boost mode, the buck-boost pairs are switched with 180° phase-shifted PWM, resulting in torque production. However, the average torque produced is zero for a switching cycle, as discussed. **Fig. 6. 15** shows the phase-B and phase-D currents when the IBuCBB operates in cascade buck-

boost mode. From **Fig. 6. 14** and **Fig. 6. 15** it is seen that the rotor is stationary at rotor position-A during boost and cascade buck-boost mode of operation.

6. 4. 2. Charging efficiency plots

For evaluating the integrated on-board charger performance efficiency plots are provided for the operating voltage spectrum of input and output. The obtained efficiency verses BESS charging power plots are shown in **Fig. 6. 16** and **Fig. 6. 17**.

According to the obtained efficiency plots during boost mode of operation, the charging efficiency improves when BESS charging power increases. In other words, the charging efficiency is improved at full load condition. Also, at higher BESS voltage i.e., 400 V, the ON duty cycle of switches in boost mode increases which reduces the charging efficiency, as shown in **Fig. 6. 16**.

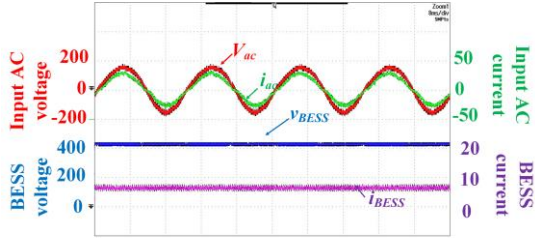
The charging efficiency during cascade buck-boost mode is lesser than the boost mode. The reasons for which are already stated and shown in **Fig. 6. 17**. The input power factor of the integrated on-board charger is greater than 0. 97.

6. 5. CONCLUSION

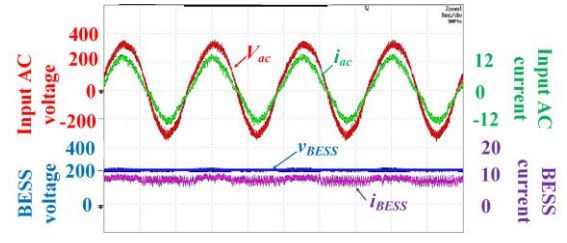
The design and implementation of a novel IC for n-phase SRM drive based EV application has been presented, in accordance to 4-phase SRM. During driving mode, the CCC response of the proposed IC when reconfigured as conventional AHB converter has been validated via experimental results.

During battery charging mode, the proposed IC has been reconfigured as a universal-input on-board charger which is based on two-phase IBuCBB or single-phase BuCBB configuration. The power electronic switches and the charging inductors required for realizing the IBuCBB\BuCBB are derived from the proposed IC itself. Thus, no additional off-board circuit is required for realizing the integrated on-board charger. Depending upon input-output condition, three operating modes i.e., boost, buck and cascade buck-boost are discussed for the IBuCBB configuration. The universal-input operation of the integrated on-board charger has been validated by experimental studies with different levels of input and output voltages.

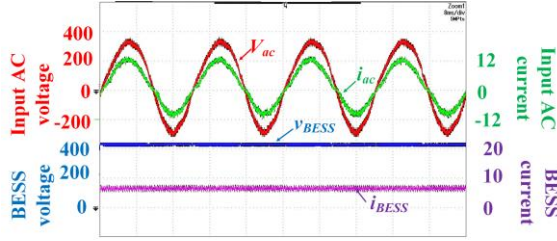
Also, the charging currents flowing in the phase winding's, when reconfigured as charging inductor's results in a zero-torque production. The zero-torque production has been experimentally validated by performing BESS charging at two selected rotor positions.



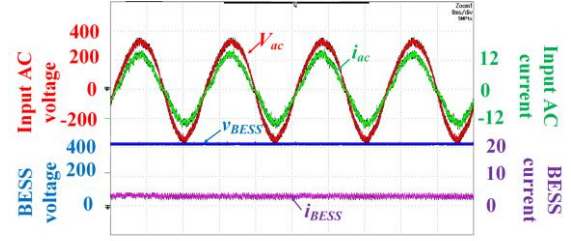
(a)



(b)



(c)



(d)

Fig. 7. 13. Input AC voltage, current and BESS voltage, current when operating at (a) $V_{ac} = 120$ V rms, $V_{BESS} = 400$ V (boost mode), (b) $V_{ac} = 230$ V rms, $V_{BESS} = 230$ V (cascade buck-boost mode), (c) $V_{ac} = 230$ V rms, $V_{BESS} = 400$ V (boost mode), and (d) $V_{ac} = 230$ V rms, $V_{BESS} = 400$ V (cascade buck-boost mode)

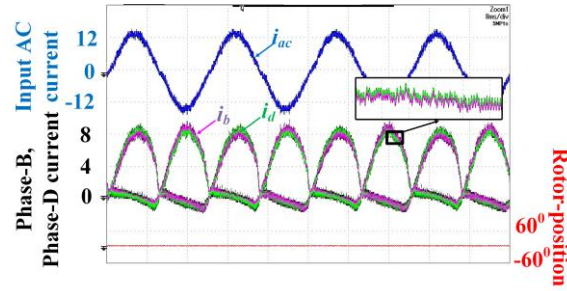


Fig. 6. 14. Torque produced via charging currents when operating in boost mode at rotor position-A ($V_{ac} = 230$ V rms, $V_{BESS} = 400$ V, $i_{BESS} = 5$ A).

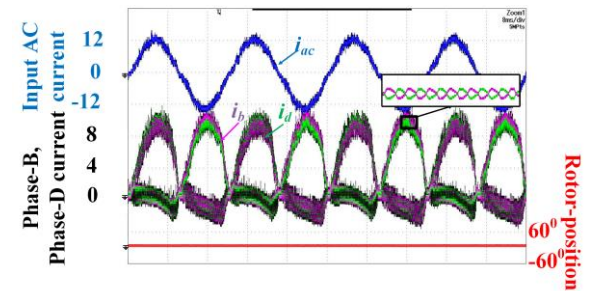


Fig. 6. 15. Torque produced via charging currents when operating in cascade buck-boost mode ($V_{ac} = 230$ V rms, $V_{BESS} = 400$ V, $i_{BESS} = 5$ A).

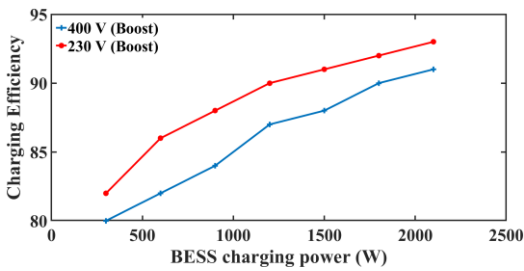


Fig. 6. 16. Efficiency plot vs BESS charging power for $V_{ac} = 120$ V rms.

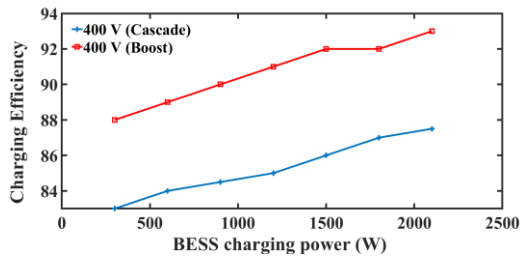


Fig. 6. 17. Efficiency plot vs BESS charging power for $V_{ac} = 230$ V rms.

CONCLUSION AND FUTURE SCOPE

CONCLUSION

The thesis firstly in chapter-2 proposes a DTC scheme for 4-phase SRM, where simultaneously, two adjacent phases were excited to extend the smooth torque operating region to the base speed. Two DTC schemes, i.e., DTC-I and DTC-II, were proposed. DTC-I operates till 70% of the base speed, and DTC-II operates above 70% of the base speed. The maximum torque ripple with DTC-I is 30% of the nominal torque till 70% of the base speed. Thereafter the controller switches to DTC-II, where the maximum torque ripple is 50% of the nominal torque at the base speed.

Now since with the advancement in control techniques and MLCTs, SRM-based drive-trains are extensively researched and developed for electric vehicle (EV) applications. Thus, the thesis further investigates/ propose integrated converter/s that integrating driving and charging modes, eliminating the requirement of separate OBC module.

Chapter-3 proposed a fully IC with charging and driving capabilities for EV application incorporating 4-phase SRM. With the proposed IC, eight novel rotor positions are proposed at which ZCT is achieved. Thus, for reaching the nearest rotor position for charging, the maximum displacement is reduced to 7.5^0 mechanical, which any other IC does not achieve for SRM drive. Also, the magnetic field density at the proposed charging rotor is not that considerable, which verified using FEA analysis. The ZCT at the proposed rotor positions is verified by observing the total charging torque at the specified rotor positions via simulation and experimental studies. However, with the proposed IC in chapter-3 for the driving mode, the torque-speed curve is limited as the IC is capable of applying three-levels of voltages only.

Chapter-4 proposes a fully IML-PCT with driving and battery charging capabilities for SRM drive-based EV application. During driving mode, the proposed IML-PCT applies higher phase voltages leading to faster energization and de-energization of the phase current/s. It resulted in an enhanced constant torque and power region for SRM drive. During battery charging mode, the proposed IML-PCT was utilized as an OBC, which is realized using an IBB-PFCC. The IBB-PFCC cascade with a BDDC facilitates battery charging in CC/CV modes directly via an AC outlet. All the benefits achieved with the IC proposed in chapter-3 are also achieved with the IC proposed in chapter-4. However fast DC/V2V charger is not integrated with the IC proposed in chapter-3 and chapter-4.

Chapter-5 proposes an IC with integrated G2V, V2G, and DC/V2V charging capabilities for SRM drive-train-based EV applications. The proposed IC does not require any additional non-integrated power electronics component/s and/or inductor/s for its operation. During G2V/V2G mode, the AC grid terminals are directly connected to the winding nodes. Moreover, the reconfigured bidirectional G2V/V2G charger allows BESS charging/ discharging via an AC grid of any voltage rating. For DC/V2V charging, the DC-link of the proposed IC can be connected to a DC source/load of any voltage rating as the integrated DC charger is capable of operating in all four quadrants. Also, the charging current flowing in the reconfigured phase windings results in net ZCT production at appropriate rotor positions. All the claims of the thesis are supported via simulation and experimental studies. However, the IC discussed/ proposed in objective-2, objective-3 and objective-4 integrates a cascade/ two stage battery charging topology for the charging mode which results in reduced charging efficiency.

Chapter-6 proposed an IC which during battery charging mode, has been reconfigured as a universal-input on-board charger which is based on two-phase IBuCBB or single-phase BuCBB configuration. No additional off-board circuit is required for realizing the integrated on-board charger. Depending upon input-output condition, three operating modes i.e., boost, buck and cascade buck-boost are discussed for the IBuCBB configuration. The universal-input operation of the integrated on-board charger has been validated by experimental studies with different levels of input and output voltages. Also, the charging currents flowing in the phase winding/s, when reconfigured as charging inductor/s results in a zero-torque production. The zero-torque production has been experimentally validated by performing BESS charging at two selected rotor positions.

FUTURE SCOPE

The thesis proposes different ICs configuration for SRM drive-train that aims to reconfigure the electric drive-train power electronics and traction motor phase winding/s for integrating propulsion and on-board battery-charging functionality.

The first future scope of the work is to validate the performance and effectiveness of the IC proposed in chapter-6 for N-phase SRM (i.e., for 3-phase and 5-phase).

The second future scope of the work is to integrate a three-phase level-3 fast charger with the IC. As the ICs proposed in chapter-5 and chapter-6 integrates slow single-phase charging and for faster charging of battery, the thesis also proposes an IC with integrated DC/V2V charger. However, the availability of DC power for EV charging is limited.

Thus, for faster charging a three-phase level-3 charger must be integrated with the IC. The electric drive-train components are rated to drive the high-power traction motor, thus ICs can support level-3 fast charging, if integrated. Presently Renault ZOE integrates a three-phase charger capable of charging the battery pack in less than 0.5 hours with a maximum power of 43kW. However, a non-integrated component is required for performing rectification. In the existing literature the ICs for conventional AC drives integrating fast three-phase AC level-3 chargers without non-integrated components suffer from torque production during charging. The torque is produced due to the rotating magnetic field developed via the charging currents in all three reconfigured phase windings. In this regard, switched reluctance motors do not require an RMF for torque production due to their isolated phase winding configuration. Thus, integrating a three-phase charger with IC for SRM drive is the future scope of this work.

REFERENCES/BIBLIOGRAPHY

- [1] I. Husain, "Minimisation of torque ripple in SRM drives," in *IEEE Trans. Ind. Electron.*, vol. 49, no. 1, pp. 28-39, Feb. 2002.
- [2] X. D. Xue, K. W. E. Cheng and S. L. Ho, "Optimization and Evaluation of Torque-Sharing Functions for Torque Ripple Minimization in Switched Reluctance Motor Drives," in *IEEE Transactions on Power Electronics*, vol. 24, no. 9, pp. 2076-2090, Sept. 2009.
- [3] Y. Z. Xu, R. Zhong, L. Chen and S. L. Lu, "Analytical method to optimize turn-on angle and turn-off angle for switched reluctance motor drives," in *IET Electric Power Applications*, vol. 6, no. 9, pp. 593-603, November 2012.
- [4] R. B. Inderka and R. W. A. A. De Doncker, "DITC-direct instantaneous torque control of switched reluctance drives," in *IEEE Transactions on Industry Applications*, vol. 39, no. 4, pp. 1046-1051, July-Aug. 2003.
- [5] I. Kioskeridis and C. Mademlis, "Maximum efficiency in single-pulse controlled switched reluctance motor drives," in *IEEE Transactions on Energy Conversion*, vol. 20, DOI: 10.1109/TEC.2005.853738, no. 4, pp. 809-817, Dec. 2005.
- [6] A. A. Abdel-Aziz, K. H. Ahmed, S. Wang, A. M. Massoud and B. W. Williams, "A Neutral-Point Diode-Clamped Converter with Inherent Voltage-Boosting for a Four-Phase SRM Drive," in *IEEE Transactions on Industrial Electronics*, DOI: 10.1109/TIE.2019.2931268, vol. 67, no. 7, pp. 5313-5324, July 2020.
- [7] F. Peng, J. Ye and A. Emadi, "An Asymmetric Three-Level Neutral Point Diode Clamped Converter for Switched Reluctance Motor Drives," in *IEEE Transactions on Power Electronics*, DOI: 10.1109/TPEL.2016.2642339, vol. 32, no. 11, pp. 8618-8631, Nov. 2017.
- [8] P. Azer and J. Bauman, "An Asymmetric Three-Level T-Type Converter for Switched Reluctance Motor Drives in Hybrid Electric Vehicles," 2019 IEEE Transportation Electrification Conference and Expo (ITEC), DOI: 10.1109/ITEC.2019.8790602, Detroit, MI, USA, 2019, pp. 1-6.
- [9] D. Patil, S. Wang and L. Gu, "Multi-level converter topologies for high-power high-speed switched reluctance motor: Performance comparison," 2016 IEEE Applied Power Electronics Conference and Exposition (APEC), DOI: 10.1109/APEC.2016.7468274, Long Beach, CA, USA, 2016, pp. 2889-2896.
- [10] D. Mohanraj, J. Gopalakrishnan, B. Chokkalingam and L. Mihet-Popa, "Critical Aspects of Electric Motor Drive Controllers and Mitigation of Torque Ripple—Review," in *IEEE Access*, vol. 10, pp. 73635-73674, 2022, doi: 10.1109/ACCESS.2022.3187515.
- [11] M. Yilmaz and P. T. Krein, "Review of Battery Charger Topologies, Charging Power Levels, and Infrastructure for Plug-In Electric and Hybrid Vehicles," in *IEEE Trans. Power Electron.*, vol. 28, no. 5, pp. 2151-2169, May 2013.

- [12] N. Leemput, F. Geth, J. Van Roy, A. Delnooz, J. Büscher and J. Driesen, "Impact of Electric Vehicle On-Board Single-Phase Charging Strategies on a Flemish Residential Grid," in *IEEE Transactions on Smart Grid*, vol. 5, no. 4, pp. 1815-1822, July 2014.
- [13] H. Tu, H. Feng, S. Srdic and S. Lukic, "Extreme Fast Charging of Electric Vehicles: A Technology Overview," in *IEEE Transactions on Transportation Electrification*, vol. 5, no. 4, pp. 861-878, Dec. 2019.
- [14] A. K. Singh, M. Badoni and Y. N. Tatte, "A Multifunctional Solar PV and Grid Based On-Board Converter for Electric Vehicles," in *IEEE Transactions on Vehicular Technology*, vol. 69, no. 4, pp. 3717-3727, April 2020.
- [15] E. Ucer et al., "Analysis, Design, and Comparison of V2V Chargers for Flexible Grid Integration," in *IEEE Transactions on Industry Applications*, vol. 57, no. 4, pp. 4143-4154, July-Aug. 2021.
- [16] M. O. Badawy et al., "Design and Implementation of a 75-kW Mobile Charging System for Electric Vehicles," in *IEEE Transactions on Industry Applications*, vol. 52, no. 1, pp. 369-377, Jan.-Feb. 2016.
- [17] [Online]. Available: <http://www.andromedapower.com/orca-inceptive/>
- [18] "NEDO, sharp, and toyota to begin public road trials of electrified vehicles equipped with high-efficiency solar batteries," Toyota, Aichi, Japan, Jul. 2019, Accessed: Sep./Nov. 2021. [Online]. Available: https://global.toyota/en/newsroom/corporate/28787347.html?_ga=2.99166806.974048827.1604834947-1182370130.1604834947
- [19] U. B S, V. Khadkikar, H. H. Zeineldin, S. Singh, H. Otrok and R. Mizouni, "Direct Electric Vehicle to Vehicle (V2V) Power Transfer Using On-Board Drivetrain and Motor Windings," in *IEEE Transactions on Industrial Electronics*, vol. 69, no. 11, pp. 10765-10775, Nov. 2022.
- [20] I. Kioskeridis and C. Mademlis, "Maximum efficiency in single-pulse controlled switched reluctance motor drives," in *IEEE Transactions on Energy Conversion*, vol. 20, DOI 10.1109/TEC.2005.853738, no. 4, pp. 809-817, Dec. 2005.
- [21] C. Mademlis and I. Kioskeridis, "Performance optimisation in switched reluctance motor drives with online commutation angle control," in *IEEE Transactions on Energy Conversion*, vol. 18, DOI 10.1109/TEC.2003.815854, no. 3, pp. 448-457, Sept. 2003.
- [22] X. D. Xue, K. W. E. Cheng and S. L. Ho, "Optimisation and Evaluation of Torque-Sharing Functions for Torque Ripple Minimization in Switched Reluctance Motor Drives," in *IEEE Transactions on Power Electronics*, vol. 24, DOI 10.1109/TPEL.2009.2019581, no. 9, pp. 2076-2090, Sept. 2009.
- [23] R. B. Inderka and R. W. A. A. De Doncker, "DITC-direct instantaneous torque control of switched reluctance drives," in *IEEE Transactions on Industry Applications*, vol. 39, DOI 10.1109/TIA.2003.814578, no. 4, pp. 1046-1051, July-Aug. 2003.
- [24] H. J. Brauer, M. D. Hennen and R. W. De Doncker, "Control for Polyphase Switched Reluctance Machines to Minimise Torque Ripple and Decrease Ohmic Machine Losses," in *IEEE Transactions on Power Electronics*, vol. 27, DOI 10.1109/TPEL.2011.2161332, no. 1, pp. 370-378, Jan. 2012.

- [25] A.D. Cheok and Y. Fukuda, "A new torque and flux control method for switched reluctance motor drives," in *IEEE Transactions on Power Electronics*, vol. 17, DOI 10.1109/TPEL.2002.800968, no. 4, pp. 543-557, July 2002.
- [26] X. Deng, B. Mecrow, H. Wu and R. Martin, "Design and Development of Low Torque Ripple Variable-Speed Drive System With Six-Phase Switched Reluctance Motors," in *IEEE Transactions on Energy Conversion*, vol. 33, DOI 10.1109/TEC.2017.2753286, no. 1, pp. 420-429, March 2018.
- [27] H. Guo, "Considerations of Direct Torque Control for Switched Reluctance Motors," 2006 IEEE International Symposium on Industrial Electronics, Montreal, Que., 2006, pp. 2321-2325.
- [28] P. K. Reddy, D. Ronanki and P. Perumal, "Efficiency improvement and torque ripple minimisation of four-phase switched reluctance motor drive using new direct torque control strategy," in *IET Electric Power Applications*, vol. 14, no. 1, pp. 52-61, 1 2020.
- [29] K. R. Pittam, D. Ronanki, P. Perumal, A. R. Beig and S. S. Williamson, "Torque Ripple Minimization of Four-phase Switched Reluctance Motor using Direct Torque Control with an Innovative Switching Sequence Scheme," 2019 IEEE Energy Conversion Congress and Exposition (ECCE), Baltimore, MD, USA, 2019, pp. 1810-1815.
- [30] V. Shah, M. Alam and S. Payami, "High Torque/Ampere Direct Torque Control of Switched Reluctance Motor Drives," 2019 National Power Electronics Conference (NPEC), Tiruchirappalli, India, 2019, pp. 1-6.
- [31] S. Sau, R. Vandana and B. G. Fernandes, "A new direct torque control method for switched reluctance motor with high torque/ampere," *IECON 2013 - 39th Annual Conference of the IEEE Industrial Electronics Society*, 2013, pp. 2518-2523.
- [32] Z. Hao, Q. Yu, X. Cao, X. Deng and X. Shen, "An Improved Direct Torque Control for a Single-Winding Bearingless Switched Reluctance Motor," in *IEEE Transactions on Energy Conversion*, vol. 35, DOI: 10.1109/TEC.2020.2988549, no. 3, pp. 1381-1393, Sept. 2020.
- [33] N. Yan, X. Cao and Z. Deng, "Direct Torque Control for Switched Reluctance Motor to Obtain High Torque–Ampere Ratio," in *IEEE Transactions on Industrial Electronics*, vol. 66, DOI 10.1109/TIE.2018.2870355, no. 7, pp. 5144-5152, July 2019.
- [34] D. Lee, J. Liang, Z. Lee and J. Ahn, "A Simple Nonlinear Logical Torque Sharing Function for Low-Torque Ripple SR Drive," in *IEEE Transactions on Industrial Electronics*, vol. 56, DOI 10.1109/TIE.2009.2024661, no. 8, pp. 3021-3028, Aug. 2009.
- [35] J. Ye, B. Bilgin and A. Emadi, "An Extended-Speed Low-Ripple Torque Control of Switched Reluctance Motor Drives," in *IEEE Transactions on Power Electronics*, DOI 10.1109/TPEL.2014.2316272, vol. 30, no. 3, pp. 1457-1470, March 2015.
- [36] S. Song, G. Fang, R. Hei, J. Jiang, R. Ma and W. Liu, "Torque Ripple and Efficiency Online Optimisation of Switched Reluctance Machine Based on Torque per Ampere Characteristics," in *IEEE Transactions on Power Electronics*, vol. 35, DOI 10.1109/TPEL.2020.2974662, no. 9, pp. 9608-9616, Sept. 2020.

- [37] Q. Sun, J. Wu and C. Gan, "Optimised Direct Instantaneous Torque Control for SRMs With Efficiency Improvement," in *IEEE Transactions on Industrial Electronics*, vol. 68, DOI 10.1109/TIE.2020.2975481, no. 3, pp. 2072-2082, March 2021.
- [38] H. Chang et.al, "An Integrated Driving/Charging Switched Reluctance Motor Drive Using Three-Phase Power Module," in *IEEE Trans. Ind. Electron.*, vol. 58, no. 5, pp. 1763-1775, May 2011.
- [39] J. Thankachan and S. P. Singh, "Bidirectional multiport solar-assisted SRM drive for pure electric vehicle applications with versatile driving and autonomous charging capabilities", *IET Elect. Power Appl.*, vol. 14, no. 4, pp. 570-583, 2020.
- [40] H. Chang and C. Liaw, "Development of a Compact Switched Reluctance Motor Drive for EV Propulsion With Voltage-Boosting and PFC Charging Capabilities," in *IEEE Trans. Veh. Technol.*, vol. 58, no. 7, pp. 3198-3215, Sept. 2009.
- [41] Jingquan Chen et.al, "Analysis and design of a low-stress buck-boost converter in universal-input PFC applications," in *IEEE Trans. Power Electron.*, vol. 21, no. 2, pp. 320-329, March 2006.
- [42] L. Huber et.al, "Performance Evaluation of Bridgeless PFC Boost Rectifiers," in *IEEE Trans. Power Electron.*, vol. 23, no. 3, pp. 1381-1390, May 2008.
- [43] Y. Hu et.al, "Split Converter-Fed SRM Drive for Flexible Charging in EV/HEV Applications," in *IEEE Trans. Ind. Electron.*, vol. 62, no. 10, pp. 6085-6095, Oct. 2015.
- [44] J. Cai and X. Zhao, "An On-Board Charger Integrated Power Converter for EV Switched Reluctance Motor Drives," in *IEEE Trans. Ind. Electron.*, vol. 68, no. 5, pp. 3683-3692, May 2021.
- [45] K. Hu et.al, "An EV SRM Drive Powered by Battery/Supercapacitor With G2V and V2H/V2G Capabilities," in *IEEE Trans. Ind. Electron.*, vol. 62, no. 8, pp. 4714-4727, Aug. 2015.
- [46] H. -C. Chen and B. -W. Huang, "Integrated G2V/V2G Switched Reluctance Motor Drive With Sensing Only Switch-Bus Current," in *IEEE Trans. Power Electron.*, vol. 36, no. 8, pp. 9372-9381, Aug. 2021.
- [47] H. Cheng et.al, "Integrated Drive Converter of SDS-SRM With Isolation and Non isolation Charging Capabilities for Electric Vehicle," in *IEEE Trans. Ind. Electron.*, vol. 69, no. 9, pp. 8679-8691, Sept. 2022.
- [48] C. Gan, J. Wu, Y. Hu, S. Yang, W. Cao and J. M. Guerrero, "New Integrated Multilevel Converter for Switched Reluctance Motor Drives in Plug-in Hybrid Electric Vehicles With Flexible Energy Conversion," in *IEEE Trans. Power Electron.*, vol. 32, no. 5, pp. 3754-3766, May 2017.
- [49] C. Gan, N. Jin, Q. Sun, W. Kong, Y. Hu and L. M. Tolbert, "Multiport Bidirectional SRM Drives for Solar-Assisted Hybrid Electric Bus Powertrain With Flexible Driving and Self-Charging Functions," in *IEEE Trans. Power Electron.*, vol. 33, no. 10, pp. 8231-8245, Oct. 2018.
- [50] Q. Sun, J. Wu, C. Gan, J. Si, J. Guo and Y. Hu, "Cascaded Multiport Converter for SRM-Based Hybrid Electrical Vehicle Applications," in *IEEE Trans. Power Electron.*, vol. 34, no. 12, pp. 11940-11951, Dec. 2019.

- [51] M. Ma, Z. Chang, Y. Hu, F. Li, C. Gan and W. Cao, "An Integrated Switched Reluctance Motor Drive Topology With Voltage-Boosting and On-Board Charging Capabilities for Plug-In Hybrid Electric Vehicles (PHEVs)," in *IEEE Access*, vol. 6, pp. 1550-1559, 2018.
- [52] H. Cheng, L. Wang, L. Xu, X. Ge and S. Yang, "An Integrated Electrified Powertrain Topology With SRG and SRM for Plug-In Hybrid Electrical Vehicle," in *IEEE Trans. Ind. Electron.*, vol. 67, no. 10, pp. 8231-8241, Oct. 2020
- [53] S. Loudot et al., "Fast charging device for an electric vehicle," Sep. 30 2014, uS Patent 8,847,555.
- [54] G. R. Chandra Mouli, J. Schijffelen, M. van den Heuvel, M. Kardolus and P. Bauer, "A 10 kW Solar-Powered Bidirectional EV Charger Compatible With Chademo and COMBO," in *IEEE Transactions on Power Electronics*, vol. 34, no. 2, pp. 1082-1098, Feb. 2019.
- [55] V. Shah, K. Gautam and S. Payami, "Integrated Power Converter with G2V, V2G and Direct V2V Capabilities for SRM Drive Based Electric Vehicle Application," 2022 Second International Conference on Power, Control and Computing Technologies (ICPC2T), 2022, pp. 1-6.
- [56] C. Viana and P. W. Lehn, "A Drivetrain Integrated DC Fast Charger With Buck and Boost Functionality and Simultaneous Drive/Charge Capability," in *IEEE Trans. Transp. Electrific.*, vol. 5, no. 4, pp. 903-911, Dec. 2019.
- [57] U. B S, V. M. Khadkikar, H. Zeineldin, S. Singh, H. Otrók and R. Mizouni, "Direct Electric Vehicle to Vehicle (V2V) Power Transfer Using On-board Drivetrain and Motor Windings, " in *IEEE Trans. Ind. Electron.*, doi: 10.1109/TIE.2021.3121707.
- [58] F. Musavi, M. Edington, W. Eberle and W. G. Dunford, "Evaluation and Efficiency Comparison of Front End AC-DC Plug-in Hybrid Charger Topologies," in *IEEE Trans. on Smart Grid*, vol. 3, no. 1, pp. 413-421, March 2012.
- [59] Y. Lee, A. Khaligh and A. Emadi, "Advanced Integrated Bidirectional AC/DC and DC/DC Converter for Plug-In Hybrid Electric Vehicles," in *IEEE Trans. on Vehicular Technology*, vol. 58, no. 8, pp. 3970-3980, Oct. 2009.
- [60] B. Singh, B. N. Singh, A. Chandra, K. Al-Haddad, A. Pandey and D. P. Kothari, "A review of single-phase improved power quality AC-DC converters," *IEEE Trans. Ind. Electron.*, vol. 50, no. 5, pp. 962-981, Oct. 2003.
- [61] Jingquan Chen, D. Maksimovic and R. W. Erickson, "Analysis and design of a low-stress buck-boost converter in universal-input PFC applications," in *IEEE Trans. Power Electron.*, vol. 21, no. 2, pp. 320-329, March 2006.
- [62] C. Oh, D. Kim, D. Woo, W. Sung, Y. Kim and B. Lee, "A High-Efficient Nonisolated Single-Stage On-Board Battery Charger for Electric Vehicles," in *IEEE Trans. Power Electron.*, vol. 28, no. 12, pp. 5746-5757, Dec. 2013.

- [63] M. O. Badawy, Y. Sozer and J. A. De Abreu-Garcia, "A Novel Control for a Cascaded Buck–Boost PFC Converter Operating in Discontinuous Capacitor Voltage Mode," in *IEEE Trans. Ind. Electron.*, vol. 63, no. 7, pp. 4198-4210, July 2016.
- [64] Y. Lee, A. Khaligh and A. Emadi, "A Compensation Technique for Smooth Transitions in a Noninverting Buck–Boost Converter," in *IEEE Trans. Power Electron.*, vol. 24, no. 4, pp. 1002-1015, April 2009.
- [65] A. Chakraborty, A. Khaligh and A. Emadi, "Combination of Buck and Boost Modes to Minimize Transients in the Output of a Positive Buck-Boost Converter," *IECON 2006 - 32nd Annual Conference on IEEE Industrial Electronics*, 2006, pp. 2372-2377.
- [66] <https://www.redalyc.org/journal/430/43050083002/html/>

APPENDIX

A. 1. Prototype 4-phase SRM inductance and torque look-up table

The obtained torque and inductance plots for the prototype SRM are shown in **Fig. A.1**. The inductance plot with respect to rotor position and current is given in **Fig. A. 1. (a)** and the torque v/s rotor position, current plot is given in **Fig. A. 1. (b)**. The torque and inductance plots are spatially shifted for obtaining plots for other phases. Table. A.1 lists the key parameters for the prototype 4-phase SRM.

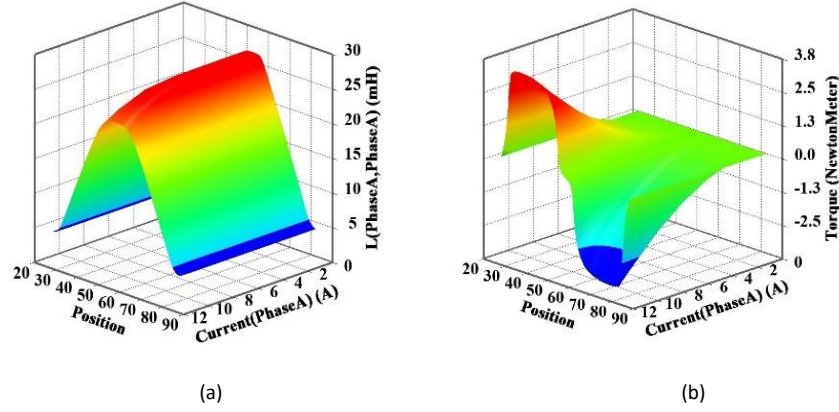


Fig. A.1. (a) Inductance plot with respect to position, current. (b) Torque plot with respect to position, current.

TABLE A. 1
MOTOR PARAMETERS

Parameters	4-phase SRM
Phase	4
Stator poles: rotor poles	8:6
Rated power: Peak power	1.1kW:2.2kW
Rated current (peak)	11A (peak)
Rated speed	3000 rpm
Phase resistance	0.6 Ω
Stator arc angle	22.5 deg
Rotor arc angle	30 deg

A. 2. Average small-signal model of the bridgeless power factor correction boost converter [66]

The bridgeless power factor correction boost converter can be perturbed by small variations in the input voltage (V_s), causing small variations in the input current and the output voltage with respect to their steady state values. The control system must modify the duty cycle (D) to control input current and output voltage state variables. These variations around the equilibrium point can be expressed as-

$$D = \bar{D} + \hat{d}, \quad V_s = \bar{V}_s + \widehat{v_s}, \quad (A.1)$$

where D and V_s denotes the equilibrium point values and \hat{d} , and $\widehat{v_s}$ represents the small-signal variations around the equilibrium point.

The averaged model can be then rewritten as-

$$\frac{d}{dt}(\bar{X} + \hat{x}) = [A_1 (\bar{D} + \hat{d}) + A_2 (1 - \bar{D} - \hat{d})] (\bar{X} + \hat{x}) + [B_1 (\bar{D} + \hat{d}) + B_2 (1 - \bar{D} - \hat{d})] (\bar{V}_s + \hat{v}_s) \quad (A.2)$$

The above equation represents a non-linear model of the bridgeless power factor correction boost converter, since it exhibits the product of time-dependent variables. The non-linear model can be linearized based on the following assumptions: $\bar{V}_s \gg \hat{v}_s$, $\bar{D} \gg \hat{d}$, $\bar{X} \gg \hat{x}$, i.e., variations of signals around the equilibrium point are small in comparison with the signal magnitude. Consequently, the magnitudes of \hat{v}_s and \hat{d} are negligible in comparison with the magnitudes of \bar{V}_s , \bar{X} and \bar{D} , i.e., $d\bar{V}_s \cong 0$. The non-linear model obtained after assumptions mentioned is given by-

$$\frac{d}{dt}(\hat{x}) \cong A\hat{x} + B\hat{v}_s + [(A_1 - A_2)\bar{X} + (B_1 - B_2)\bar{V}_s] \hat{d} \quad (A.3)$$

From the procedure as discussed in [66], the required bridgeless PFC boost converter transfer function can be given as-

$$Gi(s) = \left. \frac{\widehat{v_s(s)}}{\widehat{d_s(s)}} \right|_{\widehat{v_s(s)}=0} = \frac{\bar{V}_s}{R_L(1-D)^3} \frac{(2 + R_L C s)}{\frac{LC}{(1-D)^2} s^2 + \frac{L}{R_L(1-D)^2} s + 1}, \quad (A.4)$$

where L is operating inductance of the motor, C is the DC-link capacitor. R_L is the load resistance corresponding the designed power level, as discussed in [66]. Considering the operating point as adopted for simulation and experimental analysis in chapter-3. Substituting the values closed loop transfer function of $Gi(s) = \left. \frac{\widehat{v_s(s)}}{\widehat{d_s(s)}} \right|_{\widehat{v_s(s)}=0}$ is given by-

$$Gi(s) = \frac{1.424 s + 15.15}{2.492 * e^{-5 s^2} + 0.0001325 s + 1}. \quad (A.5)$$

$$r_{1,2} = -2.658 \pm 200.303i$$

Equation (A.5) shows the conjugate and complex roots of $Gi(s)$. The real components of these roots are negative; in consequence, the current system of the bridgeless PFC boost converter is inherently stable in open loop.

Control systems can be tuned using the root-locus method and the Bode-diagrams. The root-locus method allows analyzing the effect of the gain variations over the poles allocation and absolute stability of the system. Bode-diagrams permit determining bandwidth of current and voltage systems in open and close loop. This tuning permit selecting the appropriate parameters of PI controller to achieve desired system behavior in closed loop [66].

The bridgeless PFC boost converter configuration adopted during battery charging mode exhibits a two-loop cascade control structure composed of Proportional-Integral (PI) controller. The bridgeless PFC boost converter presented in this study exhibits a two-loop cascade control structure composed of Proportional-Integral (PI) controllers.

The inner current loop is faster and is responsible for achieving unity power factor operation. Nevertheless, the inner current control system must reject the switching noise at fsw.

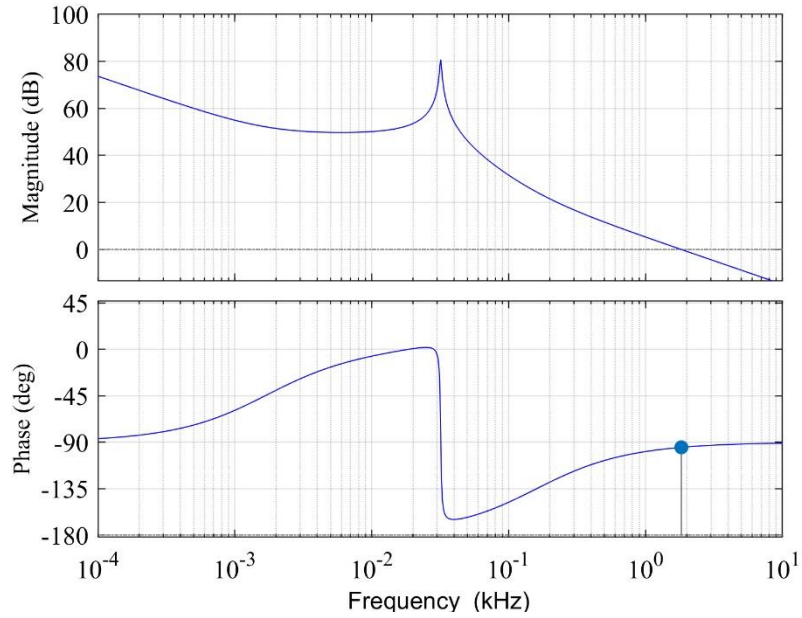
The transfer function of inner current controller is given by-

$$C_i(s) = \frac{K_p s + K_i}{s}, \quad (A.6)$$

where Kp and Ki are the proportional and integral gains of the PI controller. The transfer function of the closed loop current controller is-

$$G(s) = \frac{C_i(s) * G_i(s)}{1 + C_i(s) * G_i(s)} \quad (A.7)$$

The bandwidth of the inner current control system is set to reject the switching noise, i.e., the current control in closed-loop should reject noise at 10 kHz and it must track to iref. To calculate the Kp and Ki values the gain margin and phase margin values are fixed as per [66], and then bode plots are used to plot the closed loop response, as shown in **Fig. A. 2**.



Thus, Kp and Ki can also be obtained from (A.7) with the help of PID tuner block set in MATLAB. The values obtained Kp and Ki values obtained with the PID tuner block set is shown in **Fig. A.3**.

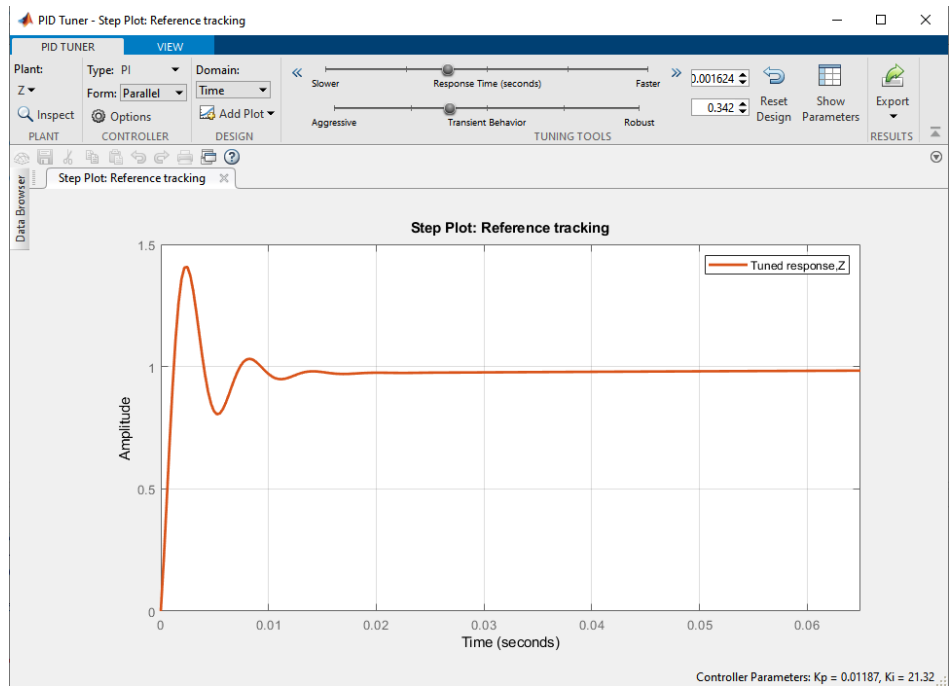


Fig. A.3. Closed loop response of $G(s)$ with $K_p = 0.01187$, and $K_i = 21.32$.

The MATLAB code used for calculation of $G_i(s)$ is given below-

```
R=(40)*2;
C=2.35*0.001;
L=0.007;
D=0.1875;
Vs=325;
A=Vs/(R*((1-D)^3));
B=R*C;
E=(L*C)/((1-D)^2);
F=L/(R*(1-D)^2);
X=A*[B 2];
Y=[E F 1];
Z=tf(X,Y)
Kp=0.2;
Ki=200;
num=[Kp Ki];
den=[1 0];
PI=tf(num,den);
%G=Z*PI/(1+Z*PI);
OLTF=Z*PI;
bode(OLTF)
%margin(Z);
```

```
%hold on  
% bode(OLTF)  
%bode(OLTF)  
% hold off
```